Scattering and topological properties of driven-dissipative quantum fluids

TESIS DOCTORAL

memoria presentada para optar al grado de
Doctor en Ciencias Físicas
Universidad Autónoma de Madrid
Departamento de Física Teórica de la Materia Condensada
Programa de Doctorado
Física de la Materia Condensada y Nanotecnología
viernes, 8 de julio del 2016

por

Andrei Ciprian Berceanu

nacido en Bucarest, Rumanía en 1983

Comisión:

Director:	Prof. dr. F. M. Marchetti (UAM)
Tribunal:	Prof. dr. C. Tejedor (UAM)
	Prof. dr. L. Viña (UAM)
	Dr. A. Amo (CNRS, France)
	Dr. J. J. García-Ripoll (CSIC)
	Dr. T. Ozawa (Università di Trento, Italy)

El autor agradece el apoyo financiero de FP7 ITN "Clermont4" y de la European Science Foundation (ESF) a través de POLATOM Grant 4914.

The author acknowledges financial support from FP7 ITN "Clermont4" and from the European Science Foundation (ESF) through POLATOM Grant 4914.

UAM
UNIVERSIDAD AUTÓNOMA
DE MADRID

Bunicilor mei.

Contents

Resumen

This short overview of the thesis work is written in Spanish as required by the Spanish Government for thesis manuscripts in a foreign language.

La superfluidez, que es la habilidad de un fluido para fluir sin viscosidad aparente, es una de las consecuencias más impactantes de la coherencia cuántica colectiva, con manifestaciones que van desde la metaestabilidad de las supercorrientes en geometrías múltiplemente conexas, la aparición de vórtices cuánticos o la existencia de una velocidad crítica para flujos sin fricción cuando el fluido se dispersa alrededor de un defecto. Tradicionalmente, la superfluidez se ha estudiado en sistemas en equilibrio como ^{4}He líquido y gases atómicos ultrafríos. Los avances experimentales en óptica no lineal, en particular las microcavidades de polaritones han allanado el camino para estudiar los fenómenos relacionados con la superfluidez en condiciones de non equilibrio, en presencia de bombeo externo y dissipación.

Igualmente interesante es la posibilidad de simular fases topológicas de la materia, así como los estados Hall cuánticos enteros y fraccionarios, más allá de los sistemas electrónicos tradicionales. En particular, los experimentos de fotónica en matrices de resonadores en presencia de bombeo y dissipación, ofrecen un alto grado de control de los parámetros que describen el sistema, así como un acceso directo a los autoestados y el espectro de energía.

En esta tesis estudiamos los efectos hidrodinámicos así como las propiedades topológicas de sistemas en presencia de bombeo y dissipación,. En particular, analizamos el comportamiento de tipo superfluido en microcavidades de polaritónes, así como la topología del espacio de momentos de matrices de resonadores acoplados.

Los polaritones excitónicos en microcavidades son cuasipartículas resultantes de la mezcla de excitones (pares electrón-hueco) y fotones confinados dentro de microcavidades con pozos cuánticos. Mientras que en los fluidos polaritónicos se han visto comportamientos de coherencia colectiva, la conexión entre las distintas manifestaciones de comportamientos superfluidos es más compleja que en los sistemas en equilibrio. En esta tesis, consideraremos tanto el caso de una configuración de un solo fluido (estado de bombeo o de pump), como el caso de tres fluidos en el régimen de oscilación óptica paramétrica que emerge de la dispersión paramétrica del estado pump a los estados de signal y de idler. En ambos casos,

miraremos la respuesta de la dispersión de los polaritones frente a un defecto estático débil.

Para la configuración de un solo fluido, evaluaremos de forma analítica el arrastre ejercido por el fluido en el defecto. Para velocidades bajas del fluido, la frequencia del pump clasifica el espectro de excitaciones colectivas en tres categorías: lineal, difusivo y gapped. Vemos que tanto el régimen lineal como el difusivo comparten cualitativamente el cambio de comportamiento del arrastre entre el régimen subsónico y supersónico. La velocidad crítica donde se produce este cambio de comportamiento esta dada por la velocidad del sonido en el régimen lineal. En cambio, para los espectros gapped encontramos que la velocidad crítica sobrepasa la velocidad del sonido. En todos los casos, vemos que el arrastre residual en el régimen subcrítico está causado por la vida media finida de los polaritones. Además, por debajo de la velocidad crítica, el arrastre varía de forma lineal con la vida del polaritón, de acuerdo con estudios numéricos previos.

El régimen de oscilación óptica paramétrica presenta retos adicionales relacionados con la presencia de tres fluidos acoplados. Se ha demonstrado que la coherencia macroscópica espontánea que proviene del acoplamiento de fase entre el estado de signal y el de idler es responsable de la metaestabilidad simultánea del flujo cuantisado de ambos estados de signal y idler. Encontramos que las modulaciones generadas por el defecto en cada fluido no vienen solo determinadas por el anillo de dispersión en el espacio de momentos (Rayleigh ring) sino que cada componente tiene anillos adicionales debidos a la interacción con los otros componentes, impuesta por procesos no lineales y paramétricos. Señalamos tres factores que determinan cual de estos anillos tiene la mayor influencia en la respuesta de cada fluido: la fuerza del acoplamiento entre los tres fluidos, la resonancia del anillo con la dispersión energética de los polaritones y por último la velocidad de grupo del fluido junto con el tiempo de vida de los polaritones. Para las condiciones típicas de dispersión paramétrica, el estado de pump está en el régimen supercrítico, por lo tanto, tanto el estado de signal como el estado de idler mostrarán la misma modulación que se aprecia en el pump, con lo cual ninguno de los tres estados manifiesta un comportamiento superfluido. Sin embargo, el signal parece fluir sin fricción en los experimentos, debido a que los tres factores mencionados anteriormente se unen para reducir la amplitud de las modulaciones por debajo de los niveles detectables.

Los sistemas en presencia de bombeo y dissipacion pueden mostrar fenómenos interesantes aunque no haya interacciones entre las partículas constituyentes, debido a la topología no trivial de las bandas de energía. En la parte final de esta tesis, presentaremos una propuesta realista para un experimento óptico utilizando matrices acopladas resonantes. Hemos estudiado de forma teórica el modelo Harper-Hofstadter para sistemas con bombeo y decadimiento en la presencia de una trampa armónica débil. Si omitimos el bombeo del láser y las pérdidas, podremos interpretar los autovalores de este sistema (bajo ciertas aproximaciones) como los niveles de Landau en el espacio de momentos toroidal, donde la curvatura de Berry actúa como un campo magnético. Vemos que las principales caracterísi-

cas de estos autoestados pueden ser observadas en el estado estacionario bajo un bombeo monocromático coherente. Además, vemos que los niveles de Landau en el espacio de momentos tienen características claras en medidas espectroscópicas experimentales. Finalmente, discutiremos las propiedades geométricas de las bandas energéticas y de las partículas en campos magnéticos.

Abstract

Superfluidity, the ability of a fluid to flow without apparent viscosity, is one of the most striking consequences of collective quantum coherence, with manifestations ranging from metastability of supercurrents in multiply connected geometries to the appearance of quantized vortices, or the existence of a critical velocity for frictionless flow when scattering against a defect. While traditionally investigated in equilibrium systems, like liquid ^{4}He and ultracold atomic gases, experimental advances in nonlinear optics, in particular regarding microcavity exciton-polaritons, paved the way for studying superfluid-related phenomena in a driven-dissipative framework.

Equally exciting is the possibility of realising topological phases of matter, such as the integer or fractional quantum Hall states, outside of traditional electronic systems. Photonics experiments in driven-dissipative resonator arrays, in particular, offer a high degree of controllability and tunability, as well as unprecedented experimental access to the eigenstates and energy spectrum.

This thesis reports on hydrodynamic effects, as well as topological properties, of driven-dissipative systems. In particular, we analyze the superfluid-like behaviour of microcavity exciton-polaritons, as well as the momentum-space topology of coupled resonator arrays.

Microcavity exciton-polaritons are quasiparticles resulting from the mixing of excitons (bound electron-hole pairs) and photons confined inside semiconductor microcavities. While polariton fluids have been shown to display collective coherence, the connection between the various manifestations of superfluid behaviour is more involved compared to equilibrium systems. In this manuscipt, we consider both the case of a single-fluid pump-only configuration, as well as the three-fluid optical parametric oscillator regime that results from parametric scattering of the pump to the signal and idler states. In both cases, we look at the response of the moving polaritons scattering against a weak static defect present in the microcavity.

For the single fluid, we evaluate analytically the drag exerted by the fluid on the defect. For low fluid velocities, the pump frequency classifies the collective excitation spectra in three different categories: linear, diffusive-like and gapped. We show that both the linear and diffusive-like cases share a qualitatively similar crossover of the drag from the subsonic to the supersonic regime as a function

of the fluid velocity, with a critical velocity given by the speed of sound found for the linear regime. In contrast, for gapped spectra, we find that the critical velocity exceeds the speed of sound. In all cases, we show that the residual drag in the subcritical regime is caused by the nonequilibrium nature of the system. Also, well below the critical velocity, the drag varies linearly with the polariton lifetime, in agreement with previous numerical studies.

The optical parametric oscillator regime presents an additional challenge, as one is dealing with three coupled fluids. The spontaneous macroscopic coherence following the phase locking of the signal and idler fluids has been already shown to be responsible for their simultaneous quantized flow metastability. We find that the modulations generated by the defect in each fluid are not only determined by its associated scattering ring in momentum space, but each component displays additional rings because of the cross-talk with the other components imposed by nonlinear and parametric processes. We single out three factors determining which one of these rings has the biggest influence on each fluid response: the coupling strength between the three fluids, the resonance of the ring with the polariton dispersion, and the values of each fluid group velocity and lifetime together establishing how far each modulation can propagate from the defect. For the typical conditions of parametric scattering, the pump is in the supercritical regime, so the signal and idler will show the modulations of the pump, meaning none of the three states manifests superfluid behaviour. However, the signal appears to flow without friction in the experimental study, because the three factors mentioned above conspire to reduce the amplitude of its modulations below currently detectable levels.

Driven-dissipative systems can show interesting phenomena also without interactions, stemming from the nontrivial topology of their energy bands. In the final part of this thesis, we present a realistic proposal for an optical experiment using state-of-the-art coupled resonator arrays. We study theoretically the driven-dissipative Harper-Hofstadter model on a square lattice in the presence of a weak harmonic trap. Without pumping and losses, the eigenstates of this system can be understood, under certain approximations, as momentum-space toroidal Landau levels, where the Berry curvature, a geometrical property of an energy band, acts like a momentum-space magnetic field. We show how key features of these eigenstates can be observed in the steady-state of the driven-dissipative system under a monochromatic coherent drive. We also show that momentum-space Landau levels would have clear signatures in spectroscopic measurements in such experiments, and we discuss the insights gained in this way into geometrical energy bands and particles in magnetic fields.

List of Publications

The following articles have been published in the context of this thesis:

- *Onset and dynamics of vortex-antivortex pairs in polariton optical parametric oscillator superfluids,* G. Tosi, F. M. Marchetti, D. Sanvitto, C. Antón, M. H. Szymańska, A. C. Berceanu, C. Tejedor, L. Marrucci, A. Lemaître, J. Bloch, and L. Viña, Phys. Rev. Lett. **107**, 036401 (2011).

- *Drag in a resonantly driven polariton fluid,* A. C. Berceanu, E. Cancellieri, and F. M. Marchetti, J. Phys.: Condens. Matter **24**, 235802 (2012) [Chapter 3].

- *Multicomponent polariton superfluidity in the optical parametric oscillator regime,* A. C. Berceanu, L. Dominici, I. Carusotto, D. Ballarini, E. Cancellieri, G. Gigli, M. H. Szymańska, D. Sanvitto, and F. M. Marchetti, Phys. Rev. B **92**, 035307 (2015) [Chapter 4].

- *Momentum-space Landau levels in driven-dissipative cavity arrays,* A. C. Berceanu, H. M. Price, T. Ozawa, and I. Carusotto, Phys. Rev. A **93**, 013827 (2016) [Chapter 5].

- *Momentum-space Landau levels in arrays of coupled ring resonators,* H. M. Price, A. C. Berceanu, T. Ozawa, and I. Carusotto, Proc. SPIE **9762**, 97620W (2016).

Preface

Systems far from thermal equilibrium frequently show novel features when compared to their equilibrium counterparts. As an everyday example, consider a group of birds displaying long-range ordered behaviour, manifested by forming a flock under certain conditions. This behaviour can be modeled by introducing a time step rule, such that each individual bird in a group determines its next direction on each time step by averaging the directions of its neighbours and adding some random noise on top of that [1]. It can be shown that, in the limit of the velocity going to zero, the model reduces to the XY model in two dimensions, where the spin is represented by the bird velocity. Since the 2D XY model does not spontaneously break the symmetry at any finite temperature (as justified by the Mermin-Wagner theorem), one can show that the appearance of the long-range ordered phase is a direct consequence of nonequilibrium aspects of the model. In a nutshell, the neighbours of one particular bird will be different at different times, depending on the velocity field. This gives rise to a time-dependent variable-ranged interaction, which can stabilize the ordered phase.

Non-equilibrium driven-dissipative photonic systems, such as polaritons in semiconductor microcavities or arrays of coupled optical resonators, have recently attracted a lot of interest due to the possibility of observing quantum phenomena which normally require very low temperatures and/or intense magnetic fields and are traditionally restricted to the domain of solid-state systems or ultracold atomic gases. Besides being highly tunable, these optical systems facilitate direct experimental access to observables such as the wavefunction or energy spectrum, all at room temperature. In particular, microcavity polaritons have allowed the observation of collective hydrodynamic phenomena, ranging from frictionless flow around a small defect to the formation of quantized vortices and dark solitons at the surface of large impenetrable obstacles [2], while ring-resonator arrays coupled to artificial magnetic fields have recently allowed engineering topological edge states robust to disorder [3].

Microcavity polaritons are quasiparticles resulting from the strong coupling of cavity photons and quantum well excitons [4, 5], and have the prerogative of being both easy to manipulate, via an external laser, and detect, via the light escaping from the cavity [6]. The finite polariton lifetime establishes the system

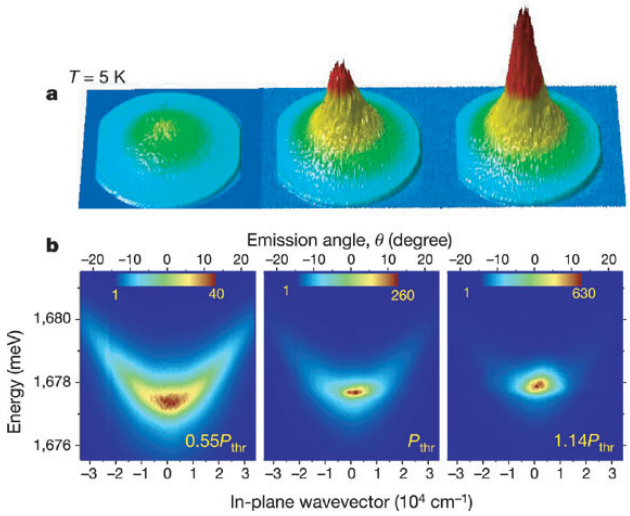

Figure 1: Experimental observation of polariton Bose-Einstein condensation. A sharp and intense peak corresponding to the lowest momentum state is formed in the center of the far-field emission [top panels], with increasing pump power (left to right). The corresponding energy-resolved emission [bottom panels] show that above the condensation threshold, the emission comes almost entirely from the lowest energy state situated at the bottom of the polariton dispersion. From Ref. [7].

as intrinsically out of equilibrium: an external pump is needed to continuously replenish the cavity of polaritons, that quickly, on a scale of tens of picoseconds, escape. The pumping can be done resonantly, close to the polariton energy dipersion, or non-resonantly.

The landmark observation [7] of polariton condensation in 2006, as shown in Fig. 1, was achieved using a non-resonant experimental setup. In the experiments, the system was incoherently excited by a laser beam tuned at a very high energy. Relaxation of the excess energy [8, 9] lead to a population of the cavity polariton states and, above a certain laser power threshold, to Bose-Einstein condensation into the lowest polariton state.

Due to their energy dispersion and strong nonlinearity inherited from the excitonic component, polaritons resonantly injected by the external laser into the pump state with a suitable wavevector and energy can undergo coherent stimulated scattering into two conjugate states [10–12], called the signal and the idler, in a process known as optical parametric oscillator (OPO). Since their first realisation [13–17], the interest in microcavity optical parametric phenomena has involved several fields of fundamental and applicative research [18–24].

The superfluid properties of a resonantly pumped polariton quantum fluid,

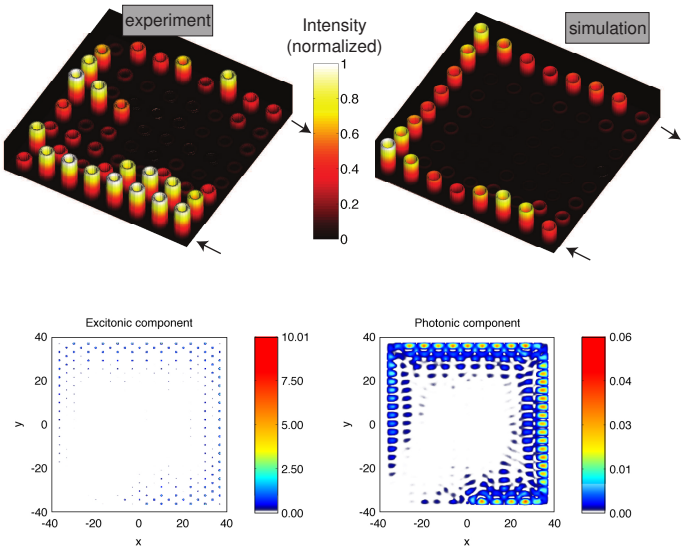

Figure 2: *Top panels:* Simulated (right panel) and observed (left panel) edge state propagation in a ring-resonator array. The light enters from one corner and exits from the other, as signaled by the arrows. Adapted from Ref. [3]. *Bottom panels:* Simulated edge state propagation in a polariton system. Intensities of the exciton (left panel) and photon (right panel) fields obtained when pumping a lattice at the center of its lower edge. From Ref. [25].

both in the pump-only configuration (without parametric scattering) as well as the OPO regime, have been actively investigated experimentally, as well as theoretically [2]. In particular, a supression of scattering in the pump-only case was observed [26] below a critical velocity, similar to what has been predicted by the Landau criterion for equilibrium superfluid condensates. While in equilibrium condensates different aspects of superfluidity are typically closely related [27], this is no longer true in a non-equilibrium context. Independent of the pumping scheme, the driving and the polariton finite lifetime force one to reconsider the meaning of superfluid behaviour, when the spectrum of collective excitations is complex rather than real, raising question about the applicability of a Landau criterion [28]. An additional complexity characterises the OPO regime, namely, the simultaneous presence of three oscillation frequencies and momenta for pump, signal and idler correspondingly increases up to 12 (or 6, depending on the approximation used to describe the system) the number of collective excitation branches [29]. Note that from the experimental point of view, pioneering experiments [30] have observed a ballistic nonspreading propagation of signal/idler

polariton wavepackets in a triggered-OPO configuration, as well as demonstrating the existence and metastability of vortex configurations [31] in the signal and idler.

Very recently, the polariton community started to explore topological effects in polariton lattices [25, 32–35]. The idea is to break time reversal symmetry by the application of a strong external magnetic field, giving rise to energy bands with nontrivial topology. In particular, Ref. [25] proposes an exciton-photon coupling with a winding phase in momentum space, giving rise to polaritonic bands with chiral edge modes that allow unidirectional propagation, protected against backscattering. The bottom panels of Fig. 2 show the exciton and photon fields traveling together as a unique polaritonic counter-clockwise chiral edge mode. In this context, dissipation in the form of photon losses provides a coupling to the outside continuum of modes and, as such, can be used to detect or inject edge modes. It would be interesting to study the feasability of coupled micropillars for this type of physics, in view of the recent experimental findings of a linear graphene-like dispersion [36] as well as edge states [37] in honeycomb micropillar lattices. On the other hand, topologically protected edge states have already been experimentaly observed [3] in the case of silicon-based optical resonator arrays (see top panels of Fig. 2), due to recent advances in creating synthetic gauge fields, which have opened new horizons for simulating topological phases of matter also with neutral particles, such as photons [38] (or ultracold atoms [39–41]). Rather than simply replicating previous measurements, experiments with synthetic gauge fields allow for unprecedented access to properties such as the eigenstates or eigenspectrum, while the tunability and controllability of these experiments offer the prospect of simulating novel physics.

Contents of this thesis

This manuscript is split in two parts: part I is a detailed review of the basic concepts, including both the theoretical formalism, as well as the relevant experiments, necessary for understanding part II, which presents the three main works published as part of my PhD (Chapters 3, 4 and 5). The two systems chosen for ilustrating the basic physical concepts are ultracold atomic gases (Chapter 1) and microcavity exciton-polaritons (Chapter 2). We now give a brief description of the content of each of the chapters.

In Chapter 1, we describe the phenomenon of Bose-Einstein condensation, and introduce the Gross-Pitaevskii equation which is extended in Chapter 2 to the case of polariton condensates. We then review the linear response of a moving atomic condensate to a weak stationary defect, leading to discussion on superfluidity. This scattering problem is the equilibrium conterpart of the problems studied in Chapters 3 and 4 in the context of polaritons in the resonantly pumped and optical parametric oscillator regimes, respectively. Finally, we introduce the Harper-Hofstadter model, which is the backbone of Chapter 5.

In Chapter 2, we introduce microcavity exciton-polaritons, and their theoret-

ical description in terms of a driven-dissipative Gross-Pitaevskii equation. We discuss both the resonantly pumped system which is used in Chapter 3, as well as the optical parametric oscillator of Chapter 4, and we make the connection to the superfluid-related phenomena previously introduced in Chapter 1.

In Chapter 3, we study the scattering of a resonantly pumped polariton condensate against a static defect of the microcavity, for the simplified case of small fluid velocities, when the polariton dispersion can be considered quadratic. After discussing the effects of dissipation on the Bogoliubov excitation spectra, we find that the finite polariton lifetime also affects the drag exerted by the condensate on the defect. In particular, we show that there is a nonzero drag force, entirely due to the out-of-equilibrium nature of the system, even in the "superfluid regime". Finally, we characterise the behaviour of the drag as a function of the condensate velocity and polariton lifetime.

In Chapter 4, we present a theoretical and experimental study of the same scattering problem, now in the context of an optical parametric oscillator consisting of three coupled condensates: the pump, the signal and the idler. Apart from using the linear response analysis first introduced in Chapter 1 and then extended to the case of a pump-only condensate in Chapter 3, we also numerically solve the full driven-dissipative Gross-Pitaevskii equation. We show that, while the modulation patterns are present in all three condensates, their relative amplitudes depend on various factors. In particular, for the typical experimental conditions that favour parametric scattering, the signal has undetectable modulations, while the pump and idler show the same response.

In Chapter 5, we add a harmonic trap to the Harper-Hofstadter lattice model of Chapter 1. We discuss how the eigenstates of the new Hamiltonian can be seen as momentum-space Landau levels, by making use of the nontrivial topology of the Harper-Hofstadter energy bands. We then extend the model to include driving and dissipation, and finally present a proposal for the physical implementation of the model in state-of-the-art driven-dissipative photonic systems.

The source code belonging to Chapters 3, 4 and 5 is available online [42].

Part I

Condensed-matter systems

Chapter 1

Ultracold atomic gases

Laser cooling [43, 44] allowed achieving temperatures in the micro-Kelvin regime, and eventually led to the realization of optical lattices [45]. It also paved the way for more powerful cooling techniques, such as evaporative cooling, which made possible the Bose-Einstein condensation of dilute atomic gases [46, 47].

Ultracold gases have been at the forefront of simulating quantum phenomena with analogs throughout physics, from nonlinear optics to condensed matter systems [48]. In particular, their link to quantum simulation of condensed matter phenomena becomes obvious when adding optical lattice potentials [49], combined with synthetic magnetic fields [39, 40].

In this Chapter, we review the physics of ultracold atomic gases, with an emphasis on their link to hydrodynamic effects such as superfluidity, as well as their connection to traditional solid state lattice models such as the celebrated Harper-Hofstadter model which originally describes the single-particle physics of band electrons in intense magnetic fields.

This Chapter is organized as follows: in Section 1.1 we present a short history of Bose-Einstein condensation, describe its main features and state its formal definition in terms of the Penrose-Onsager criterion, leading to the weakly-interacting Bose gas paradigm and the Gross-Pitaevskii equation (Sec. 1.2), an essential theoretical tool for the mean-field description of atomic condensates. In Section 1.3 we introduce the linear response formalism, which proves useful for interpreting experiments where a weak perturbation is applied to the condensate. We employ this formalism in order to study a scattering problem concerning the flow of a BEC in the presence of a weak static defect (Sec. 1.4). In this context, we review Bogoliubov's excitation spectrum and its associated Landau criterion for superfluidity, followed by a detailed discussion on superfluidity and related phenomena, such as quantized vortices, in Sec. 1.5. We briefly touch on the subject of synthetic gauge fields for neutral atoms, before investigating the properties of BECs in periodic potentials created by optical lattices (Sec. 1.6). Finally, we combine the concepts of synthetic gauge fields and optical lattices in Section 1.7, where we show the main features of the Harper-Hofstadter model, which was

recently realized using atomic gases.

1.1 Bose-Einstein condensation

In 1925, Albert Einstein (prompted by the earlier work of the indian polyglot Satyendra Nath Bose) considered what would happen to a non-interacting bosonic gas of non-relativistic particles in the thermodynamic limit, as one lowers the temperature. He predicted the phenomenon we now call *Bose-Einstein condensation* (BEC), namely a phase transition to a new state of matter, in which a finite fraction of all the particles would occupy the same single-particle state. The transition occurs at fixed density below a critical temperature T_c or, alternatively, at fixed temperature, above a critical density. In particular, if we take N neutral particles in a cubic box of volume L^3, then they would predominantly occupy the zero-wavevector state $\boldsymbol{k} = 0$, and the critical temperature would be [50]

$$T_c \simeq 3.31 \frac{\rho^{2/3}\hbar^2}{m k_B} \tag{1.1}$$

with the density $\rho = N/L^3$ and m, k_B being the particle mass and Boltzmann's constant, respectively.

At its core, BEC is a paradigm of quantum statistical mechanics, stemming from the indistinguishability of elementary particles and the Bose-Einstein statistics that they obey. One can hand-wavingly deduce the critical temperature (or critical density) where quantum degeneracy would start playing a role in a many-body system, by arguing that the thermal de Broglie wavelength should be comparable to or greater than the inter-particle distance (which in our case is $\rho^{-1/3}$ on average) [27]. Apart from the numerical prefactor, we get the same answer as Eq. (1.1). While one may argue that elementary massive bosons do not exist, it is worth emphasizing that indistinguishability only plays a role when there is a finite probability for exchange processes to occur between the particles. In that sense, all odd-isotope alkali atoms under relevant experimental conditions (see below) effectively behave as bosons: their many-body wavefunction is symmetric under the exchange of any two such atoms.

Interestingly enough, BEC was considered by many at the time to be a pathological behaviour of the non-interacting gas, which would resolve once interactions were properly accounted for. In fact, it is well known that the ideal Bose gas has infinite compresibility. This pathology is cured by introducing a weak repulsive interaction between bosons, a regime where BEC survives, as we will see next.

Following Leggett, we characterise each of the N particles (assumed spinless, for simplicity) by a position vector $\boldsymbol{r}_i$, with the label i running from 1 to N. Any pure state s of the (now interacting) system – which can be also subjected to an external potential – can be described at time t by the many-body wavefunction $\Psi_s(\boldsymbol{r}_1, \boldsymbol{r}_2, \ldots, \boldsymbol{r}_N, t)$. Therefore, the most general state of the system (also called *mixed state*) can be written as a superposition of pure orthonormal states s with

different weights p_s. The *single-particle density matrix* $\hat{\rho}_1(\boldsymbol{r}, \boldsymbol{r}', t)$ represents the probability amplitude, at time t, of finding a specific particle at position $\boldsymbol{r}$, multiplied by the amplitude of finding it at $\boldsymbol{r}'$, and averaged over the positions of all the other particles:

$$\begin{aligned}\hat{\rho}_1(\boldsymbol{r}, \boldsymbol{r}', t) &\equiv N \sum_s p_s \int d\boldsymbol{r}_2 d\boldsymbol{r}_3 \ldots d\boldsymbol{r}_N \Psi_s^\star(\boldsymbol{r}, \boldsymbol{r}_2, \ldots, \boldsymbol{r}_N, t) \Psi_s(\boldsymbol{r}', \boldsymbol{r}_2, \ldots, \boldsymbol{r}_N, t) \\ &= \sum_i n_i(t) \phi_i^\star(\boldsymbol{r}, t) \phi_i(\boldsymbol{r}', t) \end{aligned} \tag{1.2}$$

where in the second line we have re-written the density matrix in diagonal form, introducing its eigenvalues n_i and eigenvectors ϕ_i, which form a complete orthonormal set at any time t (here i labels a good quantum number of the problem, i.e. momentum in a translationally-symmetric situation).

We are now ready to state the Penrose-Onsager criterion for condensation, first formulated in 1956: if at any given time t it is possible to find a complete orthonormal basis of states of $\hat{\rho}_1$ such that one and only one of these states has an eigenvalue of order N (the rest being of order 1), then we say the system exhibits BEC. One should note that this definition only applies to "simple" BEC, as opposed to the "fragmented" case (of no concern to us here), where two or more of the eigenvalues of the one-body density matrix are of order N.

We denote the single macroscopic eigenvalue of the density matrix by $N_0(t)$, and its corresponding eigenfunction by $\phi_0(\boldsymbol{r}, t)$. ϕ_0 is called the *condensate wavefunction* and the N_0 particles occupying it the *condensate*, while the ratio N_0/N is the *condensate fraction*. It is not necessarily true that $N_0 = N$, even at zero temperature. Also note that, while ϕ_0 behaves as a single-particle Schrödinger wavefunction, it is generally not an eigenfunction of the single-particle part of the Hamiltonian, or of any other simple operator for that matter, other than $\hat{\rho}_1$. Another useful quantity frequently found in the literature is the so-called *order parameter*, $\psi(\boldsymbol{r}, t) = \sqrt{N_0(t)}\phi_0(\boldsymbol{r}, t)$. We see that, while ϕ_0 is normalized to 1, ψ will be normalized to $N_0(t)$.

It is worth mentioning the existence of a theorem due to Hohenberg [51], stating that, in the thermodynamic limit, BEC cannot occur at a finite temperature in any system moving freely in space in less than three dimensions, irespective of the existence and/or sign of the interparticle interactions, as thermal fluctuations would destroy the condensate. Note that this theorem, however, only applies under equilibrium conditions, the nonequilibrium case still being an open question. Furthermore, there is no general proof that a realistic system of interacting bosonic particles must show BEC, even at zero temperature – the solid phase of ^{4}He constitutes an obvious counter-example.

Most gases, with the notable exception of ^{4}He, are solids at the densities and temperatures predicted by Eq. (1.1). That is why it took no less than 70 years between Einstein's original paper and the first experimental observation of BEC in an atomic gas. In 1995, the group of Eric Cornell and Carl Wieman succesfully

condensed a cloud of ^{87}Rb atoms [52] (closely followed by the group of Wolfgang Ketterle at MIT with ^{23}Na atoms [53]), by first bringing the system to a very low density, and then cooling it fast enough to prevent any recombination processes that would have lead to the formation of the solid phase. While other odd-isotope alkali elements, especially ^{23}Na or ^{7}Li, are also routinely used in experiments, the first non-alkali atom to be cooled into the BEC phase was hydrogen ^{1}H. Due to the extreme diluteness of these systems ($\rho < 10^{15}$ atoms/cm^3), the typical range of T_c is from 20 nK to a few μK. Achieving such ultra-low temperatures stimulated the development of novel experimental techniques, such as magnetic/laser trapping and evaporative cooling of atoms.

The very low densities of alkali gases also limit the range of available diagnostic techniques. The most commonly employed method in BEC experiments is optical absorption imaging, where one shines a laser on the gas and detects the percentage of transmitted power. The image is usually taken after removing the trap and allowing the gas to expand. This gives information about the gas density as a function of coordinates and time, with a spatial resolution of a few μm. In stark contrast to liquid ^{4}He, density-related information seems to be sufficient for most practical purposes.

1.2 Gross-Pitaevskii equation

As it turns out, many of the experimental results in ultracold gases can be interpreted on the basis of a single equation for the condensate wavefunction $\phi_0(\boldsymbol{r}, t)$. This equation, first derived in 1961 independently by Eugene Gross and Lev Pitaevskii, was originally intended as a phenomenological description of quantum vortices in the superfluid phase of liquid ^{4}He, below the lambda point. Since liquid helium is a strongly interacting system however, the GP equation turned out to be much better suited to alkali gases. Before giving the concrete formulation of the GP equation, we must first explore the nature of the inter-atomic interactions.

In dilute systems, the inter-atomic distance $d = \rho^{-1/3}$ is on the order of 1000 Å, while the range r_0 of the inter-atomic potential, namely the extent of the last bound state of the van der Waals interaction, is about 50-100 Å. As $d \gg r_0$, the probability of three-atom colissions is substantially diminished. This justifies limiting ourselves to a binary (instead of three-body or more) scattering problem: consider two atoms, separated by a relative distance r and interacting in three dimensions through a potential $V(r)$. We can therefore decouple their center-of-mass motion from their relative one and write a Schrödinger equation for the scattering states $\psi(r)$.

For temperatures below T_c, the thermal de Broglie wavelength $\lambda_T > d$ (as mentioned in Sec. 1.1), meaning all significantly occupied states will have small wavevectors, $k \ll r_0^{-1}$. This directly translates to a low relative kinetic energy, and hence small relative wavevectors, for the scattering problem outlined above.

However, we know from scattering theory that the probability for two atoms, with relative angular momentum ℓ, of being separated by a distance $r \ll k^{-1}$ is proportional to $(kr)^{2\ell}$, therefore essentially negligible in the limit $kr_0 \ll 1$. That is of course, unless $\ell = 0$, meaning their relative state is s-wave, which is what we will assume from now on. Since $r_0 \ll d$, one can use the asymptotic expression for $\psi(r)$, which only depends on the scattering amplitude. At small wavevectors, this amplitude can be safely replaced by the *s-wave scattering length* a_s, which will encapsulate all the interaction effects on macroscopic properties of the atomic gas.

One can now replace the two-body potential $V(r)$ with an effective interaction, $V_{\text{eff}}(r)$, provided it gives the same scattering length. The limit of small wavevectors prompts us to only consider the lowest Fourier component of V_{eff}, equivalent in real space to a contact interaction[1] $V_{\text{eff}}(r) = g\delta(r)$, where we have introduced the interaction coupling constant g, whose value can be calculated using the first-order Born approximation [50]

$$g = \frac{4\pi\hbar^2}{m} a_s \tag{1.3}$$

The scattering length a_s therefore becomes the small parameter of the theory of weakly-interacting ultracold gases, and the validity of the Born approximation rests on the following two conditions

$$k|a_s| \ll 1 \tag{1.4}$$

$$|a_s| \ll \rho^{-1/3} \tag{1.5}$$

Eq. (1.5) is called the "diluteness condition", and it paves the way to various mean-field approaches, such as the GP equation.

Formally, the GP equation corresponds to the lowest-order expansion in a_s of the more exact Bogoliubov theory. However, we will try to give a hand-waving justification of it for the zero-temperature case. At $T = 0$, all N particles are in the condensate, therefore one could neglect all inter-particle correlations and introduce the simplest (Hartree-Fock) ansatz, expressing the ground state many-body wavefunction Ψ in the symmetrized form

$$\Psi(\boldsymbol{r}_1, \boldsymbol{r}_2, \ldots, \boldsymbol{r}_N, t) = \prod_{i=1}^{N} \phi_0(\boldsymbol{r}_i, t) \tag{1.6}$$

As mentioned in Sec. 1.1, the single-particle state ϕ_0 (now occupied by all the bosons) obeys a Schrödinger-like equation, to which we must add the energy of the effective binary interactions. In mean-field, these interactions contribute the

[1] Technically, one should also include a regularizing part in order to remove any $1/r$ divergencies of the wavefunction.

equivalent of a one-particle potential term proportional to $|\phi_0|^2$. [27] Together with the kinetic part, this results in the nonlinear equation[2]

$$i\hbar\partial_t\phi_0(\boldsymbol{r},t) = \left[-\frac{\hbar^2\nabla^2}{2m} + U(\boldsymbol{r},t) + gN|\phi_0(\boldsymbol{r},t)|^2\right]\phi_0(\boldsymbol{r},t) \tag{1.7}$$

where we have also included an external potential $U(\boldsymbol{r},t)$, normally used to model harmonic trapping of the gas. Note that Eq. (1.7) is valid for physics occuring over distances much larger than the scattering length a_s, which in turn must be smaller than the typical range r_0 of the potential $U(\boldsymbol{r},t)$.

Eq. (1.7) is the time-dependent Gross-Pitaevskii (TDGP) equation, a mean-field result where the condensate wavefunction ϕ_0 must be calculated self-consistently. It is important to emphasize that the TDGP equation is also valid at nonzero temperatures $T \ll T_c$, provided that the density of non-condensed particles is much smaller than the condensate density. In that case, the condensate number N_0 is smaller (but still on the order of) the total particle number N. Finally, one must note that the nonlinearity of Eq. (1.7) builds a bridge connecting BEC to nonlinear optics, where a similar relation is used, under the name of *nonlinear Schrödinger equation*.

In case the external potential U does not depend explicitly on time, the stationary solutions of Eq. (1.7) evolve with a trivial phase factor $\exp(-i\mu t/\hbar)$. This yields a time-independent GP equation for $\phi_0(\boldsymbol{r})$ (we set $\hbar = 1$ from here on)

$$\mu\phi_0(\boldsymbol{r}) = \left[-\frac{\nabla^2}{2m} + U(\boldsymbol{r}) + gN_0|\phi_0(\boldsymbol{r})|^2\right]\phi_0(\boldsymbol{r}) \tag{1.8}$$

where μ is chemical potential of the gas, the energy required to add one more particle to the system.[3]

1.3 Linear response theory

Following loosely the formalism presented in Ref. [54], we now let $\phi_0(\boldsymbol{r})$ be the steady state solution to the GP equation in the time-independent trapping potential $U_0(\boldsymbol{r})$

$$H_{\mathrm{GP}}\phi_0 = 0 \tag{1.9}$$

with the GP Hamiltonian defined as

$$H_{\mathrm{GP}} \equiv -\frac{\nabla^2}{2m} + U_0 + gN_0|\phi_0|^2 - \mu \tag{1.10}$$

This Hamiltonian describes a bosonic condensate of N_0 particles with contact interactions quantified by g, and chemical potential μ. Now consider adding a small

[2] We have tacitly assumed that N is large enough, such that $N - 1 \approx N$.

[3] Technically, it is the Lagrange multiplier associated to the conservation of particle number N_0, and can be shown to be very close to the actual chemical potential in the thermodynamic limit. [54]

time-dependent perturbation on top of the trap, giving $U(\boldsymbol{r},t) = U_0(\boldsymbol{r}) + \delta U(\boldsymbol{r},t)$. We are interested in the response of the condensate to this perturbation. For weak perturbations, we can perform a linearization of the GP equation Eq. (1.9) around the stationary solution ϕ_0 – an approach known in the literature as the "linear response" formalism. The condensate wavefunction $\phi(\boldsymbol{r},t)$ evolves according to

$$i\partial_t \phi = \left[-\frac{\nabla^2}{2m} + U + gN_0|\phi|^2 - \mu \right] \phi \tag{1.11}$$

We assume a small deviation of the wavefunction from its initial steady state

$$\phi(\boldsymbol{r},t) = \phi_0(\boldsymbol{r}) + \delta\phi(\boldsymbol{r},t) \tag{1.12}$$

such that we can expand Eq. (1.11) and keep only linear terms in $\delta\phi$ and δU. We get

$$i\partial_t \delta\phi = \left[-\frac{\nabla^2}{2m} + U_0 - \mu \right] \delta\phi + 2gN_0\phi_0^\star\phi_0\delta\phi + gN_0\phi_0^2\delta\phi^\star + \delta U\phi_0 \tag{1.13}$$

Note that Eq. (1.13) is not strictly linear due to the coupling of $\delta\phi$ to $\delta\phi^\star$. To restore linearity, we consider the functions $\delta\phi$ and $\delta\phi^\star$ as being independent and write the linear system

$$i\partial_t \begin{pmatrix} \delta\phi(\boldsymbol{r},t) \\ \delta\phi^\star(\boldsymbol{r},t) \end{pmatrix} = \mathcal{L}_{GP} \begin{pmatrix} \delta\phi(\boldsymbol{r},t) \\ \delta\phi^\star(\boldsymbol{r},t) \end{pmatrix} + \begin{pmatrix} S(\boldsymbol{r},t) \\ -S^\star(\boldsymbol{r},t) \end{pmatrix} \tag{1.14}$$

where we have introduced the linear operator

$$\mathcal{L}_{\mathrm{GP}} = \begin{pmatrix} H_{\mathrm{GP}} + gN_0|\phi_0|^2 & gN_0\phi_0^2 \\ -gN_0\phi_0^{\star 2} & -\left[H_{\mathrm{GP}} + gN_0|\phi_0|^2\right]^\star \end{pmatrix} \tag{1.15}$$

and the source term $S(\boldsymbol{r},t) = \delta U(\boldsymbol{r},t)\phi_0(\boldsymbol{r})$. Note that $\mathcal{L}_{\mathrm{GP}}$ is a non-Hermitian operator!

We now consider the eigenvalue equation for the operator $\mathcal{L}_{\mathrm{GP}}$

$$\mathcal{L}_{\mathrm{GP}}|\psi_k^R\rangle = \epsilon_k|\psi_k^R\rangle \tag{1.16}$$

with $|\psi_k^R\rangle$ being the right eigenvector and ϵ_k its corresponding eigenvalue

$$|\psi_k^R\rangle = \begin{pmatrix} |u_k\rangle \\ |v_k\rangle \end{pmatrix} \tag{1.17}$$

Similarly, we also introduce the left eigenvector, obeying $\mathcal{L}_{\mathrm{GP}}^\dagger|\psi_k^L\rangle = \epsilon_k^\star|\psi_k^L\rangle$, and the orthonormality condition $\langle\psi_k^L|\psi_q^R\rangle = \delta_{k,q}$.

Notice that $\mathcal{L}_{\mathrm{GP}}$ and $\mathcal{L}_{\mathrm{GP}}^\dagger$ are connected by the unitary transformation[4]

$$\eta\mathcal{L}_{\mathrm{GP}}\eta^\dagger = \mathcal{L}_{\mathrm{GP}}^\dagger \tag{1.18}$$

[4]Note that this holds as long as the Hamiltonian H_{GP} only contains real terms.

where $\eta = \sigma_3 = \begin{pmatrix} 1 & 0 \\ 0 & -1 \end{pmatrix}$ is the third Pauli matrix. We say that $\mathcal{L}_{\rm GP}$ is η-Hermitian, meaning that one can define a new scalar product $\langle\cdot|\cdot\rangle_\eta \equiv \langle\cdot|\eta\cdot\rangle$ with a different signature, such that $\langle\cdot|\mathcal{L}_{\rm GP}\cdot\rangle_\eta = \langle\mathcal{L}_{\rm GP}\cdot|\cdot\rangle_\eta$. The operator η is usually called the metric operator, and, not suprisingly in our case, it is the same as the one of the scalar Klein-Gordon equation. A pseudo-Hermitian operator usually also posesses antilinear symmetries, and as we will see below this is also the case for $\mathcal{L}_{\rm GP}$. Interestingly, for operators with a real spectrum, it can be shown that one can define another metric η_+, which guarantees a positive-definite inner product, or, in other words, $\langle\psi|\psi\rangle_{\eta_+} > 0$ (provided $\psi \neq 0$ of course). This can be used to formulate a probabilistic quantum theory for the new wave-functions ψ^R and ψ^L. For the general theory and properties of pseudo-Hermitian operators, we point the interested reader to Ref. [55].

Using Eq. (1.18), we get the general form of the left eigen-vectors as

$$\langle\psi_k^L| = \mathcal{N}_k\left(\langle u_k|, -\langle v_k|\right) \tag{1.19}$$

with $\mathcal{N}_k$ a normalization factor. We can chose $\mathcal{N}_k = \pm 1$ and group the eigenvalues of $\mathcal{L}_{\rm GP}$ into 3 families, according to the quantity

$$n_k = \langle u_k|u_k\rangle - \langle v_k|v_k\rangle \tag{1.20}$$

We therefore have: the "+" family, corresponding to $n_k = +1$, the "−" family, such that $n_k = -1$ and the "0" family, with $n_k = 0$.

We are now ready to write the completeness relation

$$\sum_k |\psi_k^R\rangle\langle\psi_k^L| = \mathbb{I} \tag{1.21}$$

Using Eq. (1.21), we can decompose any column vector as[5]

$$\begin{pmatrix} |l_1\rangle \\ |l_2\rangle \end{pmatrix} = \sum_{k\in\text{“+”family}} \left[\langle u_k|l_1\rangle - \langle v_k|l_2\rangle\right] \begin{pmatrix} |u_k\rangle \\ |v_k\rangle \end{pmatrix} + \sum_{k\in\text{“−”family}} \left[\langle v_k|l_2\rangle - \langle u_k|l_1\rangle\right] \begin{pmatrix} |u_k\rangle \\ |v_k\rangle \end{pmatrix} \tag{1.22}$$

There is now a further symmetry of $\mathcal{L}_{\rm GP}$ that we can exploit in our problem, a sort of time-reversal "spin"-flip symmetry, namely

$$\Theta\mathcal{L}_{\rm GP}\Theta^\dagger = -\mathcal{L}_{\rm GP} \tag{1.23}$$

where $\Theta = \sigma_1\mathcal{K}$, with $\sigma_1 = \begin{pmatrix} 0 & 1 \\ 1 & 0 \end{pmatrix}$ the first Pauli matrix and $\mathcal{K}$ the complex conjugation antilinear operator. This results in a duality between the "+" family

[5] The modes in the "0" family do not appear in this expansion as their components live in the space orthogonal to the one of our solution.

with eigenvectors (u_k, v_k) and energy ϵ_k and the "$-$" family with eigenvectors $(v^\star_{-k}, u^\star_{-k})$ and energy $-\epsilon^\star_{-k}$.

We can now finally project Eq. (1.14) onto the eigenvectors of $\mathcal{L}_{\rm GP}$. Using the above-mentioned duality and Eq. (1.22), we get

$$\begin{pmatrix} \delta\phi(\boldsymbol{r},t) \\ \delta\phi^\star(\boldsymbol{r},t) \end{pmatrix} = \sum_{k\in\text{“+”family}} b_k(t) \begin{pmatrix} u_k(\boldsymbol{r}) \\ v_k(\boldsymbol{r}) \end{pmatrix} + b^\star_{-k}(t) \begin{pmatrix} v^\star_{-k}(\boldsymbol{r}) \\ u^\star_{-k}(\boldsymbol{r}) \end{pmatrix} \tag{1.24}$$

with the complex amplitudes b_k satisfying

$$i\frac{d}{dt}b_k(t) = \epsilon_k b_k(t) + s_k(t) \tag{1.25}$$

where we introduced

$$s_k(t) = (\langle u_k|, -\langle v_k|) \begin{pmatrix} |S(t)\rangle \\ -|S^\star(t)\rangle \end{pmatrix} \tag{1.26}$$

1.4 Cherenkov emission of Bogoliubov excitations

We now turn to applying the formalism developed in Sec. 1.3 to a concrete physical example, namely a flowing condensate scattering against a static defect [56]. The BEC[6] is therefore in a state with well-defined momentum, described by the plane wave

$$\phi_0(\boldsymbol{r},t) = \psi_0 \exp\left(i\boldsymbol{k_0}\boldsymbol{r} - \omega_0 t\right) \tag{1.27}$$

and a chemical potential $\mu = k_0^2/(2m) + g\rho_0$. Since we have no trap, $U_0(\boldsymbol{r}) = 0$, and Eq. (1.9) produces the equation of state

$$\omega_0 - \left(\frac{k_0^2}{2m} + g\rho_0\right) = 0 \tag{1.28}$$

where we have introduced the condensate density $\rho_0 \equiv N_0|\phi_0|^2$.

We now introduce a weak perturbation in the form of a static localized defect potential $\delta U(\boldsymbol{r},t) = V_d(\boldsymbol{r})$, which can represent for instance a laser spot depleting a small area of the condensate, as shown in Fig. 1.1.

Using Eq. (1.28), the GP Hamiltonian becomes $H_{\rm GP} = -\frac{\nabla^2}{2m} - \frac{k_0^2}{2m}$ and the source term $S(\boldsymbol{r}) = \psi_0 V_d(\boldsymbol{r}) \exp\left(i\boldsymbol{k_0}\boldsymbol{r}\right)$. We now get the linear operator for our problem in the form

$$\mathcal{L} = \begin{pmatrix} -\frac{\nabla^2}{2m} - \frac{k_0^2}{2m} + g\rho_0 & gN_0\psi_0^2 \exp\left(2i\boldsymbol{k_0}\boldsymbol{r}\right) \\ -gN_0\psi_0^{\star 2} \exp\left(-2i\boldsymbol{k_0}\boldsymbol{r}\right) & -\left[-\frac{\nabla^2}{2m} - \frac{k_0^2}{2m} + g\rho_0\right] \end{pmatrix} \tag{1.29}$$

[6] We integrate all density profiles along the z direction, resulting in an effective 2-dimensional description.

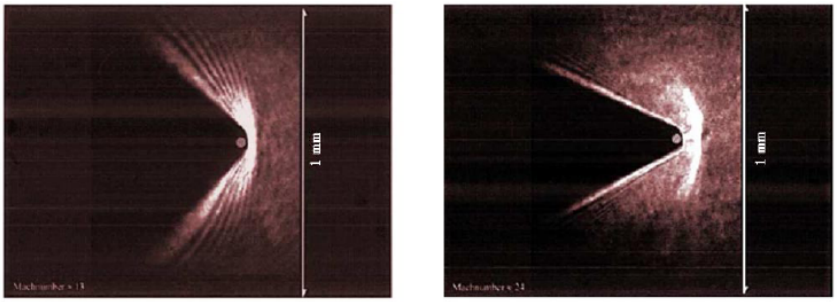

Figure 1.1: Density profiles of an expanding BEC hitting a stationary defect created by the repulsive potential of a blue-detuned laser beam. The condensate has different speeds in the two panels, moving roughly twice as fast in the right-panel. Notice the Mach cone formed behind the defect, which gets narrower as the condesate moves faster. From Ref. [56].

Notice that, due to the presence of the off-diagonal exponential terms, $\mathcal{L}$ does not commute with the momentum operator, which is the generator of the spatial translation group. Luckily, however, we can restore translational invariance by a simple unitary transformation, as shown below.

Using the standard commutation relations, one can show that, for a constant wavevector $\boldsymbol{k_0}$, the unitary operator[7]

$$\hat{T}(\boldsymbol{k_0}) = \exp\left(-i\boldsymbol{k_0}\hat{\boldsymbol{r}}\right) \tag{1.30}$$

performs a translation in momentum space, $\hat{T}(\boldsymbol{k_0})|\boldsymbol{k}\rangle = |\boldsymbol{k} - \boldsymbol{k_0}\rangle$, with the ket $|\boldsymbol{k}\rangle$ representing a single particle state with wavevector $\boldsymbol{k}$ such that $\hat{\boldsymbol{k}}|\boldsymbol{k}\rangle = \boldsymbol{k}|\boldsymbol{k}\rangle$. Using the definitions above, one can easily obtain the commutator

$$\left[\hat{\boldsymbol{k}}, \hat{T}(\boldsymbol{k_0})\right] = -\boldsymbol{k_0}\hat{T}(\boldsymbol{k_0}) \tag{1.31}$$

This allows us to rewrite the following expressions

$$\begin{aligned} \hat{T}^\dagger(\boldsymbol{k_0})\hat{\boldsymbol{k}}\hat{T}(\boldsymbol{k_0}) &= \hat{\boldsymbol{k}} - \boldsymbol{k_0}\hat{\mathbb{I}} \\ \hat{T}(\boldsymbol{k_0})\hat{\boldsymbol{k}}\hat{T}^\dagger(\boldsymbol{k_0}) &= \hat{\boldsymbol{k}} + \boldsymbol{k_0}\hat{\mathbb{I}} \end{aligned} \tag{1.32}$$

We now recognize the two exponentials in Eq. (1.29) as being the real-space representation of $\hat{T}^2(\boldsymbol{k_0})$ and its hermitian conjugate. This motivates us to define the following unitary operator

$$\hat{\mathcal{T}}(\boldsymbol{k_0}) = \begin{pmatrix} \hat{T}(\boldsymbol{k_0}) & 0 \\ 0 & \hat{T}^\dagger(\boldsymbol{k_0}) \end{pmatrix} \tag{1.33}$$

[7]The hat symbol denotes operators in the relevant Hilbert space.

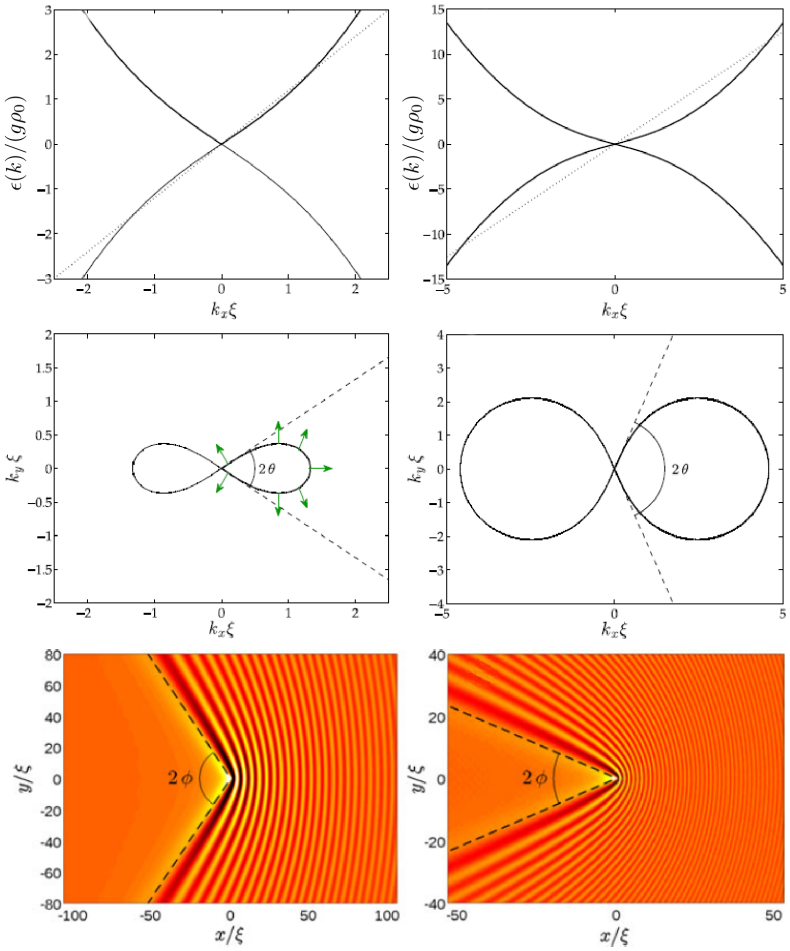

Figure 1.2: *Top panels:* Bogoliubov dispersion Eq. (1.37). The dotted lines indicate the $\boldsymbol{v}_0\boldsymbol{k}$ plane. *Middle panels:* Locus Γ of intersection of the 2D dispersion with the $\boldsymbol{v}_0\boldsymbol{k}$ plane. Green arrows are normal to Γ, while the dashed lines indicate the Cherenkov cone. *Bottom panels:* Real-space density modulation, with a δ–defect at $(0, 0)$. Dashed lines show the Mach cone. Left column panels are for $v_0 = 1.2c_s$, and right column for $v_0 = 2.5c_s$. From Ref. [57].

such that a unitary transformation of our operator $\mathcal{L}$ now restores translational

symmetry. Indeed, one can see that

$$\hat{\mathcal{T}}\hat{\mathcal{L}}\hat{\mathcal{T}}^{\dagger} = \begin{pmatrix} \frac{\left(\hat{\boldsymbol{k}}+\boldsymbol{k_0}\right)^2}{2m} - \frac{k_0^2}{2m} + g\rho_0 & gN_0\psi_0^2 \\ -gN_0\psi_0^{\star 2} & -\left[\frac{\left(\hat{\boldsymbol{k}}-\boldsymbol{k_0}\right)^2}{2m} - \frac{k_0^2}{2m} + g\rho_0\right] \end{pmatrix} \tag{1.34}$$

where we have made use of Eqs. (1.32) and we have written $\hat{\mathcal{L}}$ in a base-independent representation. In the subspace of momentum eigenstates $|\boldsymbol{k}\rangle$, we can write the (right-)eigenvalue equation corresponding to Eq. (1.34) as

$$\mathcal{L}_{\mathrm{GP}}[k] \begin{pmatrix} U_\sigma(k) \\ V_\sigma(k) \end{pmatrix} = \epsilon_\sigma(k) \begin{pmatrix} U_\sigma(k) \\ V_\sigma(k) \end{pmatrix} \tag{1.35}$$

where we have recovered the matrix representation of Eq. (1.15), and introduced the notation

$$\omega_\sigma(\boldsymbol{k}) = \boldsymbol{v}_0\boldsymbol{k} + \epsilon_\sigma(k) \tag{1.36}$$

Here $\sigma = \pm$ labels the 2 different eigenmodes, and we defined the condensate speed $\boldsymbol{v}_0 \equiv \frac{\boldsymbol{k}_0}{m}$.

Notice that the $k = 0$ mode has only one eigenvector. However, one can safely exclude it as this mode does not imply energy or momentum transport. Excluding the $k = 0$ point, one can then solve Eq. (1.35), obtaining the celebrated Bogoliubov excitation spectrum

$$\epsilon_\sigma(k) = \sigma\left[\frac{k^2}{2m}\left(\frac{k^2}{2m} + 2g\rho_0\right)\right]^{\frac{1}{2}} \tag{1.37}$$

with $\sigma = \pm$, as before. Here k represents the momentum of the quasiparticle excitation with respect to the momentum k_0 of the condensate. Note that the complex amplitudes $U_\sigma(k)$ and $V_\sigma(k)$ only depend on the absolute value of $\boldsymbol{k}$, while the (real) spectrum of Eq. (1.34), $\omega_\sigma(\boldsymbol{k})$, is the Bogoliubov spectrum with an additional Galilean boost $\boldsymbol{v}_0\boldsymbol{k}$.

We can now further simplify the problem. As can be seen from Eq. (1.23), the 2 eigen-families σ and $-\sigma$ are linked by a duality, stemming from the $\mathcal{PT}$ symmetry[8] of the Bogoliubov operator $\mathcal{L}$. We therefore drop the subscript σ and make the convention that $(U, V) \equiv (U_+, V_+)$.

The Bogoliubov spectrum Eq. (1.37) is shown in the top row of Fig. 1.2, for two different values of v_0, which sets the slope of the dotted lines (indicating the $\boldsymbol{v}_0\boldsymbol{k}$ plane). In the non-interacting case $g = 0$ and the spectrum reduces to a simple parabola characterising a free particle. For repulsive interactions, $g > 0$ and we can distinguish two qualitatively different domains, after first introducing the typical length scale of the problem, called the *healing length*. The healing

[8]This can be actually formally proven after defining the parity and time-reversal operators corresponding to our problem. For details, see Ref. [55].

length ξ is a measure of the distance over which the condensate density recovers its equilibrium value ρ_0 when forced to vary away from this value. For example, in a box the boundary conditions fix the density to zero at the positions of the walls. In mathematical terms,

$$\frac{1}{m\xi^2} = g\rho_0 \tag{1.38}$$

We first explore the domain of small momenta, $k\xi \ll 1$, which is characterised by a linear behaviour of the dispersion, $\epsilon(k) \simeq kc_s$, that implies the propagation of low-energy excitations in the form of *sound waves*, with a velocity[9] c_s given by

$$mc_s^2 = g\rho_0 \tag{1.39}$$

The *Landau criterion* for superfluidity [58] determines the maximum velocity at which a weak impurity can travel through the condensate without dissipating energy. In order for it to dissipate energy, such an impurity must be able to create quasiparticle excitations in the condensate. Conservation of energy and momentum then results in a critical velocity

$$v_c = \min_k \left[\frac{\epsilon(k)}{k}\right] \tag{1.40}$$

below which no dissipation can occur. In our case, this velocity is precisely equal to the speed of sound, $v_c = c_s$. Furthermore, the two situations, the one of a particle moving through the condensate, or of the condensate moving against a fixed defect, are physically equivalent, being connected by a Galilean transformation. We can therefore conclude that we must have $v_0 \geq c_s$ in order to observe any propagating perturbation, otherwise for $v_0 < c_s$ the superfluid will remain unperturbed. Before moving on, it is worth noting that the Landau criterion has some asociated caveats. One is assuming that the only excitations are density excitations, phonons. Thus one is, for example, neglecting the nucleation of vortices by a macroscopic defect with a size comparable to the healing length, which would lower the effective critical velocity. Vortices would furthermore also break the translational invariance along the transverse directions, an invariance that we already made use of. The second caveat is that quantum fluctuations are also neglected. As seen in Ref. [59], they could lead to nonzero dissipation even at sub-sonic speeds.

The second domain of interest is the one of large momenta, $k\xi \gg 1$. Looking at Eq. (1.35), one notices that the only k-dependent parts of $\mathcal{L}_{\rm GP}[k]$ are the diagonal terms. These terms have opposite sign, so the off-diagonal coupling between $U(k)$ and $V(k)$ becomes highly off-resonant at large k. Completely neglecting it gives the free-particle-like shifted parabola $\epsilon(k) \simeq k^2/(2m) + g\rho_0$, with $U(k) \simeq 1$

[9] The sound velocity here is measured in the condensate rest-frame ($k_0 = 0$).

and $V(k) \simeq 0$. The discontinuity in the spectrum at zero momentum can be explained by the fact that the diagonal and off-diagonal parts of $\mathcal{L}_{\mathrm{GP}}[0]$ are equal in absolute value.

In order to obtain the defect-induced density perturbation, we must now also determine the eigenvectors of the problem. Making use of Eq. (1.18), we can act with σ_3 on the eigenstates of $\mathcal{L}_{\mathrm{GP}}$ to obtain the ones of $\mathcal{L}_{\mathrm{GP}}^{\dagger}$. This finally leads us to a biorthonormal basis $\left\{|\psi_\sigma^R(\boldsymbol{k})\rangle, |\psi_\sigma^L(\boldsymbol{k})\rangle\right\}$, containing 4 basis vectors

$$\left\{\begin{pmatrix} U(k) \\ V(k) \end{pmatrix}, \begin{pmatrix} V^\star(k) \\ U^\star(k) \end{pmatrix}, \begin{pmatrix} U(k) \\ -V(k) \end{pmatrix}, \begin{pmatrix} -V^\star(k) \\ U^\star(k) \end{pmatrix}\right\} \bigotimes |\boldsymbol{k}\rangle \tag{1.41}$$

which fulfill the orthonormality condition

$$\langle \psi_{\sigma'}^L(\boldsymbol{k}')|\psi_\sigma^R(\boldsymbol{k})\rangle = \delta_{\sigma,\sigma'}\delta^2(\boldsymbol{k}-\boldsymbol{k}') \tag{1.42}$$

and the completeness relation

$$\sum_{\sigma=\pm}\int d^2\boldsymbol{k}\; |\psi_\sigma^R(\boldsymbol{k})\rangle\langle\psi_\sigma^L(\boldsymbol{k})| = 1 \tag{1.43}$$

provided of course that we normalize in such a way that $|U(k)|^2 - |V(k)|^2 = 1$. In this basis, the spectral decomposition of Eq. (1.34) is the diagonal form

$$\hat{\mathcal{T}}\hat{\mathcal{L}}\hat{\mathcal{T}}^\dagger = \sum_{\sigma=\pm}\int d^2\boldsymbol{k}\; \omega_\sigma(\boldsymbol{k})|\psi_\sigma^R(\boldsymbol{k})\rangle\langle\psi_\sigma^L(\boldsymbol{k})| \tag{1.44}$$

The concrete form of $\mathcal{L}_{\mathrm{GP}}[k]$, coupled with the normalization condition Eq. (1.20), determines the eigenvectors of the "+" family up to a phase factor. Indeed, one can choose $|U(k)| \pm |V(k)| = f(k)^{\pm\frac{1}{4}}$, with

$$f(k) = \frac{k^2/(2m)}{k^2/(2m) + 2g\rho_0} \tag{1.45}$$

Furthermore, in case the Hamiltonian doesn't contain any time-reversal symmetry-breaking terms, one can chose $U(k)$ and $V(k)$ to be real quantities, without loss of generality.

It is now straightforward to solve the linearized evolution equation Eq. (1.14). In particular, for a localized static defect potential $V_d(\boldsymbol{r}) = g_V\delta^2(\boldsymbol{r})$, quasiparticle modes at all wavevectors k are excited.[10] The source term is time-independent, and hence the quasi-particle amplitudes of Eq. (1.25) have the simple form $b(\boldsymbol{k}) = -s(\boldsymbol{k})/\omega(\boldsymbol{k})$. Equivalently, we can obtain the defect-induced perturbation of the wavefunction from its initial steady state by directly inverting Eq. (1.44) and then reversing the unitary transformation that was applied to obtain Eq. (1.34).

[10] If one wishes to selectively excite a pair of modes, one can use a periodic potential, following, for example, Ref. [60].

Whichever route we take, it is clear that the final answer will have a resonant structure, containing $\omega(\boldsymbol{k})$ in the denominator, hence the dominant modes will be the ones that satisfy $\omega(\boldsymbol{k}) = 0$.

We must also mention the subject of *adiabatic switching* at this point. Adiabatic switching is neccesary to causally distinguish the past from the future, making sure that the time $t = -\infty$ is prior to that of the occurence of any cause (in our case the defect) giving rise to the effect (pertubation of the condensate density). The way to achieve this in practice is by shifting the real poles of the Bogoliubov dispersion Eq. (1.37) into the lower half of the complex plane by an infinitesimal amount, $\epsilon(k) \to \epsilon(k) - i0^+$. This corresponds to a weak damping of the plane wave solution and ensures that no Bogoliubov excitations were present at $t = -\infty$.

We show the defect-induced perturbation of the condensate density in the bottom row of Fig. 1.2, for two distinct values of the condensate speed v_0. Rather than giving its full analytical expression, it is more instructive to present a geometrical construction, detailed in Ref. [57], that can shed light on the main features of the condensate response. We have already identified the importance of the poles of $\omega(\boldsymbol{k})$; the solutions of $\epsilon(k) + \boldsymbol{v}_0\boldsymbol{k} = 0$ can be visualized if one plots the intersection of the Bogoliubov dispersion surface $\epsilon(k)$ with the $\boldsymbol{v}_0\boldsymbol{k}$ plane. The locus of this intersection is a closed curve that we will denote by Γ and that is plotted in the middle row of Fig. 1.2. Making the connection with the Landau criterion presented earlier, we can identify two regimes. For small velocities $v_0 < c_s$ we have the *sub-sonic* regime, where Γ is a single point at the origin. Consequently, one can observe superfluid-like behaviour with no propagating density modulation. The modulation will stay localized in the vecinity of the defect, and, in the Galilean-equivalent problem of a particle moving through the condensate, it would renormalize the particle mass. [59]

As we gradually increases the condensate speed, and hence the slope of the $\boldsymbol{v}_0\boldsymbol{k}$ plane, this plane will touch the surface of the dispersion relation when $v_0 = c_s$, marking the entry into the *super-sonic* (dissipative) regime. Further increasing the speed will increase the size of Γ, as can be seen in Fig. 1.2. The green arrows, orthogonal to the curve Γ at each point, represent the group velocity of the Bogoliubov mode at that particular k-value. They show the direction of propagation of the density perturbation away from the defect, up to infinity. It is the interference of these propagating modes that we see as the real-space density pattern. Note that the locus Γ has two distinct regions, inherited from the linear and quadratic domains of the dispersion Eq. (1.37).

The linear region of Γ, close to the origin, is characterised by essentially the same physics as the Cherenkov effect in non-dispersive media [61]. The Charenkov effect consists in the emission of electromagnetic radiation by a charged particle moving relativistically through a dielectric medium at a velocity higher than the (phase) velocity of light in that medium. The emission is concentrated into a *Cherenkov cone* in momentum space, of aperture 2θ, where $\cos\theta = c/v$. [62] The higher the particle speed v with respect to the speed of light c, the wider the

angle θ between the emission and the direction of motion. The Cherenkov cone is depicted by the dashed lines in the middle panels of Fig. 1.2, and the angle θ in our case is of course given by $\cos\theta = c_s/v_0$. Due to the momentum-space singularity at the origin, the group velocity has a jump, defining a whole region of space where no phonons are emitted. This corresponds in real-space to the so-called *Mach cone*, named in analogy to the cone that is created by a supersonic aircraft (since we are dealing with terminology, it is worth noting that the ratio v_0/c_s goes by the name of *Mach number*). The Mach cone is depicted by dashed lines in the bottom panels of Fig. 1.2: as its aperture 2ϕ is quantified by $\sin\phi = c_s/v_0$, that means that, the faster the fluid, the narrower the cone will be.

The high-momentum, rounded region of Γ, which corresponds to the quadratic single-particle-like dispersion, has no equivalent in Cherenkov physics. It is responsible for the hyperbolic-like wavefronts[11], emitted in the positive $\hat{\boldsymbol{x}}$ direction (upstream). The physical origin of these rounded waves lies in the interference between the coherent matter wave of the BEC and the wave scattered off the defect. It it worth noting that the curve Γ also helps one determine the spacing between the emitted wavefronts, which is inversely proportional to the value of the momentum at the particular point on Γ that corresponds to the wave propagation direction. In practice, we see for example that the spacing along $y = 0$, in the positive $\hat{\boldsymbol{x}}$ direction, is wider in the left-bottom panel than in the right one.

Aside from being just a useful geometrical construction, the locus Γ can actually be observed in scattering experiments, both in the context of atomic condensates, as well as for microcavity polaritons (Chapter 2), where it takes the name of Rayleigh scattering ring.

Before closing this Section, it is worth making the connection between the Cherenkov waves shown in the bottom panels of Fig. 1.2 and the more mundane example of surface waves created at the interface between a fluid layer and a gas. We first need to define the *capillary length* $\ell_\gamma = \sqrt{\gamma/(G\rho)}$, with γ the surface tension of the fluid-gas interface, G the gravitational constant, and ρ the fluid density. Now, if the height h of the fluid layer in question is smaller than $\sqrt{3}\ell_\gamma$, the fluid dispersion is dominated by capillary effects, and its form is similar to Eq. (1.37) (see Ref. [57]). But we have just seen that the form of the dispersion (more precisely, its intersection with the $\boldsymbol{v}_0\boldsymbol{k}$ plane) determines the shape of the ougoing waves. This means that, for very shallow fluids, we will observe similar wavefronts to the ones of Fig. 1.2. More concretely, for the water-air interface, a thickness of $h = 1$ millimeter and a speed of $v_0 = 14$ cm/s should do the trick!

1.5 Superfluidity

The history of superfluidity is intrinsically linked to that of helium, the liquefaction of which was first achieved in 1908 by Kammerlingh-Onnes. This ushered in

[11] The wavefronts are actually parabolic in the non-interacting limit of $g = 0$.

a new era of low-temperature physics, and it was soon realized that the thermal expansion coefficient of liquid ^{4}He had a discontinuity at the so-called lambda-(λ-)point. This lead to the classification of liquid helium in two distinct phases, above (He-I) and below (He-II) the critical temperature $T_\lambda = 2.2K$. It was in this context that, 30 years later, Kapitza in Moscow and Allen and Misener in Cambridge investigated the flow of He-II through a narrow opening between two large containers. Observing that the fluid essentially behaves as having no viscosity[12], Kapitza introduced the term "superfluidity" in analogy to the superconductivity observed in charged systems. It turned out to be an inspired analogy, as the prevalent view of the scientific community nowadays is that the two are essentially the same phenomenon, stemming from BEC (in the neutral case), respectively Cooper-pairing in the charged case (arguably a kind of pseudo-BEC). The connection between superfluidity and BEC was first made by Fritz London, who noted that T_λ was not too far off from the critical temperature one would predict by applying Eq. (1.1) to a noninteracting gas of helium atoms. Of course, liquid helium is anything **but** a noninteracting gas, so in that sense it is rather amusing that this connection was made. The modern conception of superfluidity is that it represents a collection of phenomena, most of them related to flow properties, and the initial observations of Kapitza can in fact be broken down into such "elementary" ingredients, as we shall see.

A great leap in the understanding of superfluidity was made with the help of Lev Landau's phenomenological *two-fluid model* [63]. In a nutshell, one can think of the problem in terms of two liquids, one formed by the condesate occupying the single-particle state ϕ_0 and flowing without friction, and the other behaving as a normal fluid. To be fair, it must be said that Landau actually opposed the whole notion of BEC, and formulated his model without it. We must also note that the superfluid and normal components in He-II are not the condensed and noncondensed atoms, as the whole liquid is superfluid at zero temperature, while only around 10% of the atoms are in the BEC state. That being said, the model describes He-II in thermodynamic equilibrium by introducing two independent velocities ($\boldsymbol{v}_s$ and $\boldsymbol{v}_n$), and associated densities (ρ_s and ρ_n), which are temperature-dependent. One can then express the total mass current density $\boldsymbol{J} = \boldsymbol{j}_s + \boldsymbol{j}_n$ and kinetic energy of flow $Q = Q_s + Q_n$ as [64]

$$\boldsymbol{J}(\boldsymbol{r}) = \rho_s(\boldsymbol{r})\boldsymbol{v}_s(\boldsymbol{r}) + \rho_n(\boldsymbol{r})\boldsymbol{v}_n(\boldsymbol{r}) \tag{1.46}$$

$$Q(\boldsymbol{r}) = \frac{\rho_s(\boldsymbol{r})\boldsymbol{v}_s^2(\boldsymbol{r})}{2} + \frac{\rho_n(\boldsymbol{r})\boldsymbol{v}_n^2(\boldsymbol{r})}{2} \tag{1.47}$$

with $\rho_s(\boldsymbol{r}) + \rho_n(\boldsymbol{r}) = \rho(\boldsymbol{r})$. We can futher define the superfluid (f_s) and normal (f_n) fractions as $f_s(T) = \rho_s(T)/\rho$ and $f_n(T) = \rho_n(T)/\rho$, with $f_s(T) + f_n(T) = 1$.

[12] In fact, formally one cannot even define viscosity in this case, as the ratio of the mass flow to the pressure differential diverges.

Furthermore, we have the limits

$$f_s(T) \xrightarrow[T\to 0]{} 1 \tag{1.48}$$

$$f_s(T) \xrightarrow[T\to T_\lambda]{} 0 \tag{1.49}$$

It is in this sense that one is dealing with an intuitive picture of He-II as a mixture of two independent, interpenetrating components, each associated with its own mass current and flow energy.

We now look at the N_0 atoms condensed in the state ϕ_0, in order to investigate the origin of the superfluid velocity $\boldsymbol{v}_s$. One can express the condesate wavefunction in the Madelung form[13]

$$\phi_0(\boldsymbol{r},t) = \sqrt{\frac{\rho_s(\boldsymbol{r},t)}{N_0(t)}} e^{\frac{i}{\hbar}\theta(\boldsymbol{r},t)} \tag{1.50}$$

with $\rho_s = N_0|\phi_0|^2$ being the particle density[14] and θ the phase (in dimensions of an action), both real functions. The quantum mechanical definition of the probability current density of the condensate yields (see Appendix 1.A)

$$\boldsymbol{j}_s(\boldsymbol{r},t) = N_0(t)\frac{\hbar}{2im}\left[\phi_0^\star(\boldsymbol{r},t)\boldsymbol{\nabla}\phi_0(\boldsymbol{r},t) - \phi_0(\boldsymbol{r},t)\boldsymbol{\nabla}\phi_0^\star(\boldsymbol{r},t)\right] \tag{1.51}$$

$$= N_0(t)|\phi_0(\boldsymbol{r},t)|^2\frac{1}{m}\boldsymbol{\nabla}\theta(\boldsymbol{r},t) \tag{1.52}$$

with m, as before, representing the particle mass. The ratio $\boldsymbol{v}_s \equiv \boldsymbol{j}_s/\rho_s$ will then be the condensate velocity (called *superfluid velocity* in the literature for the historical reasons detailed above)

$$\boldsymbol{v}_s(\boldsymbol{r},t) = \frac{1}{m}\boldsymbol{\nabla}\theta(\boldsymbol{r},t) \tag{1.53}$$

As the curl of a gradient is zero, the flow given by Eq. (1.53) is irrotational, in other words the vorticity

$$\boldsymbol{\nabla}\times\boldsymbol{v}_s(\boldsymbol{r},t) = 0 \tag{1.54}$$

provided, of course, that $\boldsymbol{v_s}$ is defined in all space (i.e. the magnitude of ϕ_0 is finite). If that is not the case, one can consider a contour C around the region where ϕ_0 vanishes, and the condition that ϕ_0 be single-valued then gives the famous *Onsager-Feynman quantization*

$$\oint_C \boldsymbol{v}_s(\boldsymbol{r},t)\cdot d\boldsymbol{l} = \frac{\hbar}{m}2\pi n_w \tag{1.55}$$

[13] We explicitly re-introduced $\hbar$ in the equations of this Section to show their quantum nature.

[14] We again emphasize that, in general, the superfluid density ρ_s is **not** equal to the density of condensed atoms.

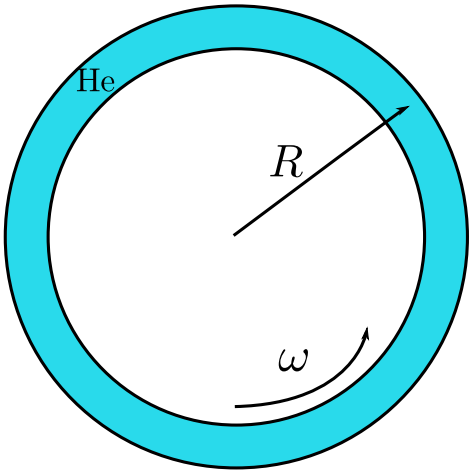

Figure 1.3: The multiply connected toroidal geometry, of radius R, used to showcase superfluid behaviour. The anullus, which contains ^{4}He atoms, rotates at an angular velocity ω.

with $n_w = 0, \pm 1, \pm 2, \ldots$ being the *windinding number*, the number of turns made by the phase in the complex plane, as we go around the integration contour C. Thus the circulation of the irrotational flow is quantized, with the quantum of circulation being $h/m = 0.997 \times 10^{-3}$ cm^2/s.

We are now in the position to discuss the two elementary ingredients which together account for the original obsevation of superfluidity by Kapitza. Following Ref. [27], we consider a multiply connected geometry in the form of a hollow cylindrical pipe with solid walls shown in Fig. 1.3. Assuming the pipe of radius R is filled with liquid helium, and rotates with angular velocity ω, one can then obtain the (temperature-dependent) orbital angular momentum of the system $L(T)$ by minimizing the effective free energy [64]

$$L(T) = I\left[f_n(T)\omega + f_s(T)n_w\omega_0\right] \tag{1.56}$$

Apart from the already defined quantities, we have introduced the moment of inertia $I = N_0 m R^2$, and defined the quantum unit of angular velocity, $\omega_0 \equiv \hbar/(mR^2)$. Finally, n_w is the nearest integer to ω/ω_0, expressed as

$$n_w = \text{int}\left[\frac{\omega}{\omega_0} + \frac{1}{2}\right] \tag{1.57}$$

One needs to compare Eq. (1.56) with the angular momentum of a normal liquid under the same circumstances, which is given by $L = I\omega = N_0\hbar\omega/\omega_0$. Keeping this in mind, we can now introduce the two qualitatively different experiments.

The first experiment starts by rotating the torus at a large angular velocity $\Omega \gg \omega_0$, on the high-temperature side of the λ-point. Once the fluid equilibrates with the motion of the container walls, we then cool the system through T_λ, maintaining the same angular velocity Ω. Finally, we stop the container from rotating, and measure the angular momentum. After a short while, proportional to the viscosity of the normal component, its velocity $\boldsymbol{v}_n$ becomes zero. However, the superfluid part of the liquid experiences no friction with the pipe walls, and will therefore continue circulating indefinately! Since we are not dealing with the ground state of the system, but with an excited state with astronomical lifetime, we call this phenomenon *metastability of supercurrents* ("persistent currents" is another commonly found term). However, metastability of superflow is not a direct consequence of the BEC state – the underlying mechanism is one of topological origin: consider the contour C in Eq. (1.55) to run around the torus of Fig. 1.3. The current in the ring will be proportional to the circulation Eq. (1.55). Since the latter is quantized, the windinding number n_w is conserved, hence so is the (super)current! Similar arguments explain the existence of so-called topological defects in superfluid systems. Such defects are singularities of the condensate wavefunction, for instance, vortex lines (or rings, if the line closes in on itself) associated with the superfluid component. The conservation laws presented above make the vortex a highly stable configuration, as opposed to the case of a normal fluid, where it is short-lived. In this sense, the circulating currents which constitute the vortex are "persistent", corresponding to metastable supercurrents. Furthermoe, a superfluid system cannot sustain bulk vorticity due to Eq. (1.54), and the vortices are quantized according to Eq. (1.55).

In the final state with the container at rest, $\omega = 0$, so the first term of Eq. (1.56) dissapears. The second term survives, as the system cannot change its winding number. In the limit of large n_w the angular momentum will then be approximately given by $L(T) \simeq f_s(T) I \Omega$. We see that one can reversibly increase (or decrease) the angular momentum L by varying the temperature (provided, of course, that it is always kept below T_λ). Since the superfluid circulates despite any roughness of the container walls, we can reasonably expect that an object moving though a stationary fluid also experiences reduced friction. This led to a series of experiments with charged ions being accelerated at various speeds by an applied external electric field [65, 66]. It was seen that, in accordance with the Landau criterion presented in Sec. 1.4, there exists a critical speed below which the ions experience reduced viscosity (and actually no viscosity at all in the $T = 0$ limit).

We now turn to the second experiment, which is arguably one of the fundamental defining properties of superfluidity. The effect was first predicted by Fritz London and then observed by G. Hess and W. Fairbank in 1967 in the context of liquid helium, hence the name Hess-Fairbank (HF) effect. As before, we cool the sample while rotating with a lower angular velocity $\omega \ll \Omega$. We wait for the system to equilibrate, and then measure the angular momentum, this time without stopping the rotation of the container. The value of L will be given by

Eq. (1.56), instead of the classical $I\omega$ (that is why the HF effect is also called nonclassical rotational inertia, NCRI). We can now distinguish two different regimes. The first one, for $\omega < \frac{1}{2}\omega_0$, implies $n_w = 0$, therefore $L(T) = f_n(T)I\omega$, so the superfluid component contributes nothing to the current. At $T = 0$, $f_n(T) \to 0$ and we get the spectacular result that the liquid completely ceases to rotate along with the container! In the general case, the second term of Eq. (1.56) survives. If we again consider the zero-temperature limit, and plot the angular momentum $L(0) = I\omega_0 n_w$ versus angular velocity $\omega \geq \frac{1}{2}\omega_0$, we get a series of plateaus of width ω_0 at positions $L = N_0\hbar n_w = N_0\hbar, 2N_0\hbar$, and so on. The centers of these plateaus all fall on the "classical" line $L = N_0\hbar\omega/\omega_0$. A hand-waving explanation, for the simplest case of a noninteracting atomic gas, goes as follows. In a noncondensed system rotating with angular velocity ω, the effective single-particle energies are shifted by an amount $\hbar\omega\ell_{n_w}$, with ℓ_{n_w} the angular momentum quantum number of state n_w. The Bose-Einstein function then redistributes the particles to accomodate this shift, producing a "classical" angular momentum. In a BEC however, all N_0 atoms must be in the same state n_w, and posess the same value of ℓ_{n_w}. Their only allowed contribution to L is then $N_0(n_w\hbar)$. For small ω, the condensate is in the $n_w = 0$ state, and so it does not rotate with the container! This argument can be formalized, so one can show the HF effect to be impossible inside the framework of classical statistical mechanics, much like the Bohr-Van Leeuwen theorem shows magnetism to be a purely quantum phenomenon. Note that, while the HF effect can be (at least hand-wavingly) explained without including interactions, these are crucial to any theory of metastable currents.

As already explained in the introductory paragraph of this Section, there is a deep underlying connection between superfluidity in a neutral system and superconductivity in a charged one. In fact, the analog of the HF effect in a charged system is the well-known Meissner effect. We now consider the same topology of Fig. 1.3, and replace the container by a crystal lattice and the liquid helium (or atomic gas for that matter) by the electrons inside this lattice. If we now keep the crystal at rest and produce a tangential vector potential $\boldsymbol{A}(\boldsymbol{r}) = A\hat{\phi}$, this will generate a flux $\Phi = \oint \boldsymbol{A}(\boldsymbol{r}) \cdot d\boldsymbol{l}$ inside the conducting ring (usually called an "Aharonov-Bohm" flux). The definition of the "superfluid" velocity Eq. (1.53) now needs to be revised according to the gauge-coupling recipe, which consists of replacing the canonical momentum $\boldsymbol{p}$ by the kinematic one: $\boldsymbol{p} \to \boldsymbol{p} - e\boldsymbol{A}(\boldsymbol{r})$. As a result, we get

$$\boldsymbol{v}_s(\boldsymbol{r}) = \frac{1}{2m}\left(\boldsymbol{\nabla}\theta(\boldsymbol{r}) - 2e\boldsymbol{A}(\boldsymbol{r})\right) \tag{1.58}$$

where the factors of 2 appear because the macroscopic wavefunction is now that of the center of mass of a Cooper-pair of electrons, so m and e are both multiplied by 2. The resulting Onsager-Feynman quantization Eq. (1.55) then becomes

$$\oint_C \boldsymbol{v}_s(\boldsymbol{r}) \cdot d\boldsymbol{l} = \frac{\hbar}{2m}\left(2\pi n_w - \frac{\Phi}{\Phi_0}\right) \tag{1.59}$$

where $\Phi_0 \equiv h/(2e)$ is the *superconducting flux quantum*. If the (mass) supercurrent is given, as before, by $\boldsymbol{j}_s = \rho_s \boldsymbol{v}_s$, then this new quantization condition results in a non-zero current even for $n_w = 0$. Indeed, for $\Phi < \frac{1}{2}\Phi_0$ (compare to the regime $\omega < \frac{1}{2}\omega_0$ discussed for the HF effect), the $n_w = 0$ state is realized and the electrical current $\boldsymbol{j}_e$ is given by

$$\boldsymbol{j}_e(\boldsymbol{r}) = \frac{2e}{2m}\boldsymbol{j}_s = -\frac{e^2}{m^2}\rho_s(T)\boldsymbol{A}(\boldsymbol{r}) \tag{1.60}$$

This proves that, while in a normal conductor the flux Φ would not generate any circulating current, a superconducting ring would respond with a diamagnetic (note the minus sign in Eq. (1.60)) electrical current proportional[15] to the vector potential $\boldsymbol{A}$. Coupling this with Maxwell's equations immediately results in the well-known Meissner effect, namely the expulsion of an applied magnetic field inside a superconducting sample.

We now proceed to a closer analysis of the connection between the charged and neutral case. The Hamiltonian H for a particle of charge q and mass m, moving in a vector potential $\boldsymbol{A}$, and in the presence of an external potential V, is given by Eq. (1.61). In our problem, V is imposed by the toroidal geometry of the container, which is for now assumed to be stationary in the inertial frame of the stars. On the other hand, the Hamiltonian H', of a neutral particle with the same mass, but this time in the frame that rotates with the container at an angular velocity $\boldsymbol{\omega} = \omega\hat{z}$ is shown in Eq. (1.62),

$$H = \frac{1}{2m}(\boldsymbol{p} - q\boldsymbol{A}(\boldsymbol{r}))^2 + V(\boldsymbol{r}) \tag{1.61}$$

$$H' = \frac{1}{2m}(\boldsymbol{p}' - m\boldsymbol{\omega}\times\boldsymbol{r}')^2 + V(\boldsymbol{r}') - \frac{1}{2}m(\boldsymbol{\omega}\times\boldsymbol{r}')^2 \tag{1.62}$$

with $\boldsymbol{r}'$ being the coordinate (and $\boldsymbol{p}'$ the canonical momentum) in the rotating frame. Making use of the cylindrical symmetry, one can decompose $\boldsymbol{r}$ as $(r,\, z,\, \theta)$, and therefore $\boldsymbol{r}' = (r,\, z,\, \theta - \omega t)$. We now see that a neutral system in the rotating frame, apart from a centrifugal term $-\frac{1}{2}m(\boldsymbol{\omega}\times\boldsymbol{r}')^2$, is formally identical to a charged system in the rest frame, with the correspondence $q\boldsymbol{A}(\boldsymbol{r}) \leftrightarrow m\boldsymbol{\omega}\times\boldsymbol{r}$. This connection can be used to make a neutral particle experience an "effective" electromagnetic vector potential. Its gauge-coupling to this potential is what eventually led to the celebrated concept of *synthetic gauge field*. In fact, such artificial, rotation-induced, gauge fields have already been proposed in the context of ultracold atomic gases, in order to asess their normal and superfluid fractions [67–69].

This naturally leads us to the topic of experimental evidence for superfluid behaviour. The answer, however, will not be a clear-cut one, as we have seen that it actually depends on which aspects of superfluidity one is interested in,

[15] The proportionality constant is called the susceptibility.

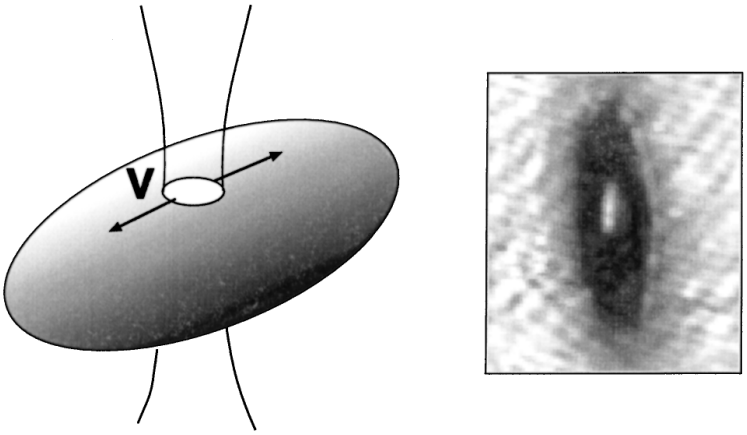

Figure 1.4: Scanning a blue-detuned laser beam with velocity v, though the cigar-shaped atomic condensate (left panel), creates a density hole (right panel) larger than the healing length. The friction acting on this hole can then be used to asess the Landau critical velocity. From Ref. [70].

such as NCRI, persistent currents, quantized vortices or reduced friction on impurities. Historically, liquid ^{4}He-II was the default system for exploring such physics, however, new systems such as ultracold gases and, more recently, microcavity polaritons (the subject of Chapter 2) have also entered the picture. In the case of liquid helium, superfluidity is relatively easy to detect, while BEC can only be asessed through circumstantial evidence (such as neutron scattering), as strong interactions oppose any large density changes. Ultracold gases, on the other hand, present a spectacular BEC onset that can be observed in the density profile, while superfluidity proves somewhat more mysterious. Regarding metastable supercurrents in a simply connected geometry, Chevy and coworkers [71] succeded in stirring an atomic condensate, and then measuring its angular momentum using the precession of certain collective modes. Other studies were also shown to produce a metastable single-vortex state (and even vortex lattices) that persist, despite not being the ground state of the system (in fact, it can be shown that the atomic BEC ground state is characterised by the absence of any macroscopic current flow). Interferometric measurements are commonly employed to see the circulation around these vortex cores. However, the lifetime of the vortices is limited by how long it takes before they escape the magnetic trap. To circumvent this limitation, persistent currents in multiply connected geometries (such as toroidal traps) were also investigated, for instance in Refs. [72] and [73]. As far as the Landau criterion is concerned, an experiment similar to the one accelerating charged ions through liquid helium was reported in Ref. [74]. The authors used a Raman laser to transfer a fraction of the condensed atoms

into a different (hyperfine) state. As a result, those atoms no longer experienced any magnetic trapping, but only the effect of gravity. The mobility of the free-falling atoms was then computed, revealing information about the friction [59] acting on them. A fairly sharp transition with a sudden increase in friction was observed, at velocities close to the local speed of sound. In the opposite limit of macroscopic "impurities" (large compared to the healing length), Ref. [75] details the use of a blue-detuned laser beam, in order to create a density hole which is then moved around the atomic condensate (see Fig. 1.4). By measuring the density difference immediately ahead and behind the hole, one can deduce the frictional force acting on it (see Appendix 1.A). This experiment resulted in a critical velocity about ten times smaller than the speed of sound, presumably due to vortex creation by the macroscopic defect.

1.6 Optical lattices

An electric dipole moment $\boldsymbol{\mathcal{P}}$ placed in an external electric field $\boldsymbol{\mathcal{E}}(\boldsymbol{r})$ aquires an energy $\mathcal{V}(\boldsymbol{r}) = -\boldsymbol{\mathcal{P}} \cdot \boldsymbol{\mathcal{E}}(\boldsymbol{r})$. If an atom is placed in a light field, the oscillating electric field of the latter induces an electric dipole moment $\boldsymbol{\mathcal{P}} = \alpha\epsilon_0\boldsymbol{\mathcal{E}}$ on the atom, with ϵ_0 the free-space permittivity and α the atomic polarizability [76]. Integrating, we obtain the interaction energy of the atom with the field as $\mathcal{V}(\boldsymbol{r}) = -\frac{1}{2}\alpha\epsilon_0\mathcal{E}^2(\boldsymbol{r})$. A classical model of the atom as a conducting sphere of radius r yields a polarizability of $4\pi r^3$. In practice however, atomic transitions complicate this simple picture, as the polarizability α depends on the driving frequency of the light field. In the framework of the Drude model [77], one has

$$\alpha(\omega) = \frac{\alpha(0)\omega_0^2}{\omega_0^2 - \omega^2 - i\frac{\omega}{\tau}} \tag{1.63}$$

with the resonant frequency ω_0, damping time τ and $\alpha(0) > 0$ the static polarizability. The frequency-dependent interaction energy $\mathcal{V}(\omega)$ thus obtained is sometimes called the *ac Stark effect* [78]. If the light frequency is smaller than that of the atomic resonance $\omega < \omega_0$, the induced dipole is in phase with the electric field, as $\Re[\alpha(\omega)] > 0$, and the force on the atom will point in the direction of the square-field maxima (the situation is of course reversed if instead $\omega > \omega_0$). This effect was first used in Ref. [79] to trap a BEC of sodium atoms using a focused infrared laser beam (the dominant transition of Na is the familiar $s \to p$ yellow emission). Interestingly, the same physics can be used to create an optical lattice, as explained below.

Consider a (plane wave) laser beam propagating along the x axis, with an associated electric field $\boldsymbol{\mathcal{E}}(x,t) = \boldsymbol{\mathcal{E}}_0\cos(k_x x - \omega t)$, which reflects from a mirror situated at $x = 0$. The interference between the reflected and original beam produces a standing wave $\boldsymbol{\mathcal{E}}_0[\cos(k_x x - \omega t) - \cos(k_x x + \omega t)]$, with an intensity $|\mathcal{E}(x,t)|^2 = 4|\mathcal{E}_0|^2\sin^2(k_x x)\sin^2(\omega t)$. This results in an effective periodic lattice

for the atoms, with lattice spacing $b = \lambda_x/2$, where $\lambda_x = 2\pi/k_x$. Such a one-dimensional lattice was first demonstrated in Ref. [80]. By tuning the strength of the laser field, one can adjust the lattice depth, and by changing the laser wavelength, one can modify the lattice constant. Adding more laser beams can produce two- or even three-dimensional lattices, in a variety of different geometries. For example, the simplest way to create a 2D square lattice would be to superimpose a second lattice in the $\hat{\boldsymbol{y}}$ direction, producing an optical potential of depth V_0:

$$\mathcal{V}(x, y) = V_0[\sin^2(\pi x/b) + \sin^2(\pi y/b)] \tag{1.64}$$

The beam along y should be orthogonally polarized with respect to the one along x, in order to avoid interference effects.

The eigen-problem of a particle moving in a periodic potential given by Eq. (1.64) is well-known in the context of solid-state band theory [77], as the electrons inside a solid also move in such a potential, produced in that case by the crystal ions. The energy eigenstates are the Bloch waves $\psi_{\gamma,\boldsymbol{k}}(\boldsymbol{r}) = e^{i\boldsymbol{k}\cdot\boldsymbol{r}} u_{\gamma,\boldsymbol{k}}(\boldsymbol{r})$, where $\hbar\boldsymbol{k}$ is the *quasimomentum*, restricted to the first Brillouin zone (BZ) $\left(-\frac{\pi}{b}, \frac{\pi}{b}\right) \times \left(-\frac{\pi}{b}, \frac{\pi}{b}\right)$ and $\gamma = 0, 1, \ldots$ represents the *band index*. The functions $u_{\gamma,\boldsymbol{k}}(\boldsymbol{r})$ are periodic in both the $\hat{\boldsymbol{x}}$ and $\hat{\boldsymbol{y}}$ direction, with period b. To see how these bands arise, one can expand both the wavefunction $\psi_{\gamma,\boldsymbol{k}}$ as well as the potential $\mathcal{V}$ in a Fourier series, making use of their periodicity. Inserting this expansion into the time-independent Schrödinger equation, we get a linear system of equations for the Fourier coefficients. For fixed $\boldsymbol{k}$, we obtain different[16] eigenenergies, $E_\gamma(\boldsymbol{k})$. These eigenenergies form bands (called Bloch bands) when $\boldsymbol{k}$ is varied inside the BZ. Each band as a certain width in energy (unsurprisingly called the bandwidth) and consecutive bands are separated by gaps, meaning certain energies are not allowed. Furthermore, each eigenenergy has an associated eigenfunction, completely determined by the set of Fourier coefficients with index γ. The solution of course depends on the value of V_0, and we can distinguish two limiting cases, depending on the ratio of the bandwidths to the energy gaps. In the weak-potential limit, the bandgaps are much smaller than the bandwidths, and the eigenenergies have a pronounced dependence on quasimomentum. The opposite limit, which is the one we want to focus on, is the regime of deep lattices, also called the *tight-binding* (TB) limit. The band dispersion is now flatter compared to the previous case, and the bandwidth/gap ratio is much smaller.

For low temperatures in the TB limit, only the lowest energy band $\gamma = 0$ is occupied, so we subsequently drop the band index. Since the potential wells are so deep, the lowest band is adequately described by considering localized wavefunctions at each well, i.e. at the minima of Eq. (1.64). Suppose now that a function $w(\boldsymbol{r})$ exists such that the Bloch waves are given by

$$\psi_{\boldsymbol{k}}(\boldsymbol{r}) = \mathcal{N} \sum_{m,n} e^{i\boldsymbol{k}\cdot\boldsymbol{r}_{m,n}} w(\boldsymbol{r} - \boldsymbol{r}_{m,n}) \tag{1.65}$$

[16] Truncating the Fourier expansion to a finite number of terms n results in $2n + 1$ bands.

where $\mathcal{N}$ is a normalization factor and $\boldsymbol{r}_{m,n} = mb\hat{\boldsymbol{x}} + nb\hat{\boldsymbol{y}}$ are the well positions. Eq. (1.65) represents a wave, $e^{i\boldsymbol{k}\cdot\boldsymbol{r}_{m,n}}$, whose phase and amplitude at each well is given by the localized function w, called the *Wannier function* [77]. It can be shown that Wannier functions centered at different wells are orthogonal to each other and form a complete basis. The Wannier functions are thus a unitary transformation of the Bloch functions, suitable for the case when particle dynamics is described by inter-well tunneling (hopping) between nearest-neighbour wells.

In the case of a BEC, when the number of ultracold atoms per lattice well is small, the "discrete structure" of the condensate becomes relevant and we must replace the GP description Eq. (1.7) we have used so far with a lattice model, such as the Bose-Hubbard model [81], as suggested in Ref. [82]. For a condensate confined in the optical potential Eq. (1.64), with an additional harmonic trap $U(\boldsymbol{r})$, the spinless Bose-Hubbard Hamiltonian in 2D can be written as [83]

$$\mathcal{H}_{\mathrm{BH}} = \mathcal{H}_0 + \frac{U}{2}\sum_{m,n}\hat{n}_{m,n}(\hat{n}_{m,n}-1) + \sum_{m,n}\epsilon_{m,n}\hat{n}_{m,n} \tag{1.66}$$

where $U \propto g$ is the on-site interaction strength and $\epsilon_{m,n} \propto U(\boldsymbol{r}_{m,n})$ is the energy offset due to the harmonic trap. Futhermore, $\hat{n}_{m,n} = \hat{a}^\dagger_{m,n}\hat{a}_{m,n}$ denotes the number operator for site (m,n) and $\hat{a}^\dagger_{m,n}$ ($\hat{a}_{m,n}$) is the bosonic creation (destruction) operator for that site. Finally, the kinetic part

$$\mathcal{H}_0 = -J\sum_{m,n}\left(\hat{a}^\dagger_{m+1,n}\hat{a}_{m,n} + \hat{a}^\dagger_{m,n+1}\hat{a}_{m,n}\right) + \mathrm{H.c.} \tag{1.67}$$

can be diagonalized to yield the Bloch dispersion

$$E(\boldsymbol{k}) = -2J\left[\cos(k_x b) + \cos(k_y b)\right] \tag{1.68}$$

where the tunneling amplitude J is an exponentially decreasing function of V_0 [83]. The characteristic tunneling energy scale is given by the bandwidth, which in this case is $8J$.

Hamiltonian Eq. (1.66) supports a zero-temperature quantum phase transition between a superfluid and a Mott-insulating phase, at a critical value of the ratio U/J. This transition was experimentally observed for the case of a bosonic BEC in a 3D optical lattice, as reported in Ref. [84]. Increasing the lattice depth V_0, the authors went from a gapless, superfluid regime dominated by the kinetic term Eq. (1.67) to a gapped Mott-insulator state, where the atoms are localized and the on-site interaction term in Eq. (1.66) is dominant.

1.7 Harper-Hofstadter model

In Sec. 1.6 we introduced the quantized Bloch bands, characterising particles in a periodic potential. A similar quantization also occurs in the case of a charged

particle moving perpendicular to a constant uniform magnetic field, and the allowed energy bands are called *Landau levels* [85]. In a magnetic field $\boldsymbol{B} = B\hat{\boldsymbol{z}}$, the relevant energy and length scales for a particle with charge e and mass m are set by the *cyclotron frequency* $\omega_c = eB/m$ and *magnetic length* $l_\mathrm{m} = \sqrt{\hbar/eB}$, respectively. In this Section we want to explore the fate of the Bloch bands in presence of a magnetic field. Alternatively, one could also start from a Landau quantized system and perturb it via a weak periodic potential [86, 87], the two approaches having distinct validity ranges.

One of the simplest TB models for Bloch electrons in uniform magnetic fields is the *Harper-Hofstadter model* [88, 89]. Its relevant dimensionless parameter is the ratio of flux Φ through a lattice cell to one *Dirac flux quantum*[17] $\Phi_0 = h/e$

$$\alpha = \frac{\Phi}{\Phi_0} = \frac{eBb^2}{h} \tag{1.69}$$

Physically, α reflects[18] the commensurability of the lattice period b and the magnetic length l_m, as it can be recast in the form $\alpha = \frac{1}{2\pi}\left(b/l_\mathrm{m}\right)^2$. The resulting single-particle energy spectrum of the model depends on the rationality of α. If $\alpha = p/q$, for p and q co-prime integers, the Bloch band splits into q distinct magnetic subbands. For α irrational, the spectrum consists instead of an infinite number of energy levels, forming a Cantor set. The union of all allowed energies as a function of α forms a self-similar fractal, shown in Fig. 1.5 and known as *Hofstadter's butterfly* [89]. In the continuum limit ($b \to 0$, with fixed B), $\alpha \ll 1$ and the bands group into clusters that can be identified with the Landau fan predicted in the absence of a lattice potential.

Solid-state experiments in the Hofstadter regime are notoriously difficult, since the inter-atomic spacing of a crystal lattice is a few Ångströms, and achieving a comparable magnetic length would require a field of about 10^4 Tesla. Signatures of the Hofstadter bands have instead been seen in artificial superlattices with periodicities of tens of nanometers [90, 91]. In the context of neutral ultracold atoms, synthetic gauge potentials paved the way for the exploration of similar physics [39, 40]. For instance, rotating a harmonically trapped condensate with a high angular velocity (comparable to the radial trap frequency) allowed BEC experiments [92] to enter the lowest Landau level (LLL) regime. Rotating 2D optical lattices have also been realized [93], but the first implementation of the Harper-Hofstadter (HH) model with ultracold atoms [94, 95] employed a different method [40] of generating the artificial magnetic field, namely *laser-assisted tunneling* [96] based on a linear superlattice potential [97]. In a nutshell, tunneling between lattice sites required atoms to absorb and emit photons produced by external lasers. The interaction with said lasers generated a net phase change equivalent to the flux of a magnetic field. The total phase accumulated by an atom when performing a loop around a lattice cell (plaquette) was $\sim \pi/2$ in these experiments.

[17] As opposed to the superconducting flux quantum of Sec. 1.5.

[18] Not to be confused with the atomic polarizability, also denoted by α.

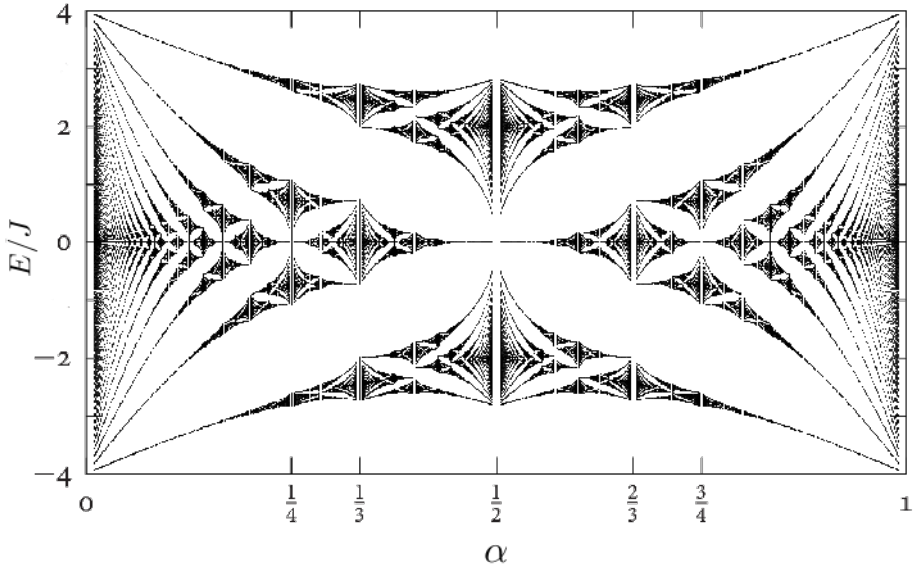

Figure 1.5: Hofstadter's butterfly, representing the internal structure of the lowest Bloch band in a uniform magnetic field. For rational values of $\alpha = p/q$, the spectrum has q magnetic subbands, which become increasingly narrow as q gets larger. Adapted from Ref. [89].

In quantum mechanics, the phase of the wavefunction of a charged particle moving between positions $\boldsymbol{r}_1$ and $\boldsymbol{r}_2$ is changed by the presence of a magnetic field $\boldsymbol{B} = \boldsymbol{\nabla} \times \boldsymbol{A}$ by [76]

$$\phi_{12} = \frac{e}{\hbar} \int_{\boldsymbol{r}_1}^{\boldsymbol{r}_2} d\boldsymbol{r} \cdot \boldsymbol{A}(\boldsymbol{r}) \tag{1.70}$$

where the integral is taken along an oriented path from point "1" to point "2". Therefore, $\phi_{21} = -\phi_{12}$ and, if we consider a smooth closed integration contour $\mathcal{C}$ instead of two separate points, the total phase change (or *Aharonov-Bohm phase*) along $\mathcal{C}$ is

$$\phi_{\mathcal{C}} = \frac{e}{\hbar} \int_{\mathcal{S}} d^2\boldsymbol{r} \cdot \boldsymbol{\nabla} \times \boldsymbol{A}(\boldsymbol{r}) = 2\pi \frac{\Phi_B}{\Phi_0} \tag{1.71}$$

where Φ_B is the magnetic flux through a smooth surface $\mathcal{S}$ bounded by the curve $\mathcal{C}$ with positive orientation, according to Stoke's theorem.

On the 2D square lattice in Fig. 1.6, one can define the magnetic phases $\phi_{m,n} = \left(\phi^x_{m,n}, \phi^y_{m,n}\right)$ along the $\hat{\boldsymbol{x}}$ and $\hat{\boldsymbol{y}}$ directions in a similar manner, as

$$\phi^x_{m,n} = \frac{e}{\hbar} \int_{\boldsymbol{r}_{m,n}}^{\boldsymbol{r}_{m+1,n}} d\boldsymbol{r} \cdot \boldsymbol{A}(\boldsymbol{r}) \qquad \phi^y_{m,n} = \frac{e}{\hbar} \int_{\boldsymbol{r}_{m,n}}^{\boldsymbol{r}_{m,n+1}} d\boldsymbol{r} \cdot \boldsymbol{A}(\boldsymbol{r}) \tag{1.72}$$

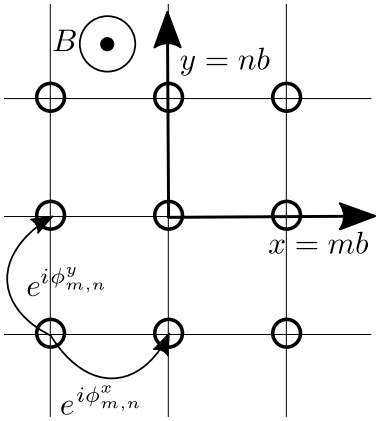

Figure 1.6: 2D square lattice pierced by a homogeneous static magnetic field $\boldsymbol{B} = B\hat{\boldsymbol{z}}$. The lattice constant is b, and the curved arrows indicate the field-induced hopping phases.

where the integrals are now taken along the links joining neighbouring sites. Using Eq. (1.71), the flux Φ through a plaquette can be related to the total phase $\phi_\square$ accumulated on a contour enclosing the plaquette in a counterclockwise sense

$$\phi_\square \equiv \sum_{\circlearrowleft\square} \phi_{m,n} = \phi^x_{m,n} + \phi^y_{m+1,n} - \phi^x_{m,n+1} - \phi^y_{m,n} = 2\pi\alpha \tag{1.73}$$

Note that $\phi_\square$ is gauge-independent, unlike the *Peierls phases* $\phi_{m,n}$.

To obtain the HH Hamiltonian, we introduce a static uniform magnetic field into the single-band Bose-Hubbard model Eq. (1.66) of Sec. 1.6. We follow Hofstadter's original treatment, and neglect on-site interactions[19], as well as the harmonic trapping. The kinetic term Eq. (1.67) is then modified according to Peierls' substitution [99] to include the hopping phases $\phi_{m,n}$

$$\mathcal{H}_0 = -J \sum_{m,n} \left(e^{i\phi^x_{m,n}} \hat{a}^\dagger_{m+1,n} \hat{a}_{m,n} + e^{i\phi^y_{m,n}} \hat{a}^\dagger_{m,n+1} \hat{a}_{m,n} \right) + \text{H.c.} \tag{1.74}$$

These phases act to "frustrate" the hopping, such that for noninteger α it is impossible to minimize the kinetic energy simultaneously on all lattice links [100]. The Hamiltonian is no longer invariant under translations by a single lattice site in any direction, because fixing a gauge for the vector potential $\boldsymbol{A}(\boldsymbol{r})$ reduces the physical symmetry of the lattice. In fact, it can be shown [101] that a translation of $\boldsymbol{A}$ is equivalent to a gauge transformation, suggesting that new translation operators that would commute with Eq. (1.74) can be constructed as a combination of translation and gauge transformation.

[19] For a treatment that includes interactions in the Bogoliubov approximation, see Ref. [98].

We define the *magnetic translation operators* (MTOs) [102, 103] as

$$\hat{T}_x = \sum_{m,n} \hat{a}^\dagger_{m+1,n} \hat{a}_{m,n} e^{i\theta^x_{m,n}} \qquad \hat{T}_y = \sum_{m,n} \hat{a}^\dagger_{m,n+1} \hat{a}_{m,n} e^{i\theta^y_{m,n}} \tag{1.75}$$

where the phases $\theta_{m,n}$ are to be determined by imposing $\left[\hat{T}, \mathcal{H}_0\right] = 0$, leading to [104]

$$\theta^x_{m,n} = \phi^x_{m,n} + 2\pi\alpha n \qquad \theta^y_{m,n} = \phi^y_{m,n} - 2\pi\alpha m \tag{1.76}$$

While the specific form of the MTOs depends on the choice of gauge, their commutator is gauge independent

$$\hat{T}_x \hat{T}_y = \hat{T}_y \hat{T}_x e^{i2\pi\alpha} \tag{1.77}$$

and vanishes only if α is an integer, a situation equivalent to the zero-field case. In order to proceed, we point out that Eq. (1.77) has a transparent physical interpretation. If we act on the single-particle state $|m,n\rangle = \hat{a}^\dagger_{m,n}|0\rangle$

$$\hat{T}^\dagger_y \hat{T}^\dagger_x \hat{T}_y \hat{T}_x |m,n\rangle = e^{-i2\pi\alpha} |m,n\rangle \tag{1.78}$$

we see that performing a counterclockwise loop around a unit cell results in the accumulation of a phase proportional to the flux inside the cell. This can be generalized to a macrocell containing $r \times s$ original lattice cells, to deduce that

$$\hat{T}^r_x \hat{T}^s_y = \hat{T}^s_y \hat{T}^r_x e^{i(rs)2\pi\alpha} \tag{1.79}$$

For $\alpha = p/q$ the commutator $\left[\hat{T}^r_x, \hat{T}^s_y\right]$ vanishes if $p(rs)/q$ is an integer. The smallest possible macrocell is given by $rs = q$ and is called the *magnetic unit cell*. For this choice of unit cell, $\{\hat{T}^r_x, \hat{T}^s_y, \mathcal{H}_0\}$ form a complete set of commuting operators, so we can find simultaneous eigenstates, labeled by the quasi-momentum $\hbar\boldsymbol{k}^0$ which is now restricted to the *magnetic Brillouin zone* (MBZ) $\left(-\frac{\pi}{rb}, \frac{\pi}{rb}\right) \times \left(-\frac{\pi}{sb}, \frac{\pi}{sb}\right)$.

To obtain the spectrum of $\mathcal{H}_0$, we need to solve its associated Schrödinger equation, $\mathcal{H}_0|\psi\rangle = E|\psi\rangle$. We expand the eigenstates $|\psi\rangle$ in the single-particle basis $|\psi\rangle = \sum_{m,n} \psi_{m,n}|m,n\rangle$ and obtain an equation for the coefficients $\psi_{m,n}$

$$\begin{aligned} -J\big(&e^{-i\phi^x_{m,n}}\psi_{m+1,n} + e^{i\phi^x_{m-1,n}}\psi_{m-1,n} \\ &+ e^{-i\phi^y_{m,n}}\psi_{m,n+1} + e^{i\phi^y_{m,n-1}}\psi_{m,n-1}\big) = E\psi_{m,n} \end{aligned} \tag{1.80}$$

We fix the Landau gauge $\boldsymbol{A}(x,y) = Bx\hat{\boldsymbol{y}}$ for simplicity, so $\phi_{m,n} = (0, 2\pi\alpha m)$ and we choose the magnetic unit cell[20] $r \times s = q \times 1$, for which the commuting MTOs

[20] In the symmetric gauge, the magnetic unit cell is larger, containing $2q \times 2q$ sites.

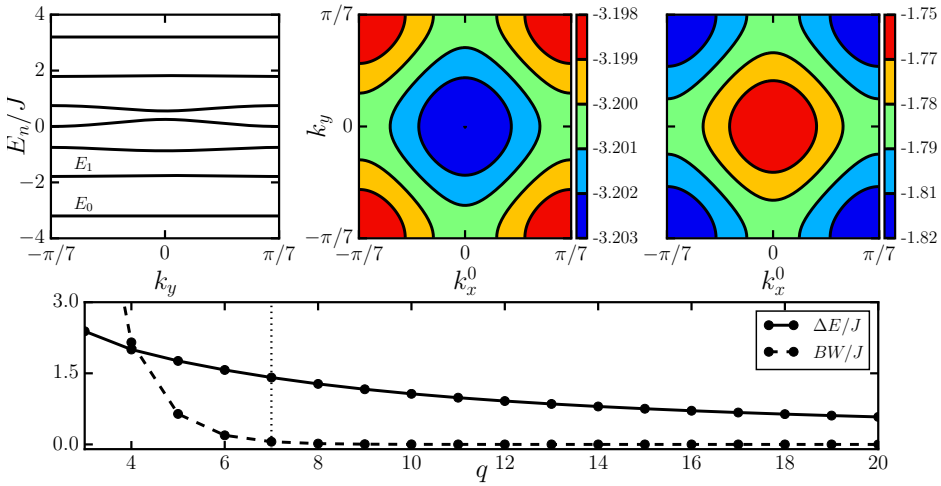

Figure 1.7: *Top panels:* Single-particle energy spectrum (left) $E_n(k_x^0 = 0, k_y)$ of the HH Hamiltonian Eq. (1.74) for $\alpha = 1/7$ and dispersion of the two lowest bands, $E_0(\boldsymbol{k})$ (middle) and $E_1(\boldsymbol{k})$ (right) in (part of) the MBZ. *Bottom panel:* Energy gap (continuous line) $\Delta E = \langle E_1(\mathbf{k})\rangle_{\mathbf{k}} - \langle E_0(\mathbf{k})\rangle_{\mathbf{k}}$ (here $\langle\cdot\rangle_{\mathbf{k}}$ denotes an average over the MBZ) and bandwidth of $E_0(\boldsymbol{k})$ (dashed line, $\times 10$) for $p = 1$. The dotted vertical line marks the location of the $q = 7$ case shown above.

read

$$\hat{T}_x^q = \sum_{m,n} \hat{a}^\dagger_{m+q,n}\hat{a}_{m,n} \qquad \hat{T}_y = \sum_{m,n} \hat{a}^\dagger_{m,n+1}\hat{a}_{m,n} \tag{1.81}$$

justifying the plane wave ansatz[21] $\psi_{m,n} = e^{ik_y nb}e^{ik_x^0 mb}\psi_m$ subject to the periodic boundary conditions $\psi_{m+q} = \psi_m$. Substituting this ansatz into Eq. (1.80) yields the *Harper equation* [105]

$$-J\left[e^{-ik_x^0 b}\psi_{m-1} + 2\cos\left(k_y b - 2\pi\alpha m\right)\psi_m + e^{ik_x^0 b}\psi_{m+1}\right] = E\psi_m \tag{1.82}$$

Calculating the single-particle spectrum of Eq. (1.74) is therefore equivalent to solving the eigenvalue equation $\sum_{m'=0}^{q-1} H_{mm'}\psi_{m'} = E\psi_m$, $m = 0, \ldots, q-1$ for the $q \times q$ matrix H defined as[22]

$$H_{mm'}(k_x^0, k_y) = -J \times \begin{cases} e^{-ik_x^0 b} & \text{if } m' = m-1 \bmod q \\ 2\cos\left(k_y b - 2\pi\alpha m\right) & \text{if } m' = m \\ e^{ik_x^0 b} & \text{if } m' = m+1 \bmod q \\ 0 & \text{otherwise} \end{cases} \tag{1.83}$$

[21] Here k_y is defined in the full BZ.
[22] If $q = 2$, $m + 1 \bmod q = m - 1 \bmod q$ and $H_{01} = H_{10} = -2J\cos(k_x^0 b)$.

For integer α we recover the lowest Bloch band Eq. (1.68), while for $\alpha = p/q$ this band splits into q bands with dispersion $E_n(k_x^0, k_y)$, $n = 0, \ldots, q-1$.

In the top-left panel of Fig. 1.7 we show an example of the spectrum computed by diagonalizing H for $\alpha = 1/7$. The $E = 0$ level is at the centre of the middle band, and there are $q-1$ gaps separating the bands. For even values of q, the spectrum is symmetric with respect to $E = 0$ and the two central bands touch at zero energy. Around these degeneracy points, the dispersion is linear [106], while in all other cases it is quadratic near its minimum. The $\alpha = 1/2$ case is particularly interesting by analogy to graphene-related physics [107], as there are two inequivalent "Dirac points" and the Hamiltonian preserves time-reversal symmetry. Inspecting the middle and right panels we note that, despite the reduced symmetry of $\mathcal{H}_0$, the dispersion has the full C_4 rotational symmetry of the underlying square lattice. One can formally define rotation and reflection operators which, together with the MTOs, constitute the full *projective symmetry group* [108]. The bottom panel of Fig. 1.7 shows the evolution of the lowest energy gap ΔE, as well as the bandwidth BW of the lowest band as function of q (for the case $\alpha = 1/q$). The lowest band gets flatter, as the continuum ($q \to \infty$) LLL eigenstates are the solutions of the lowest band of the HH model [104], and ΔE decreases like $\sim 1/q$, as the number of gaps is $\sim q-1$ (excluding the band bottom and band top).

The energy bands of the HH model are topologically nontrivial, as characterized by their non-zero *Chern numbers* – topological invariants that are linked to the quantization of the Hall conductivity in the integer quantum Hall (QH) effect [109]. In fact, solutions of the Harper equation Eq. (1.82) were also studied in connection with the QH effect [106]. We make use of these topological properties in Chapter 5, where we consider the HH model in the presence of an external harmonic trap in a dissipative system.

1.A Conservation laws for the GP field

In this Appendix we use (classical) field theory to derive the conservation laws associated with the time-dependent Gross-Pitaevskii Eq. (1.7). We start by recasting the TDGP using Einstein's summation convention, with the notation $\boldsymbol{x} \equiv (x_1, x_2, x_3)$ and $\partial_k \equiv \frac{\partial}{\partial x_k}$ $(k = 1, 2, 3)$

$$i\hbar\partial_t\phi_0(\boldsymbol{x},t) = \left[-\frac{\hbar^2}{2m}\partial_k\partial_k + U(\boldsymbol{x},t) + gN_0|\phi_0(\boldsymbol{x},t)|^2\right]\phi_0(\boldsymbol{x},t) \tag{1.84}$$

This equation can be deduced by extremalization of the action $S = \int dt \int d\boldsymbol{x}\, L$, where the Lagrangian density $L = L[\phi_0, \partial\phi_0, \phi_0^\star, \partial\phi_0^\star, \boldsymbol{x}, t]$ is given by

$$L = -N_0\left[\hbar\,\mathrm{Im}\,(\phi_0^\star\partial_t\phi_0) + \frac{\hbar^2}{2m}\partial_k\phi_0\partial_k\phi_0^\star + U|\phi_0|^2 + \frac{g}{2}N_0|\phi_0|^4\right] \tag{1.85}$$

For compactness, let $x_4 = ict$,[23] and we can define the canonical energy-momentum tensor [110], following the usual field-theory prescription [111]

$$T_{\mu\nu} = -\partial_\nu \phi_0 \frac{\partial L}{\partial(\partial_\mu \phi_0)} - \partial_\nu \phi_0^\star \frac{\partial L}{\partial(\partial_\mu \phi_0^\star)} + L\delta_{\mu\nu} \tag{1.86}$$

where the indices μ, ν run from 1 to 4. As the complex scalar field $\phi_0^\star$ (and ϕ_0) satisfy the Euler-Lagrange equations [112] resulting in Eq. (1.84) (and its complex conjugate), we have

$$\partial_\mu T_{\mu\nu} = \partial_\nu L \tag{1.87}$$

from which energy and momentum conservation immediately follow.[24] To see this explicitly, we split the temporal and spatial parts of Eq. (1.87) to obtain

$$\partial_t T_{44} + ic\partial_k T_{k4} = \partial_t L \tag{1.88}$$

$$\partial_t T_{4l} + ic\partial_k T_{kl} = ic\partial_l L \tag{1.89}$$

Direct subsitution into Eq. (1.86) shows that $T_{44} = -H$, where the energy density H is given by

$$H = N_0 \left(\frac{\hbar^2}{2m} \partial_k \phi_0 \partial_k \phi_0^\star + U|\phi_0|^2 + \frac{g}{2} N_0 |\phi_0|^4 \right) \tag{1.90}$$

while $T_{k4} = \frac{i}{c} S_k$, with the energy flux density

$$S_k = -\frac{N_0 \hbar^2}{m} \operatorname{Re}\left(\partial_t \phi_0^\star \partial_k \phi_0\right) \tag{1.91}$$

Regarding Eq. (1.89), we get $T_{4l} = icJ_l$, with the mass current density (compare to Eq. (1.51))

$$J_l = N_0 \hbar \operatorname{Im}\left(\phi_0^\star \partial_l \phi_0\right) \tag{1.92}$$

and the momentum flux density tensor $\Pi_{kl} \equiv T_{kl}$

$$\Pi_{kl} = \frac{N_0 \hbar^2}{m} \operatorname{Re}\left(\partial_l \phi_0^\star \partial_k \phi_0\right) + \delta_{kl} \left(\frac{g}{2} N_0^2 |\phi_0|^4 - \frac{N_0 \hbar^2}{4m} \partial_i \partial_i |\phi_0|^2 \right) \tag{1.93}$$

Combining all the above, one can rewrite Eq. (1.87) as

$$\partial_t H + \partial_k S_k = N_0 |\phi_0|^2 \partial_t U \tag{1.94}$$

$$\partial_t J_l + \partial_k \Pi_{kl} = -N_0 |\phi_0|^2 \partial_l U \tag{1.95}$$

[23] c is the speed of light, but it is just a constant for our purposes, and will drop out from all final results.

[24] Conservation of angular momentum imposes the additional requirement that $T_{\mu\nu} = T_{\nu\mu}$.

We now focus on Eq. (1.95), which shows momentum conservation. For a more transparent physical interpretation, one can make use of the Madelung transformation Eq. (1.50) and integrate over a volume V, obtaining

$$\partial_t P_l + \oint_S \Pi_{kl} \hat{n}_k dS = -\int_V \rho \partial_l U dV \tag{1.96}$$

where we made use of the divergence theorem for tensor fields [113] in order to express the volume integral as an integral over the surface S which encloses V. Here $\hat{\boldsymbol{n}}$ is the outward-pointing unit normal to S at each point, and we also introduced the total momentum of the field, $\boldsymbol{P} = m\int_V \rho \boldsymbol{v}\, dV$ (with $\boldsymbol{v}$ the velocity Eq. (1.53)). The hydrodynamic form of the momentum flux density then reads

$$\Pi_{kl} = \frac{\hbar^2}{4m\rho}\partial_k\rho\partial_l\rho + m\rho v_k v_l + p\delta_{kl} \tag{1.97}$$

with the pressure $p \equiv \frac{g}{2}\rho^2 - \frac{\hbar^2}{4m}\nabla^2\rho$. We can now write Eq. (1.96) in vector form

$$\int_V \rho \boldsymbol{\nabla} U dV = -\oint_S \left[p\hat{\boldsymbol{n}} + m\rho\boldsymbol{v}\,(\boldsymbol{v}\cdot\hat{\boldsymbol{n}}) + \frac{\hbar^2}{4m\rho}\boldsymbol{\nabla}\rho\,(\boldsymbol{\nabla}\rho\cdot\hat{\boldsymbol{n}})\right] dS - \partial_t \boldsymbol{P} \tag{1.98}$$

and see that the vector between square brackets is the amount of momentum per unit time and area "flowing" through a surface orthogonal to $\hat{\boldsymbol{n}}$.

If we now consider a stationary regime (so that the last term of Eq. (1.98) drops out), and assume the potential U describes some fixed obstacle (such as a cylinder) inside V, then by definition [63] the "drag" force acting on a surface element of the obstacle is the momentum flux though this element. The total force, of course, will be given by the surface integral of the momentum flux, or equivalently, by the volume integral of the potential gradient in Eq. (1.98). While in conservative systems this drag is caused by pressure gradients across the obstacle [114], nonconservative ones such as the resonantly pumped polariton fluid of Chapter 3 also have a viscous contribution to the momentum flux tensor, giving rise to Navier-Stokes-type physics.

Chapter 2

Microcavity exciton-polaritons

In Chapter 1 we have seen, among other things, that interactions are essential for the appearance of superfluidity, and the existence of a BEC is not sufficient. We now want to explore similar physics in the context of nonlinear optical systems, as their nonlinear polarization is able to mediate appreciable interactions between photons [115]. One way to achieve the strong interactions necessary for collective fluid-like behavior of the many-photon system is by coupling the photons with matter degrees of freedom, resulting in new quasiparticles called *polaritons* [116].

The connection between BEC and spontaneous coherence effects in nonlinear optical systems became apparent starting with the experiments on exciton-polaritons in semiconductor microcavities [7, 13, 16, 117]. However, the steady state in such devices typically results from a dynamical balance between driving and dissipation, in contrast to the thermal equilibrium achieved in ultracold atomic gases [2].

In this Chapter we review the physics of microcavity exciton polaritons, with an emphasis on their hydrodynamics properties, and in particular the new effects that their non-equilibrium nature introduces.

This Chapter is organized as follows: we start from a microscopic description of a semiconductor microcavity (Sec. 2.1) in terms of electrons, holes and cavity photons (Sec. 2.2), before switching to a higher level weakly-interacting Bose model for polaritons in Sections 2.3 and 2.4. We discuss various ways of pumping the system, as well as the important roles played by decay (Sec. 2.5) and disorder (Sec. 2.6), leading to a driven-dissipative Gross-Pitaevskii equation at the mean-field level (Sec. 2.7). We investigate the optical limiter and bistable regimes of resonantly pumped polariton condensates, by means of a single-state (pump only) ansatz (Sec. 2.8) for the polaritonic GP equation. Finally, we consider a three-state solution, the optical parametric oscillator regime (Sec. 2.9) obtained by parametric scattering of pump polaritons into the signal and idler states. In Section 2.9, we also review some superfluid-related phenomena in an OPO context, such as quantized vortices, and the $U(1)$ symmetry breaking resulting in a Goldstone mode of the OPO Bogoliubov spectrum.

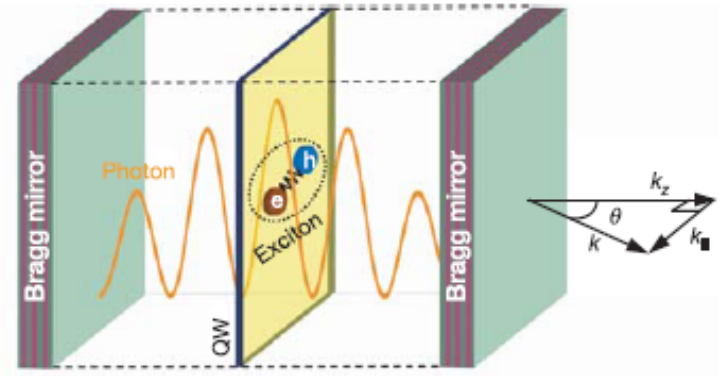

Figure 2.1: Pictorial representation of microcavity polaritons, as electron-hole pairs (excitons) inside a semiconductor quantum well (QW), coupled with the photons trapped by the dielectric Bragg mirrors of the cavity. Momentum conservation dictates that a cavity field component of momentum $\boldsymbol{k}$ must decay into external radiation of frequency ω, emitted at an angle θ satisfying $kc = \omega \sin\theta$. From Ref. [7].

2.1 Model system

Consider the following (simplified) physical system, at zero temperature: we have an optical planar microcavity containing photons confined along the growth direction (say z) by its (identical) metalic mirrors, separated by a distance l_z. At position z_{QW}, the cavity contains a 2D quantum well (QW), which is a thin semiconductor layer sandwitched in between another alloy acting as a barrier. The setup is shown in Fig. 2.1 (for an in-depth introduction to the physics of semiconductor microcavities, see Ref. [6]). The photons create electron-hole hydrogenlike bound pairs (excitons) confined by the barrier inside the QW. Exactly describing the system of electrons, holes and photons, taking into account their Coulomb interaction and the disorder created by defects inside the QW, as well as imperfections present in the cavity mirrors is a daunting task that would provide little physical insight into this system. We therefore use a series of approximations and construct an effective theory that is more physical.

2.2 Microscopic description

We start by writing down the kinetic energy of the cavity photons

$$H_C = \sum_{\boldsymbol{k}} \omega_C(k) a^\dagger_{\boldsymbol{k}} a_{\boldsymbol{k}} \tag{2.1}$$

where we've made use of the translational symmetry of the problem in the (x, y) plane and labeled the bosonic creation (annihilation) operators $a^\dagger_{\boldsymbol{k}}$ ($a_{\boldsymbol{k}}$) by the in-plane momentum $\boldsymbol{k}$. These operators satisfy the standard commutation relations

$$\left[a_{\boldsymbol{k}}, a^\dagger_{\boldsymbol{k}'}\right] = \delta_{\boldsymbol{k},\boldsymbol{k}'} \tag{2.2}$$

$$[a_{\boldsymbol{k}}, a_{\boldsymbol{k}'}] = \left[a^\dagger_{\boldsymbol{k}}, a^\dagger_{\boldsymbol{k}'}\right] = 0 \tag{2.3}$$

The confinement along the z direction leads to the quantization of the photon momentum $k_z = \pi N/l_z$, with $N = 1, 2, \ldots$ indexing the longitudinal modes. Fig. 2.1 depicts the photonic field corresponding to the $N = 5$ mode as a standing wave, representing the measurable electric field inside the cavity. This field can be expressed in terms of photonic operators by $E(\boldsymbol{k}, z)a_{\boldsymbol{k}}+$ H.c., where the photon mode wavefunction $E(\boldsymbol{k}, z)$ has the sinusoidal shape [6]

$$E(\boldsymbol{k}, z) \propto \sqrt{\omega_C(k)/l_z}\sin(k_z z) \tag{2.4}$$

The cavity photon dispersion for each of these modes is therefore $\omega_C(k) = c/n\sqrt{k^2 + k_z^2}$, with c/n the speed of light in the semiconductor. Expanding the square root for $k \ll k_z$, one gets $\omega_C(k) \approx c/nk_z + k^2/(2m_C)$. We see that cavity photons, as opposed to free-space photons, have a quadratic dispersion with an effective mass $m_C = nk_z/c$. For typical cavities used in experiments, m_C is of the order of 10^{-5} (free) electron masses m_e^0 (see Tab. 2.1).

We now turn our attention to the semiconductor QW. For simplicity, consider a spin-polarized direct bandgap semiconductor such as GaAs, so that we can neglect additional spin degrees of freedom. We further assume that the dispersions of single particle states in the conduction and valence bands have the quadratic form $\varepsilon^c_k = \varepsilon_g/2 + k^2/(2m_e)$ and $\varepsilon^v_k = -\varepsilon_g/2 - k^2/(2m_h)$, with ε_g the semiconductor bandgap and m_e and m_h the effective masses for electrons and (heavy) holes. Excitons have a typical "extension" $\lambda_X = \frac{\epsilon}{2\mu e^2}$ (see Tab. 2.1 for typical values for a GaAs-based microcavity) called the (2D) exciton Bohr radius, with ϵ the static dielectric constant, e the electron charge and $\mu^{-1} = m_e^{-1} + m_h^{-1}$ their reduced mass. Their binding energy is called the exciton Rydberg, defined as $\mathcal{R}\mathrm{y}_X = \frac{e^2}{\epsilon\lambda_X}$ (see Tab. 2.1).

We further define $c^\dagger_{\boldsymbol{k}}$ and $v_{\boldsymbol{k}}$ as the operators which create an electron in the empty conduction band, respectively a hole in the filled valence band, and which obey the Fermi anticommutation rules

$$\left\{c_{\boldsymbol{k}}, c^\dagger_{\boldsymbol{k}'}\right\} = \delta_{\boldsymbol{k},\boldsymbol{k}'} \tag{2.5}$$

$$\{c_{\boldsymbol{k}}, c_{\boldsymbol{k}'}\} = \left\{c^\dagger_{\boldsymbol{k}}, c^\dagger_{\boldsymbol{k}'}\right\} = 0 \tag{2.6}$$

and similar for $v_{\boldsymbol{k}}$. We can therefore write the electronic Hamiltonian in terms

of these new operators as [118]

$$H_{\mathrm{el}} = \sum_{\boldsymbol{k}} \left(\varepsilon_k^c c_{\boldsymbol{k}}^\dagger c_{\boldsymbol{k}} + \varepsilon_k^v v_{\boldsymbol{k}}^\dagger v_{\boldsymbol{k}} \right) + \frac{1}{2} \sum_{\boldsymbol{q}} V_q \left(\rho_{\boldsymbol{q}}^e \rho_{-\boldsymbol{q}}^e + \rho_{\boldsymbol{q}}^h \rho_{-\boldsymbol{q}}^h - 2\rho_{\boldsymbol{q}}^e \rho_{-\boldsymbol{q}}^h \right) \tag{2.7}$$

Here we have introduced the electron and hole densities, $\rho_{\boldsymbol{q}}^e = \sum_{\boldsymbol{k}} c_{\boldsymbol{k}+\boldsymbol{q}}^\dagger c_{\boldsymbol{k}}$ and $\rho_{\boldsymbol{q}}^h = \sum_{\boldsymbol{k}} v_{\boldsymbol{k}} v_{\boldsymbol{k}+\boldsymbol{q}}^\dagger$. The matrix element of the Coulomb potential $V_q = \frac{e^2}{2\epsilon A q}$ depends on cavity quantization area A, but this dependence drops out when passing from discrete sums over states to integrals over the momenta $\boldsymbol{k}$.

Finally, the last ingredient of our microscopic description concerns the interaction between electrons and photons. Making use of the dipole approximation, we have

$$H_{\mathrm{dipole}} = \sum_{\boldsymbol{k},\boldsymbol{q}} G(q) \left(a_{\boldsymbol{q}}^\dagger v_{\boldsymbol{k}+\boldsymbol{q}}^\dagger c_{\boldsymbol{k}} + \mathrm{H.c.} \right) \tag{2.8}$$

with the strength $G(k) = e\mu_{\mathrm{cv}} \sqrt{\frac{\omega_C(k)}{2\epsilon A l_z}}$ written in the dipole gauge, where μ_{cv} is the inter-band dipole matrix element.

2.3 Effective Hamiltonian

As mentioned in Sec. 2.1, we are interested in an approximate description of the problem where we can consider the excitons as fundamental quasiparticle excitations from the ground state of the semiconductor and treat the Coulomb term in Eq. (2.7) as an effective exciton-exciton interaction. We then couple the resulting excitons to light, and obtain the so-called *weakly interacting boson model* for polaritons. The name stems from the fact that, at moderate electron-hole densities, such that the inter-exciton distance is much larger than λ_X, one can assume excitons to behave esentially as (composite) bosons [5], and therefore describe them using the Bose creation and annihilation operators $b_{\boldsymbol{k}}^\dagger$ and $b_{\boldsymbol{k}}$. Making an Usui transformation [119] and truncating the interaction terms at fourth order results in the following three-part effective Hamiltonian [12]

$$H_{\mathrm{eff}} = H_0 + H_{\mathrm{XX}} + H_{XC}^{\mathrm{sat}} \tag{2.9}$$

where we have defined

$$H_0 = \sum_{\boldsymbol{k}} \left(a_{\boldsymbol{k}}^\dagger,\, b_{\boldsymbol{k}}^\dagger \right) \begin{pmatrix} \omega_C(k) & \Omega_R \\ \Omega_R & \omega_X(k) \end{pmatrix} \begin{pmatrix} a_{\boldsymbol{k}} \\ b_{\boldsymbol{k}} \end{pmatrix} \tag{2.10}$$

$$H_{\mathrm{XX}} = \frac{1}{2} \sum_{\boldsymbol{k},\boldsymbol{k}',\boldsymbol{q}} U_{\boldsymbol{k}-\boldsymbol{k}',\boldsymbol{q}} b_{\boldsymbol{k}+\boldsymbol{q}}^\dagger b_{\boldsymbol{k}'-\boldsymbol{q}}^\dagger b_{\boldsymbol{k}'} b_{\boldsymbol{k}} \tag{2.11}$$

$$H_{XC}^{\mathrm{sat}} = -\frac{\Omega_R}{\rho_{\mathrm{sat}} A} \sum_{\boldsymbol{k},\boldsymbol{k}',\boldsymbol{q}} \left(b_{\boldsymbol{k}'-\boldsymbol{q}}^\dagger b_{\boldsymbol{k}+\boldsymbol{q}}^\dagger b_{\boldsymbol{k}} a_{\boldsymbol{k}'} + \mathrm{H.c.} \right) \tag{2.12}$$

H_0 contains the kinetic energy of the excitons and cavity photons, as well as their harmonic coupling, ie. the conversion of an exciton to a cavity photon at the Rabi frequency Ω_R, which depends on the overlap between the wavefunctions of the exciton and photon through the oscillator strength surface density $f_{2\mathrm{D}}$ of the excitonic transition

$$\Omega_R \propto \frac{E(z_{\mathrm{QW}})}{E_{\max}} \sqrt{f_{2\mathrm{D}} \omega_C(0)/l_z} \tag{2.13}$$

where $E_{\max}$ is the maximum amplitude of the cavity photon electric field, at one of its antinodes from Eq. (2.4). It is worth noting that both Eq. (2.8) and Eq. (2.10) make use of the rotating-wave approximation, neglecting antiresonant terms which do not conserve the number of excitations, such as $b_{\boldsymbol{k}} a_{\boldsymbol{k}}$ and $b^\dagger_{\boldsymbol{k}} a^\dagger_{\boldsymbol{k}}$. This is justified so long as $\Omega_R \ll \omega_C(0), \omega_X(0)$, which is normally the case, as can be seen in Tab. 2.1, which reports typical parameters of a GaAs-based microcavity with embedded QWs.

Eq. (2.10) can be diagonalized by means of a unitary transformation of the form [116]

$$\begin{pmatrix} p_{\boldsymbol{k}} \\ u_{\boldsymbol{k}} \end{pmatrix} = \begin{pmatrix} X_k & C_k \\ -C_k & X_k \end{pmatrix} \begin{pmatrix} b_{\boldsymbol{k}} \\ a_{\boldsymbol{k}} \end{pmatrix} \tag{2.14}$$

The normal modes of H_0 are called *upper and lower polaritons* (UP and LP) and correspond to the Bose operators $u_{\boldsymbol{k}}$ and $p_{\boldsymbol{k}}$, with eigenenergies

$$\omega_{\mathrm{UP,LP}}(k) = \frac{1}{2}\left(\omega_C(k) + \omega_X(k)\right) \pm \frac{1}{2}\left[\left(\omega_C(k) - \omega_X(k)\right)^2 + 4\Omega_R^2\right]^{1/2} \tag{2.15}$$

where the $\pm$ signs refer to the UP and LP branches and the Hopfield coefficients appearing in Eq. (2.14) are

$$X_k = \left[1 + \left(\frac{\Omega_R}{\omega_{\mathrm{LP}}(k) - \omega_C(k)}\right)^2\right]^{-1/2} \tag{2.16}$$

$$C_k = -\left[1 + \left(\frac{\omega_{\mathrm{LP}}(k) - \omega_C(k)}{\Omega_R}\right)^2\right]^{-1/2} \tag{2.17}$$

The two branches of the polaritonic dispersion relation are shown in Fig. 2.2, together with the dispersions of the cavity photons and excitons. One can therefore think of polaritons as being massive photons dressed by matter excitations.

Note that the 1s-exciton energy can be approximated as $\omega_X(k) = \omega_X(0) + \frac{k^2}{2M}$, with the exciton mass $M = m_e + m_h$ of the order of the electron mass and $\omega_X(0) = \varepsilon_g - \mathcal{R}\mathrm{y}_X$. Since, as we have already noted, M is several orders of magnitude larger than the cavity photon mass m_C, one can in practice neglect the momentum dependence of the excitonic dispersion, considering it as flat compared to the cavity photon one. Furthermore, we can measure energies starting from $\omega_X(0)$ and denote the detuning between exciton and photon bands as

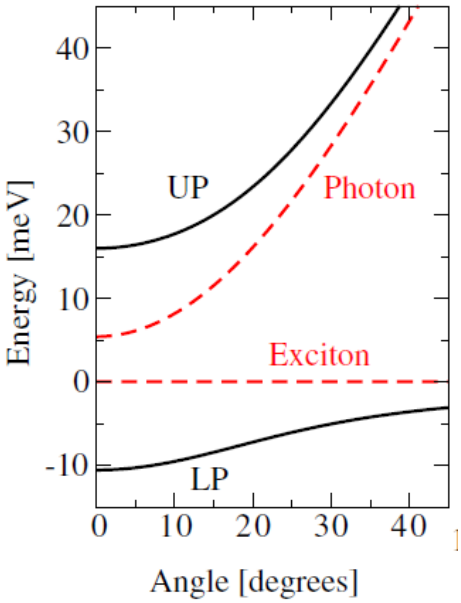

Figure 2.2: Dispersion relation for the two polaritonic branches (UP, LP) as a function of emission angle θ of photons outside the cavity, which is directly related to the momentum $\boldsymbol{k}$ of polaritons inside the cavity. The exciton and cavity photon dispersions are depicted with dashed (red) lines. Due to their light mass, the polaritons have a very sharp dispersion compared to excitons. Also note the typical anticrossing form characteristic of Hermitian coupling. From Ref. [9].

$\delta \equiv \omega_C(0) - \omega_X(0)$. For zero detuning ($\delta = 0$), the splitting between the two polariton branches is $2\Omega_R$. In order to tune δ in experiments, one tipically builds the cavity mirrors with a wedge [120].

H_{XX} quantifies the effective repulsive exciton-exciton interaction, with a momentum dependent strength $U_{\boldsymbol{k}-\boldsymbol{k}',\boldsymbol{q}}$ that can be calculated from the Coulomb exchange term in the Born approximation [121]. A further approximation that one can make for wave vectors much smaller than λ_X^{-1} is to reduce $U_{\boldsymbol{k}-\boldsymbol{k}',\boldsymbol{q}}$ to a contact potential $g_X \equiv \frac{1}{2}U_{\mathbf{0},\mathbf{0}} = \frac{6\epsilon^2\lambda_X}{2A\epsilon}$, as shown in Ref. [121]. As a result, g_X physically represents the interaction between two excitons in the same single-particle momentum eigenstate $|\boldsymbol{k}\rangle$.

Finally, the last term of Eq. (2.9), $H_{\mathrm{XC}}^{\mathrm{sat}}$, can be interpreted as a saturation effect due to the Pauli exclusion principle underlying the fermionic character of the excitons [122]. The exciton saturation density $\rho_{\mathrm{sat}} \sim \frac{7}{16\pi\lambda_X^2}$ generally depends on the specific shape of the internal wavefunction of the exciton [123].

For the problems we will be treating in the remainder of this manuscript it can be considered large enough to justify neglecting this anharmonic contribution to the total Hamiltonian Eq. (2.9) (see Tab. 2.1).

Before concluding this Section, one should mention the validity limitations of the weakly interacting boson model for polaritons reviewed here. Its derivation implies an expansion of the original fermionic operators of Eq. (2.7) in powers of bosonic operators, having as small parameter the number of excitons per Bohr radius λ_X. Truncating this series at fourth order results in an upper bound on the exciton density of around $1/\lambda_X^2$. At higher densities, an electron-hole plasma-like state is formed, with a a qualitatively different behaviour [124]. We see that this model is particularly useful for the case when the dominant interaction is the Coulomb repulsion between the excitons.

2.4 Lower polaritons

Assuming the Rabi energy Ω_R to dominate over the kinetic and interaction energies we can neglect the upper polaritons and project Eq. (2.9) on the basis of lower-polariton states only. Employing the approximations discussed above, we obtain the lower-polariton Hamiltonian

$$H_{\mathrm{LP}} = \sum_{\boldsymbol{k}} \omega_{\mathrm{LP}}(k) p^\dagger_{\boldsymbol{k}} p_{\boldsymbol{k}} + \sum_{\boldsymbol{k},\boldsymbol{k}',\boldsymbol{q}} V^{\mathrm{eff}}_{\boldsymbol{k},\boldsymbol{k}',\boldsymbol{q}}\, p^\dagger_{\boldsymbol{k}+\boldsymbol{q}} p^\dagger_{\boldsymbol{k}'-\boldsymbol{q}} p_{\boldsymbol{k}} p_{\boldsymbol{k}'} \tag{2.18}$$

where the strength of the repulsive interaction between lower polaritons now depends on in-plane momentum through the Hopfield coefficients[1]

$$V^{\mathrm{eff}}_{\boldsymbol{k},\boldsymbol{k}',\boldsymbol{q}} = g_X X_{\boldsymbol{k}+\boldsymbol{q}} X_{\boldsymbol{k}'-\boldsymbol{q}} X_{\boldsymbol{k}} X_{\boldsymbol{k}'} \tag{2.19}$$

This effective interaction, originating from the binary Coulomb scattering of the excitons, is the one responsible for the collective behaviour of the polaritons, and in particular superfluid hydrodynamics, an aspect which we will explore in the following two Chapters.

Physically, the quantities $|X_k|^2$ and $|C_k|^2$ are the excitonic and photonic fractions of the lower polariton mode and the effective mass of the lower polaritons, m_{LP}, can be computed from the curvature of their dispersion Eq. (2.15) by

$$m_{\mathrm{LP}}(k) = \left[\frac{d^2\omega_{\mathrm{LP}}(k)}{dk^2}\right]^{-1} \tag{2.20}$$

which at normal incidence $\boldsymbol{k} = 0$ reduces to

$$m_{\mathrm{LP}} = 2m_C \left[1 - \delta/\sqrt{\delta^2 + 4\Omega_R^2}\right]^{-1} \tag{2.21}$$

[1]The interaction strength g_X can usually be rescaled to 1 by a simple transformation.

if we neglect the flat exciton dispersion in the limit $M \gg m_C$. For zero detuning, we see that $m_{\mathrm{LP}} = 2m_C$ and the light and matter content of lower polaritons are each equal to 1/2.

As long as the interesting physics is limited to small (compared to $\sqrt{m_{\mathrm{LP}}\Omega_R}$) wavevectors $\boldsymbol{k}$, close to the bottom of the LP branch, one can safely approximate the LP dispersion as being parabolic, by expanding Eq. (2.15) in a Taylor series around $\boldsymbol{k} = 0$ and truncating at second order. We obtain the expression

$$\omega_{\mathrm{LP}}(k) \simeq \omega_{\mathrm{LP}}(0) + \frac{k^2}{2m_{\mathrm{LP}}} \tag{2.22}$$

with an effective mass given by Eq. (2.21). In practice, many interesting experimental conditions can be adequately described by limiting ourselves to the LP branch with a quadratic dispersion.

2.5 Pumping and dissipation

We have so far assumed that the mirrors at the two ends of the optical cavity in Fig. 2.1 are perfect. In reality of course, this is not the case, and photons continuously escape from the cavity. In other words, decay is a built-in feature of this system and, rather than being a hindrance, it is actually useful as it allows one to extract information about the system. By looking at the near-field (far-field) emission from the cavity, one can measure the real (momentum) space photon density. The polaritonic spectrum can also be obtained in this way, as a function of the angle θ of emission of a photon out of the cavity, as shown in Fig. 2.2.

Since the system is lossy, one needs to drive it by means of an incoming laser beam (called the pump), thus replenishing the photons and achieving a stationary state. It is important to note, however, that this state should not be confused with thermal equilibrium, as we are dealing with intrinsic out-of-equilibrium physics here. Experiments have so far explored two main ways of pumping these cavities: resonantly (coherent) and non-resonantly (incoherent). We will not concern ourselves with the latter in this manuscript, but we point the interested reader to the excelent review in Ref. [2] (and references therein) for details.

Resonant pumping is done by means of a continuous-wave coherent laser beam which is transmitted through one of the mirrors, at energies and momenta close to the LP or UP. The coherence of the beam is then inherited by the polariton fluid. As already mentioned, conservation of in-plane momentum and photon frequency dictates that a laser wave coming in at an angle θ and frequency ω resonantly excites a microcavity mode with wavevector $k = \frac{\omega}{c}\sin(\theta)$ (see Fig. 2.1). As a result, we see that, besides balancing the losses, the pump can also be used to tune the system to a particular desired state, injecting polaritons of a given momentum and energy. In the following we will consider that the pumping is done

quasi-resonantly, close to the bottom of the LP branch, by using a homogeneous planewave pump of amplitude f_p, wavevector $\boldsymbol{k}_p$, frequency ω_p

$$\mathcal{F}(\boldsymbol{r},t) = f_p \exp\left[i(\boldsymbol{k}_p \cdot \boldsymbol{r} - \omega_p t)\right] \tag{2.23}$$

Depending on the pump parameters (specifically the pumping angle, which in turn determines k_p), one can distinguish two qualitatively different regimes: 1) the pump-only state where the only stable configuration of the system is the mode at k_p and 2) the regime where polaritons at k_p undergo stimulated scattering and populate two other modes. Indeed, if the pumping angle is such that the wavevector it excites lies above the inflection point of the LP dispersion, the system can enter a new regime called *optical parametric oscillator* (see Sec. 2.9 for details about OPO).

To quantitatively account for the driving and decay, one can use the input-output formalism that was extended to planar microcavities in Ref. [125]. As far as photonic losses are concerned, we must first note that, apart from the radiative decay channels already mentioned, there is also a nonradiative contribution due to photon absorbtion inside the cavity. The total cavity photon decay rate γ_C can therefore be expressed as the sum $\gamma_C^{\mathrm{rad}} + \gamma_C^{\mathrm{nrad}}$, where the radiative decay rate is [2, 126]

$$\gamma_C^{\mathrm{rad}}(\boldsymbol{k}) = \frac{ct^2}{2l_z} \tag{2.24}$$

for normal incidence, where c is the speed of light in vacuum and t the mirror transmittivity.

The excitons from the QW are of course also subject to decay processes. While their radiative decay can only take place via one of the cavity modes (due to strong light-matter coupling[2]), we must include nonradiative recombination processes as well as the additional dephasing [127] caused by interactions with carriers inside the well and variations in well thickness. All this results in an effective decay rate γ_X for excitons, which is generally weaker than the photonic one quantified by γ_C. Typical values of both rates for GaAs-based microcavities are shown in Tab. 2.1.

2.6 Disorder effects

It is noteworthy to remark that Hamiltonian Eq. (2.9) does not include any disorder. We have already mentioned that there are two distinct disorder classes in this problem. One is the excitonic disorder, acting on length scales of around 10 nanometers, which tipically affects the exciton oscillator strengths $f_{2\mathrm{D}}$, but not the spatial polaritonic density. This type of disorder stems from variations in the QW thickness as well as alloy imperfections and is typically not strong

[2]In general, one is in the strong coupling regime when Ω_R is greater than the combined losses in the system.

enough to dissociate excitons. Neglecting excitonic disorder also implies that each localized exciton state couples to precisely one extended photon state. The resulting polaritons are then nothing but the coherent superposition of these excitonic and photonic states.

Photonic disorder, on the other hand, acts on lengthscales $\ell_C = (m_C\Omega_R)^{-1/2}$ on the order of microns (see Tab. 2.1) and therefore can disrupt the polariton density profile. Photonic disorder is normally caused by the presence of imperfections inherent to the growth process of the cavity mirrors. These defects (as well as any layer mismatch) act as scattering centers for the polaritons, and can be included in the Hamiltonian as an additional external scalar potential. The simplest example is that of a spatially localized defect of strength g_V located at positon $\boldsymbol{r}_0$, which can be approximated by the potential

$$\tilde{V}_d(\boldsymbol{r}) = g_V\delta^2(\boldsymbol{r} - \boldsymbol{r}_0) \tag{2.25}$$

To get a more quantitative idea of the physics involved, it is worth describing realistic samples typically used in state-of-the-art experiments. Instead of simple metallic mirrors, such microcavities are usually bound by a series of up to around 20 distributed Bragg reflectors (DBRs), which are alternating dielectric layers of thickness $\lambda/4$ and different refractive indices, achieving a total reflectivity of over 99.9% [6].

Multiple CdTe (or GaAs, GaN, ZnO) QWs a few nanometers thick are placed inside the cavity of length $l_z = 2\lambda \sim 1$ μm, at the antinodes (maxima) of the photonic electric field, in order to maximize the coupling between excitons and photons (see Eq. (2.13), which shows maximum coupling for $E(z_{\mathrm{QW}}) = E_{\max}$). When N distinct QWs are placed in the cavity at the electric field maxima, the light-matter coupling Ω_R is enhanced by a factor $\sqrt{N}$. Furthermore, the cavity cutoff frequency $\omega_C(0)$ is normally chosen close to the exciton frequency $\omega_X(0)$.

Typical values of the relevant parameters for GaAs-based microcavities are shown in Tab. 2.1.

2.7 Mean-field description

As it turns out, a useful approach for tackling the hydrodynamics-related problems that we will encounter in the following Chapters is the so-called mean-field approximation. In the context of conservative, weakly interacting Bose gases at thermal equilibrium, this approach leads to the celebrated Gross-Pitaevskii equation [50], and in our case it will lead to its driven-dissipative counterpart.

If the Rabi energy is larger than the pump detuning from the bottom of the LP branch $\omega_p - \omega_{\mathrm{LP}}(0)$ and also larger than the decay rates γ_X and γ_C, we can start from the lower polariton Hamiltonian of Sec. 2.4. The idea is that one replaces the lower polariton operators $p_{\boldsymbol{k}}$ in Eq. (2.18) with their expectation values $\psi_{\boldsymbol{k}} = \langle p_{\boldsymbol{k}}\rangle$, where $\psi_{\boldsymbol{k}}$ is now interpreted as a classical field (order parameter representing lower polariton polarization) describing the state with momentum

QW	Cavity
$\epsilon \simeq 13$	$\omega_C(0) \simeq \omega_X(0) \simeq 1.53$ eV
$m_e = 0.063 m_e^0$	$\delta \in [-10, 10]$ meV
$m_h = 0.3 m_e^0$	$m_C = 2.3 \times 10^{-5} m_e^0$
$\lambda_X \simeq 7$ nm	$\ell_C = 0.868$ μm
$\mathcal{R}\mathrm{y}_X \simeq 17$ meV	$\Omega_R \simeq 2.2$ meV
$\gamma_X \sim \mu$eV	$\gamma_C = 0.1$ meV
$g_X \simeq 5 \times 10^{-3}$ meV$(\mu\mathrm{m})^2$	$A \sim 10^4$ μm^2
$\rho_{\mathrm{sat}} \simeq 2842$ $(\mu\mathrm{m})^{-2}$	$l_z \sim 1$ μm

Table 2.1: Typical parameters of a GaAs-based microcavity with embedded QWs. Left column shows properties of a QW, while the right one refers to the microcavity. For these values, the ratio between saturation and Coulomb interaction is small, $\Omega_R/(g_X \rho_{\mathrm{sat}}) \simeq 0.1$. From Ref. [128].

label $\boldsymbol{k}$. The mean-field equation for $\psi_{\boldsymbol{k}}$ is then obtained from the Heisenberg equation of motion $\dot{p}_{\boldsymbol{k}} = i\,[H_{\mathrm{LP}},\, p_{\boldsymbol{k}}]$ by replacing all the operators with their corresponding expectation values. This mean-field treatment is of course exact as far as the pumping and the losses are concerned, as well as for any two-operator product such as the polariton kinetic energy. However, the effective lower polariton interactions are approximated following an approach similar to the one pioneered by Bogoliubov in the context of atomic BECs, namely

$$\langle p^\dagger_{\boldsymbol{k}_1+\boldsymbol{k}_2-\boldsymbol{k}} p_{\boldsymbol{k}_2} p_{\boldsymbol{k}_1} \rangle \approx \langle p_{\boldsymbol{k}_1+\boldsymbol{k}_2-\boldsymbol{k}} \rangle^\star \langle p_{\boldsymbol{k}_2} \rangle \langle p_{\boldsymbol{k}_1} \rangle \tag{2.26}$$

We obtain a generalized Gross-Pitaevskii equation (GPE) in momentum space under coherent driving, which includes losses and describes the time evolution of $\psi_{\boldsymbol{k}}(t)$

$$\begin{aligned} i\partial_t \psi_{\boldsymbol{k}} = \left[\omega_{\mathrm{LP}}(k) - \frac{i}{2}\gamma_k\right]\psi_{\boldsymbol{k}} + \sum_{\boldsymbol{k}_1,\boldsymbol{k}_2} g_{\boldsymbol{k},\boldsymbol{k}_1,\boldsymbol{k}_2}\, \psi^\star_{\boldsymbol{k}_1+\boldsymbol{k}_2-\boldsymbol{k}} \psi_{\boldsymbol{k}_2} \psi_{\boldsymbol{k}_1} \\ + C_{\boldsymbol{k}} \sum_{\boldsymbol{q}} C_{\boldsymbol{q}} V_d(\boldsymbol{k}-\boldsymbol{q}) \psi_{\boldsymbol{q}} + C_{\boldsymbol{k}} f_p \exp(-i\omega_p t)\delta_{\boldsymbol{k},\boldsymbol{k}_p} \end{aligned} \tag{2.27}$$

Here $\gamma_k = \gamma_X |X_k|^2 + \gamma_C |C_k|^2$ is the (lower) polariton loss rate, $V_d(\boldsymbol{k})$ is the Fourier transform of the external potential Eq. (2.25) and the effective polariton-polariton interaction strength is given by

$$g_{\boldsymbol{k},\boldsymbol{k}_1,\boldsymbol{k}_2} = g_X X_{\boldsymbol{k}} X_{|\boldsymbol{k}_1+\boldsymbol{k}_2-\boldsymbol{k}|} X_{\boldsymbol{k}_1} X_{\boldsymbol{k}_2} \tag{2.28}$$

Going beyond the mean-field approximation to include quantum and thermal fluctuations of the (quantum) field $\hat{\psi}_{\boldsymbol{k}}$ is not an easy task in general, see Ref. [2] for some approaches such as using the semiclassical Wigner representation.

In order to obtain the corresponding form of Eq. (2.27) in real-space, we introduce the Fourier transform of the classical wavefunction $\psi_{\boldsymbol{k}}$ by means of[3]

$$\tilde{\psi}(\boldsymbol{r}) = \int \frac{d^2\boldsymbol{k}}{(2\pi)^2}\psi(\boldsymbol{k})\exp\left(i\boldsymbol{k}\cdot\boldsymbol{r}\right) \tag{2.29}$$

Knowing that Fourier transforms take multiplication to convolution, we immediately get the real-space equation for $\tilde{\psi}(\boldsymbol{r},t)$

$$\begin{aligned} i\partial_t\tilde{\psi}(\boldsymbol{r}) = &\left[\omega_{\mathrm{LP}}(-i\boldsymbol{\nabla}) - \frac{i}{2}\gamma(-i\boldsymbol{\nabla})\right]\tilde{\psi}(\boldsymbol{r}) \\ &+ \int d\boldsymbol{r}_{1,2,3}\,\tilde{g}(\boldsymbol{r}_1-\boldsymbol{r},\boldsymbol{r}-\boldsymbol{r}_2,\boldsymbol{r}-\boldsymbol{r}_3)\tilde{\psi}^\star(\boldsymbol{r}_1)\tilde{\psi}(\boldsymbol{r}_2)\tilde{\psi}(\boldsymbol{r}_3) \\ &+ \int d\boldsymbol{r}_{1,2}\,\tilde{C}(\boldsymbol{r}-\boldsymbol{r}_1)\tilde{C}(\boldsymbol{r}_1-\boldsymbol{r}_2)\tilde{V}_d(\boldsymbol{r}_1)\tilde{\psi}(\boldsymbol{r}_2) + C(\boldsymbol{k}_p)\mathcal{F}(\boldsymbol{r},t) \end{aligned} \tag{2.30}$$

Note that the kinetic energy operator has a particular dependence on the gradient instead of the usual Laplacian, reflecting the non-parabolic LP dispersion. Furthermore, the nonlocal interaction term in the second line of Eq. (2.30) has the form of the most general third order nonlinear term that one can come up with, if $\tilde{g}$ were an arbitrary function. This freedom is somewhat restrained in practice by the fact that $\tilde{g}$ is related to Eq. (2.28) by

$$\tilde{g}(\boldsymbol{r}_1,\boldsymbol{r}_2,\boldsymbol{r}_3) = \int d\boldsymbol{k}_{1,2,3}\,g(\boldsymbol{k}_1,\boldsymbol{k}_2,\boldsymbol{k}_3)\exp\left[i\textstyle\sum_{n=1}^{3}(\boldsymbol{k}_n\cdot\boldsymbol{r}_n)\right] \tag{2.31}$$

and we have also introduced the functions $\tilde{C}(\boldsymbol{r})$, which are the Fourier transforms of the Hopfield coefficients $C(\boldsymbol{k})$. These coefficients do not have a very pronounced momentum dependence, as in fact for $\delta = 0$, $X(\boldsymbol{k})$ is between $1/\sqrt{2}$ and 1. If we neglect altogether the Hopfield coefficients in Eq. (2.30) and consider the case of parabolic lower polariton dispersion, we finally obtain the real-space driven-dissipative GPE in its simplified form

$$i\partial_t\tilde{\psi}(\boldsymbol{r}) = \left[\omega_{\mathrm{LP}}(0) - \frac{\nabla^2}{2m_{\mathrm{LP}}} - \frac{i}{2}\gamma + \tilde{V}_d(\boldsymbol{r}) + g_X|\tilde{\psi}(\boldsymbol{r})|^2\right]\tilde{\psi}(\boldsymbol{r}) + \mathcal{F}(\boldsymbol{r},t) \tag{2.32}$$

Here we have also neglected the momentum dependence of the polariton loss rate, justified by the fact that, at large momenta, the diminishing radiative width is normally compensated by non-radiative broadening. To make a stronger connection with nonlinear optics, we note that a similar equation holds for cavities containing a nonlinear medium, with the role of g_X being taken by the $\chi^{(3)}$ susceptibility of the medium [129]. This equation allows for an ab-initio description of the coherently pumped system, unlike the more complicated case of incoherent

[3]Replacing the discrete sums over $\boldsymbol{k}$ states by continuous integrals is justified in the limit of a large system.

pumping where one generally also needs a phenomenological description of the various relaxation processes [9].

Before moving on, we note that one can also describe the dynamics of polaritons scattering against a defect using the two-component GPE [2, 130] for the coupled exciton and cavity fields $\psi_{X,C}(\mathbf{r},t)$:

$$i\partial_t \begin{pmatrix} \psi_X \\ \psi_C \end{pmatrix} = \hat{H} \begin{pmatrix} \psi_X \\ \psi_C \end{pmatrix} + \begin{pmatrix} 0 \\ \mathcal{F}(\mathbf{r},t) \end{pmatrix} , \tag{2.33}$$

where

$$\hat{H} = \begin{pmatrix} \omega_X(-i\nabla) - i\frac{\gamma_X}{2} + g_X|\psi_X|^2 & \Omega_R \\ \Omega_R & \omega_C(-i\nabla) - i\frac{\gamma_C}{2} + \tilde{V}_d \end{pmatrix} . \tag{2.34}$$

Eq. (2.33) is usually solved numerically, as we shall see in Chapter 4.

2.8 Equation of state

Because we drive the system with the coherent plane-wave continuous pump Eq. (2.23), we can look for stationary state solutions with similar oscillatory behaviour

$$\psi(\boldsymbol{r},t) = \psi_p e^{i(\boldsymbol{k}_p\cdot\boldsymbol{r}-\omega_p t)} \tag{2.35}$$

In absence of an external potential, inserting this ansatz into Eq. (2.27), we obtain the equation of state for lower polaritons

$$\left[\omega_p - \omega^p_{\mathrm{LP}} - g_X X_p^4|\psi_p|^2 + \frac{i}{2}\gamma_p\right]\psi_p = C_p f_p \tag{2.36}$$

where we employ the simplified notation $\gamma_p \equiv \gamma(\boldsymbol{k}_p)$, $C_p \equiv C(\boldsymbol{k}_p)$, $X_p \equiv X(\boldsymbol{k}_p)$ and $\omega^p_{\mathrm{LP}} \equiv \omega_{\mathrm{LP}}(\boldsymbol{k}_p)$. One immediately notices that, unlike the case of the atomic mean-field Eq. (1.28), the phase of the polariton field amplitude ψ_p is set by the pump, therefore explicitly breaking the $U(1)$ gauge symmetry associated with global rotations of the condensate phase. This implies that, unlike the atomic BECs, no Goldstone branch will be present in the polaritonic excitation spectrum. Note also that the oscillation frequency of the condensate wavefunction is fixed by the pump frequency ω_p. In Chapter 3, we will compare the main features of the quasiparticle excitation spectrum for polaritons to equilibrium systems like cold atomic gases in the BEC regime. Furthermore, a locked phase clearly prevents the formation of phase dislocations, such as vortices and solitons. For this reason, it has been suggested [131] and experimentally realised [132] that the defect can be located just outside the pump spot, leaving the condensate phase unbound and allowing hydrodynamic nucleation of vortices, vortex-antivortex pairs, arrays of vortices, and solitons to be observed when the fluid collides with the extended defect. Similarly, nucleation of vortices in the wake of the obstacle has been observed in pulsed experiments [133, 134].

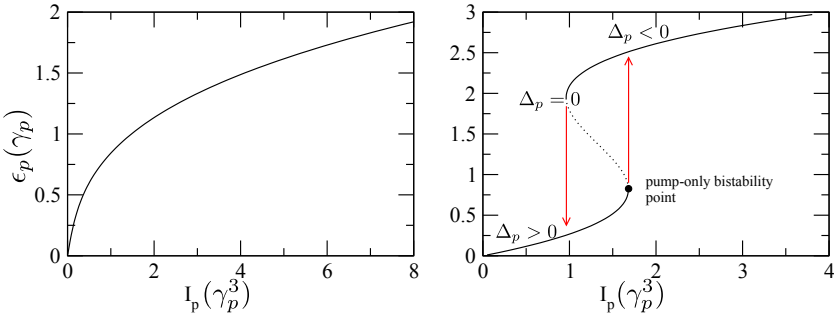

Figure 2.3: Pump energy blueshift of Eq. (2.37) as a function of pump laser intensity in the optical limiter (left panel) and bistable (right panel) regimes. The arrows in the right panel show the hysteretic jumps between the lower and upper branches at different intensities, while the dotted middle branch is single-mode unstable. The black dot marks a saddle node bifurcation. From Ref. [135].

The repulsive polaritonic interaction is responsible for a blueshift of the LP dispersion $\omega^p_{\rm LP}$. Introducing the pump energy blueshift $\epsilon_p = g_X X_p^2 |\psi_p|^2$, we can rewrite Eq. (2.36) in absolute value as

$$\left[\left(\frac{\omega_p - \omega^p_{\rm LP}}{\gamma_p} - X_p^2 \frac{\epsilon_p}{\gamma_p}\right)^2 + \frac{1}{4}\right] \frac{\epsilon_p}{\gamma_p} = X_p^4 \frac{I_p}{\gamma_p^3} \tag{2.37}$$

where we have also defined the pump laser intensity $I_p = g_X C_p^2 |f_p|^2 / X_p^2$. One can now distinguish two qualitatively different regimes, based on the value of the bare pump detuning $\omega_p - \omega^p_{\rm LP}$. The first regime, called *optical limiter* is for $\omega_p - \omega^p_{\rm LP} \leq \sqrt{3}\gamma_p/2$ and it is plotted in the left panel of Fig. 2.3. We see that the pump blueshift increases monotonically with increasing pump power. The increase is sublinear, as the blueshift moves the lower polariton dispersion out of resonance with the pump.

The second regime $\omega_p - \omega^p_{\rm LP} > \sqrt{3}\gamma_p/2$, shown in the right panel of Fig. 2.3, is called *optical bistability* and is no longer monotonic. The blueshift-intensity curve has a characteric S-shape, and shows hysteresis: increasing the pump power, we get to the first turning point (filled circle in the figure) where the blueshift suddenly jumps from the low to the high branch, while the reverse process of decreasing the pump power shows a jump at a second turning point on the S curve. Defining an interaction-renormalized pump detuning $\Delta_p \equiv \omega_p - (\omega^p_{\rm LP} + X_p^2 \epsilon_p)$, we see that this quantity is positive up to the second turning point on the S curve, and then changes sign, becoming negative on the higher branch.

The middle branch of the S curve, with negative slope, is dynamically unstable, while the two turning points where the stable and unstable solutions meet are called *saddle node* bifurcations. To see this, one must consider small pertur-

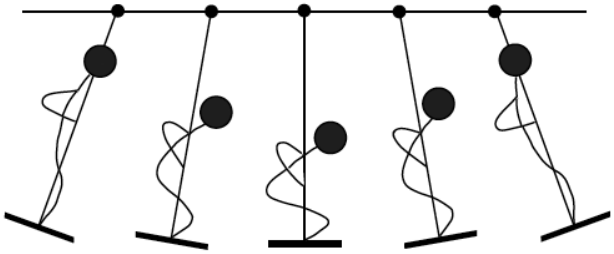

Figure 2.4: The driving (pumping) of a swing by a person, using the standing position, shown as an (albeit contrived) example of a degenerate parametric amplifier. From Ref. [136].

bations of wave-vector $\boldsymbol{k}$ of the form

$$\delta\psi(\boldsymbol{r},t)=\sum_{\boldsymbol{k},\omega}\left\{u_p e^{i[(\boldsymbol{k}_p+\delta\boldsymbol{k})\cdot\boldsymbol{r}-(\omega_p+\omega)t]}+v_p^{\star}e^{i[(\boldsymbol{k}_p-\delta\boldsymbol{k})\cdot\boldsymbol{r}-(\omega_p-\omega)t]}\right\} \tag{2.38}$$

where $\delta\boldsymbol{k}\equiv\boldsymbol{k}-\boldsymbol{k}_p$. Substituting this into Eq. (2.27) and linearising with respect to the amplitudes u_p and v_p, we obtain an eigenvalue problem from which the two (complex) eigenvalues ω can be determined in a straightforward manner.

Dynamical stability is then ensured when $\Im\left[\omega(\boldsymbol{k})\right]<0$ for any wave-vector $\boldsymbol{k}$. We can therefore distinguish two main types of instabilities, depending on the value of $\delta\boldsymbol{k}$: for $\delta\boldsymbol{k}=0$ (the degenerate case), the system shows a *Kerr single-mode* (or pump-only) instability which only involves the pump wave-vector, while the general case of $\delta\boldsymbol{k}\neq 0$ implies a *parametric* instability, signaling the onset of the optical parametric oscillator (OPO) regime. This regime involves two separate modes (apart from the pump), namely the so-called *signal* and *idler* states at wavevectors $\boldsymbol{k}_s=\boldsymbol{k}$ and $\boldsymbol{k}_i=2\boldsymbol{k}_p-\boldsymbol{k}$ respectively, as we will discuss at large in Sec. 2.9.

2.9 OPO regime

To understand why the OPO regime arises, one has to first look at the form of the Heisenberg equation of motion Eq. (2.27). This equation describes the coupled dynamics of an arbitrary state $\boldsymbol{k}$, given an applied optical field which excites polaritons with in-plane wavevector $\boldsymbol{k}_p$. As a result of polariton-polariton interactions, the coherent occupation at generic wavevectors $\boldsymbol{k}_1$ and $\boldsymbol{k}_2$ can scatter into $\boldsymbol{k}$ and $\boldsymbol{k}_1+\boldsymbol{k}_2-\boldsymbol{k}$, a process one can represent as

$$\{\boldsymbol{k}_1,\boldsymbol{k}_2\}\rightarrow\{\boldsymbol{k},\boldsymbol{k}_1+\boldsymbol{k}_2-\boldsymbol{k}\} \tag{2.39}$$

As these states further scatter into others by the same matter wave-mixing mechanism, we get a cascade of so-called satellite states, with diminishing population.

Out of the multitude of possible scattering channels, we limit our description to the one describing the process $\{\boldsymbol{k}_p, \boldsymbol{k}_p\} \rightarrow \{\boldsymbol{k}, 2\boldsymbol{k}_p - \boldsymbol{k}\}$, which is precisely the parametric scattering of two pump polaritons into the signal and idler states that we just introduced in Sec. 2.8. As it turns out, due to the peculiar shape of the lower polariton dispersion relation Eq. (2.15), this scattering process can occur in a completely resonant way, with conservation of both in-plane momentum as well as energy, expressed by the phase-matching conditions $2\boldsymbol{k}_p = \boldsymbol{k}_s + \boldsymbol{k}_i$ and $2\omega_p = \omega_s + \omega_i$ (we have introduced here the signal and idler frequencies). The parametric scattering condition that has to be satisfied then reads

$$2\omega_{\mathrm{LP}}(\boldsymbol{k}_p) = \omega_{\mathrm{LP}}(\boldsymbol{k}_s) + \omega_{\mathrm{LP}}(\boldsymbol{k}_i) \tag{2.40}$$

We must further emphasize the importance of the unique form of the LP dispersion in Eq. (2.40), as it allows efficient parametric coupling on a relatively broad range of pump momenta. Parametric scattering would not be possible for particles with a quadratic dispersion: in the atomic case for instance, one must employ the use of an optical lattice in order to deform the dispersion and promote parametric amplification [137].

While this may all seem far-removed from everyday experience, we remind the reader that parametric amplifiers and oscillators are commonly found in mechanical (as well as electronic) systems. For instance, one can consider a person on a swing in the standing position, as shown in Fig. 2.4 (and described in detail in Ref. [138]). In this particular example, we are dealing with a degenerate parametric amplifier, as the signal and idler have the same frequency and are represented by the swing. The person driving the swing then acts as the pump, and one can see that his (or hers) up-down motion has a periodicity which is twice that of the swing, therefore $\omega_p = 2\omega_s$ in this case.

A schematic depiction of the polariton parametric scattering process with the signal state located at zero momentum and the pump close to the inflection point of the LP dispersion is shown in Fig. 2.5. It is clear that for a given signal wavevector, Eq. (2.40) then uniquely determines the pump and idler states. The fact that $\boldsymbol{k}_s$ is close to 0 is not incidental, but was observed in multiple experiments [139, 140] performed in the OPO regime, as well as numerical simulations of the full GP equation [128]. An intuitive explanation was put forward [130, 141], based on the interaction-induced blueshift of the LP dispersion.

We now turn our attention to the mechanism explaining the onset of the parametric scattering instability in the simple case of the optical limiter regime shown in the left panel of Fig. 2.3. As already mentioned, the polariton-polariton repulsive interaction causes a blueshift of the LP dispersion proportional to the pump mode population $|\psi_p|^2$. This shift also affects the signal and idler frequencies $\omega_{\mathrm{LP}}(\boldsymbol{k}_{s,i})$, bringing them in resonance with the pump frequency ω_p. The pump population (and hence the shift) of the optical limiter is a monotonically

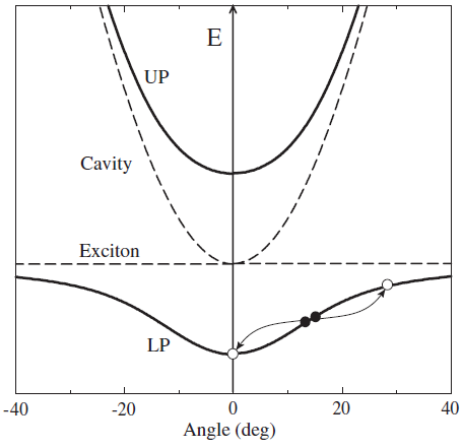

Figure 2.5: Upper (UP) and lower (LP) polariton dispersions are shown as solid lines, while the original exciton and cavity photon are represented by dashed lines, as a function of the laser incidence angle θ. The filled circles represent two pump polaritons being parametrically scattered into the signal (here at 0 angle) and idler states, shown as empty circles. The scattering process depicted by the curved arrows is resonant, conserving both energy and momentum. From Ref. [12].

increasing function of laser intensity, quantified by Eq. (2.37). As a result, there is a certain minimum *threshold intensity* where the resonance starts and the pump-only solution becomes unstable towards parametric scattering. Further increasing the laser power, we hit an upper threshold, where the blueshift becomes too large and the resonance is lost, forbiding parametric oscillation. This mechanism defines a certain window of pump intensities where the parametric instability can arise, the region depicted by the dashed line in Fig. 2.6. Inside this window, the pump-only solution still exists, but it is unstable towards OPO.

The simplest ansatz one can make for describing the OPO regime above threshold is to consider the three separate states (signal, pump and idler), each with its own population, wavevector and frequency, in the form [10, 130, 141, 142]

$$\psi(\boldsymbol{r},t) = \psi_s e^{i(\boldsymbol{k}_s\cdot\boldsymbol{r}-\omega_s t)} + \psi_p e^{i(\boldsymbol{k}_p\cdot\boldsymbol{r}-\omega_p t)} + \psi_i e^{i(\boldsymbol{k}_i\cdot\boldsymbol{r}-\omega_i t)} \tag{2.41}$$

where energy and momentum conservation dictate that $\omega_i = 2\omega_p - \omega_s$ and $\boldsymbol{k}_i = 2\boldsymbol{k}_p - \boldsymbol{k}_s$. As before, we insert this ansatz into Eq. (2.27) and we obtain three coupled complex nonlinear equations for $\psi_{s,p,i}$ which determine the dynamics of the signal, pump and idler. It is important to note that these equations become closed only if we neglect the multiple scattering processes mentioned at the start of this Section and consider only the conversion of two pump polaritons into

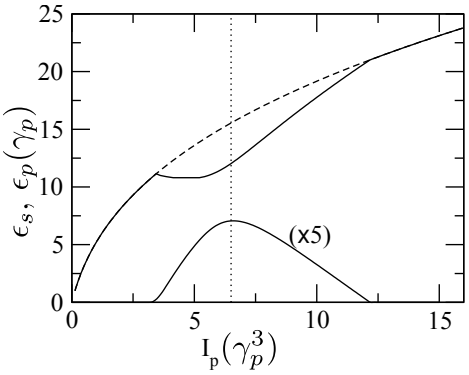

Figure 2.6: OPO pump (upper solid curve) and signal (lower curve, magnified 5 times) energy blueshifts in the optical limiter regime, as a function of pump laser intensity. The dashed line is the pump blueshift in the pump-only solution Eq. (2.37). The vertical dotted line marks the pump intensity used in Fig. 2.7. From Ref. [29].

a signal and an idler polariton. We will not give the full form of these OPO equations of state, but instead refer the reader to Ref. [135], where a complete discussion of the oscillation threshold and ensuing dynamics is given. Fig. 2.6 shows a particular solution of the equations for the optical limiter case. One can see the smooth growth of the signal population (and subsequent depletion of the pump) inside the OPO (dashed) region. It is of course never implied that the whole OPO window is dynamically stable, and in fact a stability analysis needs to be performed by adding small fluctuations on top of the (now) three coupled states, in a manner similar to Eq. (2.38), following Ref. [29]. The complete treatment will be presented in Chapter 4.

Before moving on, it is worth noting that a limitation of the ansatz Eq. (2.41) is that it does not allow solving the so-called "selection" problem of determining the value of $\boldsymbol{k}_s$ above threshold. As a result, this value has to be considered as an input parameter to our problem. Futhermore, similarly to the pump-only case and inherent in any mean-field approach, we are of course neglecting any quantum fluctuations of the three macroscopically occupied modes. Last but not least, we are also neglecting the so-called TE-TM (transverse electric - transverse magnetic) splitting [143], which can act as an effective spin-orbit interaction term [144]. This approximation allows one to work with a single spin state, considering the circular polarization of the pump to be fully transmitted to the signal and ider as well.

We now turn our attention to a separate discussion, concerning the phases of the three OPO states. As before, the phase of the pump is fixed by the outside laser, and now the sum of the signal and idler phases is given by the matching

condition $\phi_s + \phi_i = 2\phi_p$. Their phase difference however is a free parameter, and as such it is spontaneously chosen by the system every time the threshold is crossed. In summary, the OPO equations of motion for the three states posess a $U(1)$ symmetry, corresponding to a simultaneous and opposite phase rotation of the signal and idler, that is

$$\begin{aligned} \psi_s &\to \psi_s e^{i\phi} \\ \psi_i &\to \psi_i e^{-i\phi} \end{aligned} \tag{2.42}$$

This intrinsic symmetry is spontaneously broken above threshold, a random value of the phase of the signal (and hence idler) being selected at each realization of the experiment.

We can thus see the onset of OPO as a phase transition in out-of-equilibrium conditions, signaling the spontaneous macroscopic occupation of the signal and idler states. Below threshold, the incoherent signal and idler emission starts being stimulated and then becomes coherent once the threshold is crossed. These coherence properties were studied both experimentally [117] as well as theoretically, by means of quantum Monte Carlo methods [145]. The order parameter of the transition is the matter polarization, the analog of magnetization in the ferromagnetic phase transition. At the critical point, noise fluctuations are amplified and a macroscopic polarization is spontaneously created.

The phase transition can be first or second order, depending on the pump parameters - both behaviors have been observed in experiments [16, 146, 147]. In the optical limiter case detailed above, both pump and signal are continuous functions of the incident laser power, and the transition is second order as the signal increases smoothly. In the pattern formation language, one clasifies the associated bifurcation as being of the *supercritical Hopf* type. If one considers the bistable pump regime of the right panel of Fig. 2.3 however, things get more complicated, as the bifurcation can now be of the *subcritical Hopf* type and hence the associated OPO initiates discontinuously [135].

It is relatively well known that in an infinite uniform two-dimensional equilibrium system, thermal fluctuations at any strictly nonzero temperature are strong enough to destroy the fully ordered BEC state. The associated phase transition in that case is instead described by the so-called Berezinskii-Kosterlitz-Thouless (BKT) theory, and is driven by interactions as opposed to being a purely statistical phenomenon. As the polariton system is out of equilibrium (and in practice no experimental system is truly infinite anyway), the exact nature of the OPO transition in this case has not yet been fully elucidated, although it seems that BKT-like physics has been both predicted [148] and observed [149] under incoherent pumping.

The breaking of the $U(1)$ symmetry in an atomic gas below the BEC critical point is related to the appearance of a soft Goldstone mode in the form of zero sound. Similar physics arises below the Curie temperature in a ferromagnet, where the magnon excitations (spin waves) are the corresponding Goldstone

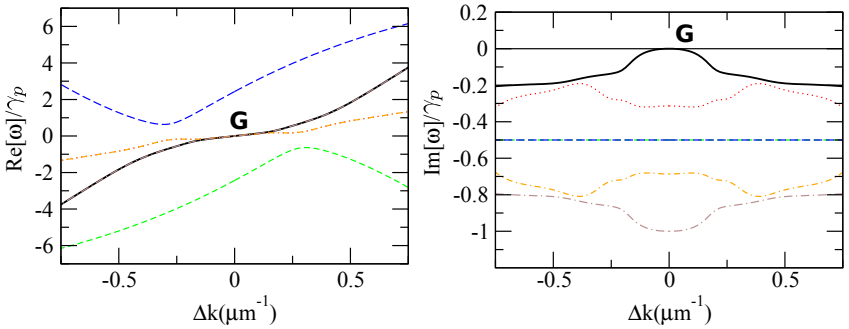

Figure 2.7: Real (left) and imaginary (right) parts of the Bogoliubov spectrum of collective excitations on top of the OPO stationary state as a function of $\Delta k = k - k_{s,p,i}$. The chosen pump intensity is marked with a dotted line in Fig. 2.6. The breaking of the $U(1)$ symmetry corresponding to the simultaneous phase rotation of the signal and idler is manifest in the presence of the Goldstone mode **G** (solid heavy curve). From Ref. [29].

bosons due to the spontaneous breaking of the initial rotational symmetry. Since the resonantly pumped polariton system above threshold spontaneously breaks a $U(1)$ symmetry, Goldtone's theorem predicts a massless mode corresponding in this case to a spatial twist of the signal-idler phases. Indeed, such a mode has been identified in Ref. [29] by calculating the quasiparticle excitation spectrum on top of the three-state OPO anzatz Eq. (2.41). The Bogoliubov spectrum in question is shown in Fig. 2.7, and the Goldstone mode represented by the solid heavy line labeled "G". Note that both the real and imaginary parts of the frequency of this gapless mode tend to zero in the long wavelength limit $\Delta k \to 0$. Close to this point, the real part has a non-zero slope due to the finite wavevector of the injected pump polaritons, while the imaginary part has a parabolic shape. This means that, as opposed to the BEC case, a localized perturbation in the OPO regime does not freely propagate as a sound wave. Instead, one should observe a diffusive-like behaviour, where the localized signal-idler phase perturbation decays and is then dragged along by the flow of the pump. Another important difference compared to the BEC spectrum is the absence of a singularity of the Goldstone branch around the $\Delta k = 0$ point.

Further insight into OPO physics for realistic experimental conditions can be gained by numerically solving the full 2-component GP equation (2.33) for the coupled exciton and cavity photon fields, as first done in Ref. [150]. A similar approach, reviewed in detail in Ref. [128], will be employed in Chapter 4, where we study multicomponent superfluidity in the OPO regime. Using a continuous wave pump with a top-hat profile, one injects polaritons at a specific wavevector, close to the inflection point of the LP dispersion. Above a certain threshold pump power, random numerical noise starts getting amplified and the OPO instability

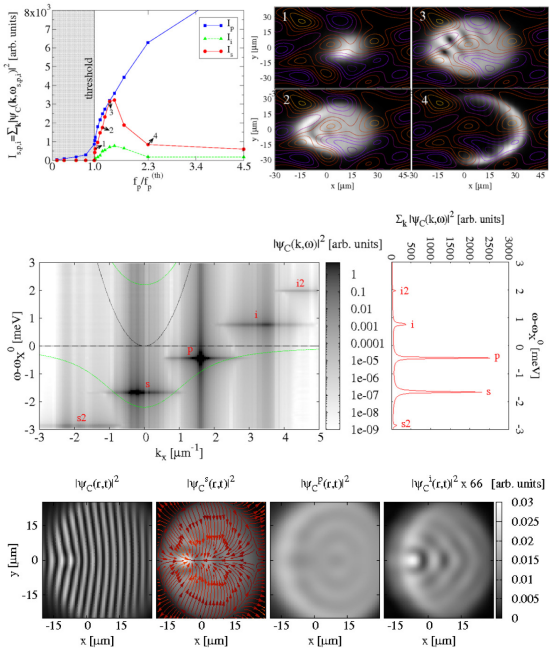

Figure 2.8: *Top panels:* Integrated photon emission intensities for the signal s (red dots), pump p (blue squares) and idler i (green triangles) as a function of the renormalized pump intensity (left) and real-space signal emission corresponding to positions 1-4, including random photonic disorder, shown as contour lines (right). Note the OPO phase transition is a gradual one, with the signal first switching on in the center, increasing to maximum size and finally switching off for large pump intensities. *Middle panels:* Photonic component of the OPO spectrum (log scale) as a function of energy and momentum (left) and integrated in momentum (right). Note that the emission is δ-like in energy. *Bottom panels:* Full photonic emission (left) and filtered real-space emission of signal, pump and idler (last 3 panels). Note the vertical interference fringes caused by the coherent superposition of the 3 states. The arrows in the second panel indicate the complex currents due to finite size effects. From Ref. [128].

sets in, populating the three states. After the system reaches a steady state, one can obtain the time evolution of the photon and exciton fields ψ_C and ψ_X both in real and momentum space. Since experiments measure the photonic component of the polariton field, that is what is plotted in Fig. 2.8. Filtering in a narrow cone in momentum (or equivalently, in energy), one can obtain separately the emission of the signal, pump and idler states, while the energy-momentum spectrum can be calculated as the discrete Fourier transform of the total photonic wavefunction

recorded at equally spaced time-intervals.

Inspecting Fig. 2.8, we see that the threshold is a continuous one in this case, with the OPO first switching on in a narrow region in the center of the system and then extending to the size of the whole pump spot before finally surviving only on its edge when pumping is increased even further. Interestingly, the OPO transition is signaled by the appearance of a moving striped pattern in the polariton density (see bottom left panel), spontaneously breaking the translational symmetry of the system. This pattern is caused by the interference of the coherent emission of the three states, and is similar to the Rayleigh-Bénard instability in the field of fluid dynamics. The threshold point in the OPO case is where the stimulated scattering rate exceeds the losses, while the Bénard cells form when the temperature gradient (playing the role of pumping) exceeds the viscosity (dissipation). In these simulations, the pump (and hence also signal and idler) wavevectors are oriented along the $\hat{x}$ direction, $\boldsymbol{k}_p = (\boldsymbol{k}_p, 0)$, so the fringes appear along the $\hat{y}$ axis. They are however usually not visible in experiments, due to the time integration of the photonic emission in most experimental setups. Seen in this new light, the OPO phase transition has an associated Goldstone mode that would correspond to a rigid translation of the spatial stripe pattern.

The photonic component of the OPO spectrum is shown in the middle pannel of Fig. 2.8. Integrating the spectrum over all momenta, one sees that, as a result of being in the steady state, the emission is δ-like in energy, while it is broadened in momentum due to the finite size of the pump. The satellite states, equally spaced in energy and less populated, are also visible in the middle left panel. They are due to secondary scattering processes, from the signal/idler into the pump and secondary-signal/secondary-idler, and so on.

Finally, the filtered emission from the signal, pump and idler states is shown in the lower panels of Fig. 2.8. Since we are in the steady state, the density profiles are time-independent and the idler emission is less intense due to the smaller radiative decay of polaritons at large momenta. One important difference from cold atomic gases in the BEC regime is the presence of nonvanishing currents, which can flow across the microcavity even in the ground state in a polariton system. These currents can be seen in the second panel for the signal state, and are due the complex interaction between nonlinearities, dissipation and parametric gain. Note that we are not refering here to the uniform flow caused by the signal being at finite momentum $\boldsymbol{k}_s$, as in fact this dominant current is substracted from the plot.

While still on the topic of persistent currents, we can make the connection to Sec. 1.5, and discuss superfluid-related phenomena in the OPO regime. A prime example of this is the stability of quantized vortices, reported by Sanvitto and coworkers in Ref. [31]. They used a pulsed, narrow probe beam in a Gauss-Laguerre state in order to imprint a finite angular momentum on the OPO condensate previously created by means of a wide pump spot. In a similar fashion to the rotating BEC experiments performed with ultracold gases, the system responded by forming a quantized vortex, which eventually drifted out of

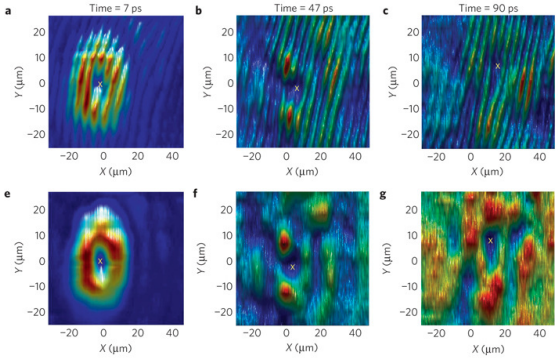

Figure 2.9: Snapshots of the time evolution of the phase (upper row) and the density (bottom row) of an OPO polariton condensate triggered by a pulsed probe carrying a $m = 1$ vortex. From Ref. [31].

the condensate, due to the simply-connected geometry (see Fig. 2.9). The vortex was visible in both the signal and idler state, and its lifetime was much longer than the average polariton lifetime. In a similar direction, Ref. [151] presented a theoretical study predicting the formation of spontaneous quantized vortices in the OPO regime, provided the pump spot is spatially narrow. These vortices were shown to drift to their stable equilibrium positions, caried by the nontrivial OPO currents discussed in the previous paragraph. Further work by Tosi et al. [152] investigated the appearance and dynamics of vortex-antivortex pairs created by a pulsed probe, much narrower than the pump spot. It was shown that, while both vortices and antivortices form along the edge of the probe laser, they form at different relative positions, as determined by the steady-state currents. We will deepen our investigation of OPO superfluidity in Chapter 4, where we look at the flow of the signal, pump and idler states against a small defect. Finally, departing somewhat from the OPO regime, it was shown in Ref. [153] that, despite not strictly obeying the Landau criterion, the superfluid density of incoherently pumped polaritons need not vanish. However, due to their nonequilibrium nature, the normal fraction would remain finite even at zero temperature. Last but not least, the same publication proposes using artificial gauge fields (generated by applying a real magnetic field in an anti-Helmholtz configuration) for measuring the superfluid and normal components of the system.

Part II

Applications

Chapter 3

Drag in a coherently-driven polariton fluid

In a conservative quantum liquid flowing past a small defect, the Landau criterion for superfluidity (presented in Sec. 1.4) links the onset of dissipation at a critical fluid velocity with the shape of the fluid collective excitation spectrum [50]. In particular, for weakly interacting Bose gases, the dispersion of the low-energy excitation modes being linear implies that the critical velocity for superflow coincides with the speed of sound c_s. Clearly, this is strictly correct only for vanishingly small perturbations [59], while for a defect with finite size and strength, the critical velocity can be smaller than c_s [60, 75], due to vortex creation by the macroscopic defect.

However, even for perturbatively weak defects, in out-of-equilibrium systems, where the spectrum of excitations is complex, the validity of the Landau criterion has to be questioned [28, 148, 154]. In the particular case of coherently driven polaritons in the pump-only configuration, it has been predicted [155, 156], and later observed [26], that scattering is suppressed at either strong enough pump powers or small enough flow velocities (see Fig. 3.1). Yet, on closer scrutiny, it has been shown that, despite the apparent validity of the Landau criterion, the system always experiences a residual drag force, even in the limit of asymptotically large densities [154] or small velocities. This result has been proven by numerically solving the Gross-Pitaevskii equation describing the resonantly-driven polariton system in presence of a non-perturbative extended defect. Here, the drag force exerted by the defect on the fluid has been shown to display a smooth crossover from the subsonic to the supersonic regime, similar to what it has been found in the case of non-resonantly pumped polaritons [28]. In this Chapter, we find an even richer phenomenology for the dependence of the drag force on the fluid velocity and two different kinds of crossovers from the sub- to the supercritical regime. Furthermore, we show that the origin of the residual drag force, which, in agreement with Ref. [154], lies in the polariton lifetime only, can be demonstrated even within a linear response approximation.

More specifically, we apply the linear response theory described in Sec. 1.3 for the case of an equilibrium condensate and extended here to a driven-dissipative

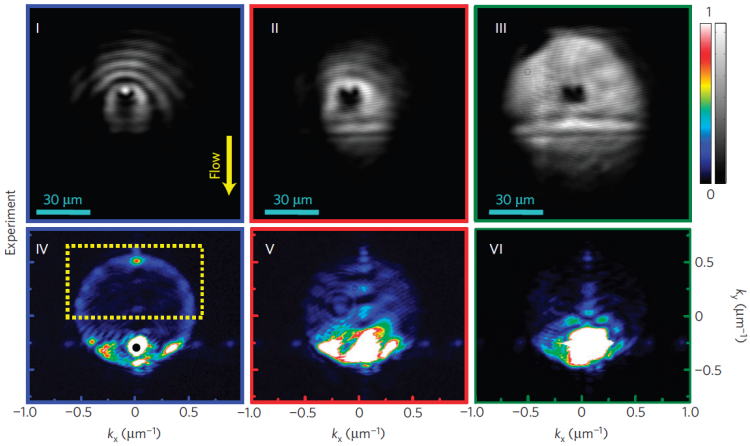

Figure 3.1: Experimental images of the real- (top row) and momentum- (bottom row) space polariton density extracted from the near/far-field light emitted from the cavity. The different columns correspond to increasing values of the polariton density, from left to right. For the highest density, polariton superfluidity is apparent as a suppression of the real-space modulation (panel III) accompanied by the collapse of the Rayleigh scattering ring (panel VI). From Ref. [26].

fluid in order to analytically evaluate the drag force exerted by the coherently driven polariton fluid in the pump-only configuration on a point-like defect. To simplify the formalism, we restrict our analysis to the case of resonant pumping close to the bottom of the lower polariton dispersion, where the dispersion is quadratic. Here, the properties of the collective excitation spectrum have been shown to be uniquely determined by three parameters only [156]: the fluid velocity v_p, the interaction-renormalised pump detuning Δ_p, and the polariton lifetime γ. In particular, the sign of the detuning Δ_p determines three qualitatively different types of spectra: linear for $\Delta_p = 0$, diffusive-like for $\Delta_p > 0$, and gapped for $\Delta_p < 0$.

For both cases of linear and diffusive spectra, we find a qualitatively similar behaviour of the drag force as a function of the fluid velocity v_p: In particular, the drag displays a crossover from a subsonic or superfluid regime — characterised by the absence of quasiparticle excitations — to a supersonic regime — where Cherenkov-like waves, similar to those of Sec. 1.4, are generated by the defect and propagate into the fluid. The crossover becomes sharper for increasing polariton lifetimes $1/\gamma$ and displays the typical threshold behaviour for $\gamma \to 0$ with a critical velocity given by the speed of sound of the linear regime, $v^c = c_s$, exactly as for weakly interacting equilibrium superfluids (in the case of perturbatively weak defects). This behaviour is similar to the one predicted for polariton superfluids excited non-resonantly [28], where the spectrum in that case is diffusive-like.

However, for gapped spectra at $\Delta_p < 0$, we find that the critical velocity governing the drag crossover exceeds the speed of sound, $v^c > c_s$, and we determine an analytical expression of v^c as a function of the detuning Δ_p. Furthermore, for $\gamma \to 0$, the drag has a threshold-like behaviour qualitatively different from the one of weakly interacting equilibrium superfluids, with the drag jumping discontinuously from zero to a finite value at $v_p = v^c$.

We evaluate the drag as a function of the polariton lifetime γ and find for all three cases that: In the supercritical regime, $v_p > v^c$, the lifetime tends to suppress the propagation of the Cherenkov waves away from the defect and therefore to suppress the drag. Instead, well in the subcritical regime, $v_p \ll v^c$, we find that the residual drag goes linearly to zero with the polariton lifetime γ, in agreement to what was found in Ref. [154], by making use of a non-perturbative numerical analysis for a finite size defect. Similar to Ref. [154], here, we do also find that the residual drag in the subcritical regime can be explained in terms of an asymmetric perturbation induced in the fluid by the defect in the direction of the fluid velocity.

This Chapter is structured as follows: In Sec. 3.1 we briefly review the linear approximation scheme and extend it to the case of a resonantly pumped polariton fluid. We classify the three types of collective excitation spectra in the simplified case of excitation close to the bottom of the LP dispersion in Sec. 3.1.1. In Sec. 3.2 we derive the drag force and characterise the crossover from the subsonic to the supersonic regime in the three cases of zero, positive and negative detuning. In this section, we also evaluate the drag as a function of the polariton lifetime, interpreting therefore the results of Ref. [154]. Brief conclusions are drawn is Sec. 3.3.

3.1 Linear response

As explained in Chapter 2, the description of cavity polaritons resonantly excited by an external laser is usually formulated in terms of a classical non-linear Schrödinger equation (or Gross-Pitaevskii equation) for the LP field $\psi_{LP}(\boldsymbol{r}, t)$ (see Eq. (2.32)):

$$i\partial_t \psi_{LP} = [\omega_{LP}(-i\nabla) - i\gamma/2 + V_d(\boldsymbol{r}) + g_X|\psi_{LP}|^2]\psi_{LP} + \mathcal{F}(\boldsymbol{r}, t) \,. \tag{3.1}$$

The LP dispersion is expressed in terms of the photon $\omega_C(\boldsymbol{k}) = \omega_C(0) + \frac{\boldsymbol{k}^2}{2m_C}$ and exciton $\omega_X(0)$ energies, the photon mass m_C, and the Rabi splitting Ω_R (see Eq. (2.15)):

$$\omega_{LP}(\boldsymbol{k}) = \frac{1}{2}\left[\omega_C(\boldsymbol{k}) + \omega_X(0)\right] - \frac{1}{2}\sqrt{\left[\omega_C(\boldsymbol{k}) - \omega_X(0)\right]^2 + 4\Omega_R^2} \,. \tag{3.2}$$

Because polaritons continuously decay at a rate γ (see Sec. 2.5), the cavity is replenished by a continuous wave resonant pump $\mathcal{F}(\boldsymbol{r}, t)$ at a wavevector $\boldsymbol{k}_p$ (we

will later assume $\boldsymbol{k}_p$ directed along the x-direction, $\boldsymbol{k}_p = (k_p, 0)$) and frequency ω_p (see Eq. (2.23)):

$$\mathcal{F}(\boldsymbol{r}, t) = f_p e^{i(\boldsymbol{k}_p \cdot \boldsymbol{r} - \omega_p t)} \ . \tag{3.3}$$

Note that, as discussed in Secs. 2.4–2.7, Eq. (3.1) is a simplified description of the polariton system. It implies that the interaction nonlinearities are small enough not to mix the lower and upper polariton branches and that we pump far from the UP dispersion. Moreover, starting from a formulation in terms of coupled exciton and photon fields, the polariton lifetime would be momentum dependent and, similarly, the polariton-polariton interaction strength g_X is not contact-like as instead assumed in Eq. (3.1). However, as shown in Appendix 3.A, these simplifications do not affect our results qualitatively, rather, they allow us to write them in terms of simpler expressions. Furthermore, we have checked that, whenever the system is excited near the bottom of the lower polariton dispersion, the results for the drag force reported in Sec. 3.2 coincide with the ones obtained using the photon-exciton coupled field description Eq. (2.33) introduced in Chapter 2.

The potential $V_d(\boldsymbol{r})$ in Eq. (3.2) describes a defect, which can be either naturally present in the cavity mirror [26] or it can be created by an additional laser [157]. Later on, we will assume the defect to be point-like $V_d(\boldsymbol{r}) = g_V \delta(\boldsymbol{r})$ and weak, so that we can apply the linear response approximation [59]. As detailed in Sec. 1.3, one divides the response of the LP field in a mean-field component ψ_p corresponding to the case when the perturbing potential is absent, and a fluctuation part $\delta\psi(\boldsymbol{r}, t)$ reflecting the linear response of the system to the perturbing potential (see Eq. (1.12)):

$$\psi_{LP}(\boldsymbol{r}, t) = e^{-i\omega_p t} \left[e^{i\boldsymbol{k}_p \cdot \boldsymbol{r}} \psi_p + \delta\psi(\boldsymbol{r}, t) \right] \ . \tag{3.4}$$

By substituting (3.4) into (3.1), we obtain a mean-field equation and by retaining only the linear terms in the fluctuation field and the defect potential, the following first order equation in $\delta\psi(\boldsymbol{r}, t)$ (the equivalent of Eq. (1.14)):

$$i\partial_t \begin{pmatrix} \delta\psi \\ \delta\psi^* \end{pmatrix} = \hat{\mathcal{L}} \begin{pmatrix} \delta\psi \\ \delta\psi^* \end{pmatrix} + V_d(\boldsymbol{r}) \begin{pmatrix} \psi_p e^{i\boldsymbol{k}_p \cdot \boldsymbol{r}} \\ -\psi_p^\star e^{-i\boldsymbol{k}_p \cdot \boldsymbol{r}} \end{pmatrix} \ , \tag{3.5}$$

where the operator $\hat{\mathcal{L}}$ is given by (compare to Eq. (1.29) for the atomic case):

$$\hat{\mathcal{L}} = \begin{pmatrix} \widetilde{\omega_{LP}}(-i\nabla) - i\gamma/2 & g_X \psi_p^2 e^{2i\boldsymbol{k}_p \cdot \boldsymbol{r}} \\ -g_X \psi_p^{\star 2} e^{-2i\boldsymbol{k}_p \cdot \boldsymbol{r}} & -\widetilde{\omega_{LP}}(-i\nabla) - i\gamma/2 \end{pmatrix} \ , \tag{3.6}$$

with $\widetilde{\omega_{LP}} = \omega_{LP} - \omega_p + 2g_X|\psi_p|^2$. We solved the complex cubic mean-field equation (2.36) for ψ_p in Sec. 2.8. Here, we want to study the response of the system to the presence of the defect and how different behaviours of the onset of dissipation can be described in terms of the different excitation spectra one can get for polaritons resonantly pumped close to the bottom of the LP dispersion.

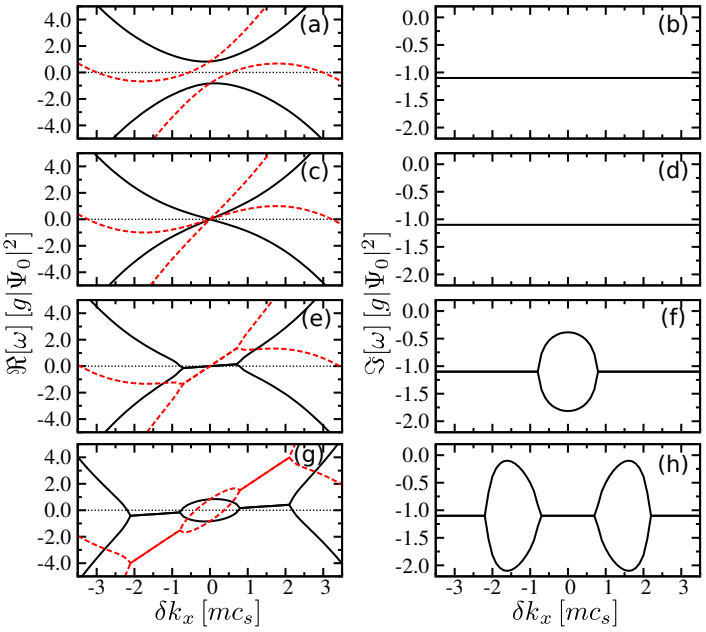

Figure 3.2: Collective excitation spectra for the subsonic (thick solid [black] line at $v_p = 0.2c_s$, with $c_s = \sqrt{g_X|\psi_p|^2/m_{\rm LP}}$) and supersonic (dashed [red] line at $v_p = 1.9c_s$) regimes and for an interaction-renormalised pump detuning $\Delta_p = -0.3g_X|\psi_p|^2$ (a, b), $\Delta_p = 0$ (c, d), $\Delta_p = 0.3g_X|\psi_p|^2$ (e, f) and $\Delta_p = 2.3g_X|\psi_p|^2$ (g, h). Real parts of the spectra are plotted in the left panels and the corresponding imaginary parts in the right panels for $\gamma = 2.2g_X|\psi_p|^2$ — note that in our description the spectrum imaginary parts do not depend on the fluid velocity v_p.

3.1.1 Spectrum of collective excitations

The spectrum of the collective excitations can be obtained by diagonalising the operator $\hat{\mathcal{L}}$ in the momentum space representation, following the approach of Sec. 1.4 (see Eq. (1.34))

$$\mathcal{L}_{\boldsymbol{k},\boldsymbol{k}_p} = \begin{pmatrix} \widetilde{\omega_{LP}}(\delta\boldsymbol{k}+\boldsymbol{k}_p) - i\gamma/2 & g_X\psi_p^2 \\ -g_X\psi_p^{\star 2} & -\widetilde{\omega_{LP}}(\delta\boldsymbol{k}-\boldsymbol{k}_p) - i\gamma/2 \end{pmatrix} , \tag{3.7}$$

where, $\delta\boldsymbol{k} = \boldsymbol{k} - \boldsymbol{k}_p$. The description of the spectrum simplifies in the case when the pumping is close to the bottom of the LP dispersion, that can be approximated as parabolic (see Eq. (2.22))

$$\omega_{LP}(\delta\boldsymbol{k} \pm \boldsymbol{k}_p) \simeq \omega_{LP}(0) + \frac{k_p^2}{2m_{\rm LP}} + \frac{\delta\boldsymbol{k}^2}{2m_{\rm LP}} \pm \delta\boldsymbol{k}\cdot\boldsymbol{v}_p \, , \tag{3.8}$$

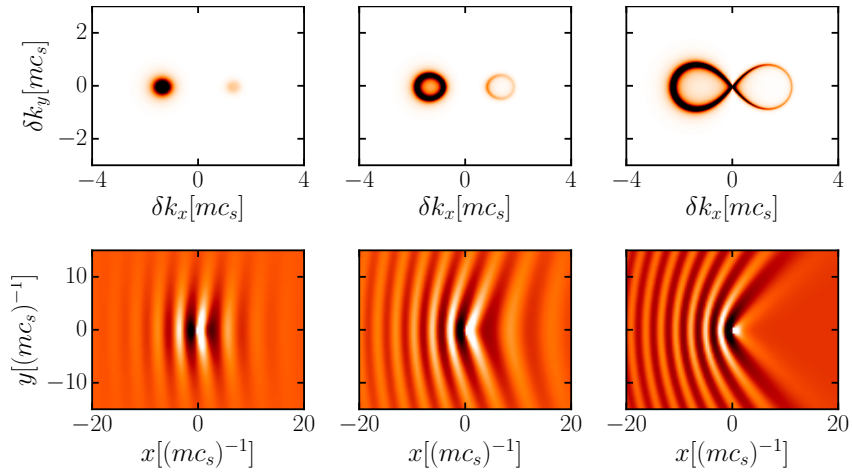

Figure 3.3: Momentum-space response (top row) $|\delta\psi_s\,(\boldsymbol{k}+\boldsymbol{k}_p)\,|^2$ (arb. units) and normalised real-space wavefunction (bottom row) $|\psi_{LP}(\boldsymbol{r})|^2/|\psi_p|^2$ corresponding to the nondiffusive spectra (a)–(d) in Fig. 3.2. System parameters: $v_p = 1.5c_s$, $\gamma = 0.06g_X|\psi_p|^2$, and Δ_p is $-0.35g_X|\psi_p|^2$ (left column), $-0.25g_X|\psi_p|^2$ (middle column) and 0 (right column).

where $\boldsymbol{v}_p = \boldsymbol{k}_p/m_{\mathrm{LP}}$ is the fluid velocity, and m_{LP} is the LP mass of Eq. (2.21). This simplification allows one to describe the complex spectrum in terms of three parameters only, namely the fluid velocity $\boldsymbol{v}_p$, the interaction-renormalised pump detuning (defined in Sec. 2.8)

$$\Delta_p = \omega_p - \left[\omega_{LP}(0) + \frac{k_p^2}{2m_{\mathrm{LP}}} + g_X|\psi_p|^2\right] \tag{3.9}$$

and the LP lifetime γ. One observation we can immediately make is that, unlike the atomic case, one will no longer have a sharp corner[1] in the spectrum at $\delta\boldsymbol{k} = 0$, as that feature depended on the equality (up to a sign) between the diagonal and off-diagonal elements of $\mathcal{L}$. The elementary excitation spectrum of coherently-driven polaritons reads (compare this to the spectrum given by Eq. (1.36)):

$$\omega_\pm(\boldsymbol{k}) = \delta\boldsymbol{k}\cdot\boldsymbol{v}_p - i\gamma/2 \pm \sqrt{\varepsilon(\delta\boldsymbol{k})\left[\varepsilon(\delta\boldsymbol{k}) + 2g_X|\psi_p|^2\right]}\,, \tag{3.10}$$

where $\varepsilon(\boldsymbol{k}) = \frac{k^2}{2m_{\mathrm{LP}}} - \Delta_p$. If energies are measured in units of the mean-field energy blue-shift $g_X|\psi_p|^2$ (we will use the notation $\Delta_p' = \Delta_p/g_X|\psi_p|^2$ and $\gamma' = \gamma/g_X|\psi_p|^2$), then the fluid velocity v_p is measured in units of the speed of sound

[1] Unless, of course, $\Delta_p = 0$.

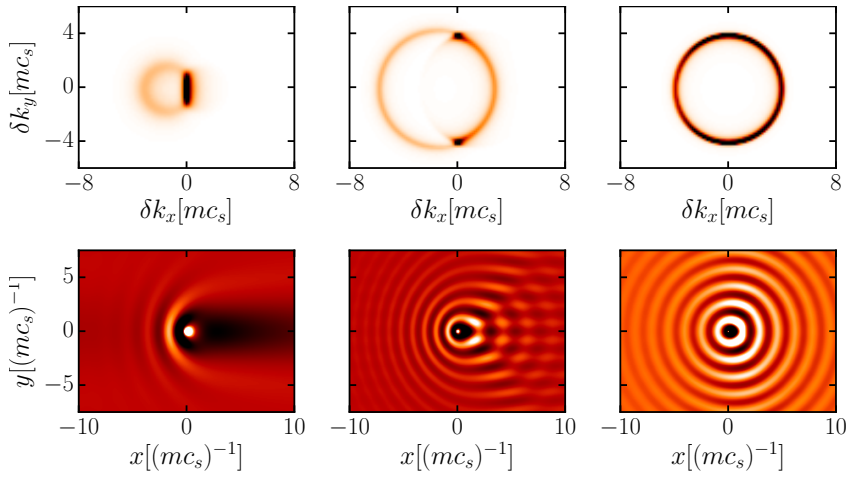

Figure 3.4: Momentum-space response (top row) $|\delta\psi_s\,(\boldsymbol{k}+\boldsymbol{k}_p)\,|^2$ (arb. units) and normalised real-space wavefunction (bottom row) $|\psi_{LP}(\boldsymbol{r})|^2/|\psi_p|^2$ corresponding to the diffusive spectra (e)–(h) in Fig. 3.2. Polariton lifetime $\gamma = 2.2 g_X|\psi_p|^2$, and $\Delta_p = g_X|\psi_p|^2$, $v_p = 1.5c_s$ (left column); $\Delta_p = 9g_X|\psi_p|^2$, $v_p = 1.5c_s$ (middle column) and $\Delta_p = 9g_X|\psi_p|^2$, $v_p = 0.07c_s$ (right column).

$c_s = \sqrt{g_X|\psi_p|^2/m_{\rm LP}}$. In order to make connection with the current experiments, note that, for blue-shifts in the range $g_X|\psi_p|^2 \simeq 0.1-1$ meV, typical values of the speed of sound c_s are $0.8-2.7\times10^6$ m/s. Similarly, for common values of the LP mass, the range in momenta in Fig. 3.2 comes of the order of $\delta k_x \simeq 0.2-0.8\ \mu\mathrm{m}^{-1}$.

The spectrum (3.10) can be classified according to the sign of the interaction-renormalised pump detuning Δ_p [155, 156] — see Fig. 3.2. For $\Delta_p < 0$ (panels [a,b]), the real part of the spectrum lacks the sonic behaviour at small $\delta\boldsymbol{k}$, and shows a *gap* that increases with $|\Delta_p|$, while the imaginary part is determined by the polariton lifetime γ only. If one applies the Landau criterion for the real part of the spectrum only, then one finds a critical velocity

$$\frac{v^c}{c_s} = \sqrt{1+|\Delta_p'|+\sqrt{|\Delta_p'|(|\Delta_p'|+2)}} > 1\,, \tag{3.11}$$

always larger than the speed of sound for $\Delta_p < 0$. If the fluid velocity is sub-critical, $v_p < v^c$ (see the [black] solid lines in Fig. 3.2(a)), then no quasiparticles can be excited and thus, for infinitely living polaritons $\gamma \to 0$, the fluid would experience no drag when scattering against the defect. For the case of $v_p = v^c$, the $\Re[\omega_+(\boldsymbol{k})]$ branch touches the $\omega = 0$ plane in one point (see left column of Fig. 3.3), resulting in a localized perturbation around the defect, with an additional stripe pattern of wavevector $m_{\rm LP}v^c$, caused by the interference of the pump with the momentum of the scattered state. For supercritical velocities in-

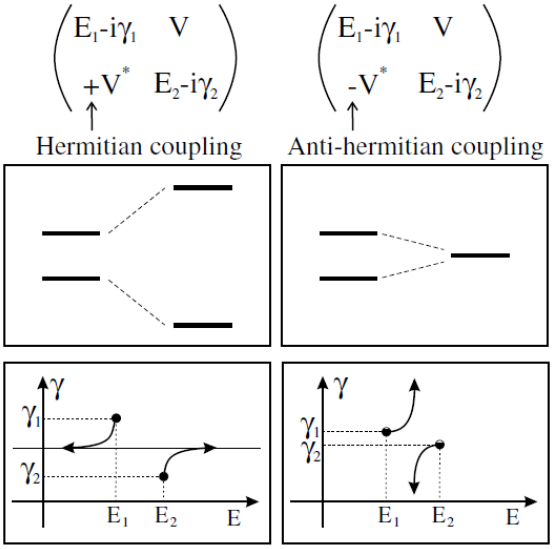

Figure 3.5: Hermitian (left column) and anti-Hermitian (right column) coupling between two damped oscillators of energies E_1, E_2, decay rates γ_1, γ_2 and interaction energy V. Top row shows the coupling matrices, while middle (bottom) row shows the evolution of the real (complex) eigenvalues, with increasing $|V|$. From Ref. [12].

stead, $v_p > v^c$ see the [red] dashed lines in Fig. 3.2(a), one expects dissipation in the form of radiation of Cherenkov-like waves from the defect into the fluid. In the supercritical regime, the set of wavevectors $\boldsymbol{k}$ for which $\Re[\omega_+(\boldsymbol{k})] = 0$ form a closed curve in $\boldsymbol{k}$-space with no singularity of the derivative (see middle column of Fig. 3.3). As explained in the geometrical model presented in Sec. 1.4, this means the radiation can be emitted in all possible directions around the defect. This, as we will see in the next section, will imply that the drag force for $\gamma \to 0$ goes abruptly, rather than continuously, from zero at $v_p < v^c$ to a finite value at $v_p \geq v^c$.

The spectrum gap closes to zero in the resonant situation at $\Delta_p = 0$, when the two branches $\omega_\pm(\boldsymbol{k})$ touch at $\delta\boldsymbol{k} = 0$ (panels [c,d] of Fig. 3.2). Here, the real part of the spectrum displays the standard *sonic dispersion* at small wavevectors (as for the weakly interacting bosonic gases of Chapter 1) with a slope given by $c_s \pm v_p$. The imaginary part, as in the previous case, is constant and equal to $-\gamma/2$. It is clear therefore that in this case, when $\gamma \to 0$, one recovers the equilibrium results valid for weakly interacting gases [56, 59], where the critical velocity for superfluidity equals the speed of sound, $v^c = c_s$, and the drag displays a threshold-like behaviour. Here, in the supersonic regime $v_p > v^c$, the closed

curve $\Re[\omega_+(\boldsymbol{k})] = 0$ has instead a singularity, resulting in the standard Mach cone of aperture θ, $\sin\theta = c_s/v_p$, inside which radiation from the defect cannot be emitted [56] (see right column of Fig. 3.3, as well as Fig. 1.2 of Sec. 1.4).

For $\Delta_p > 0$, the real parts of the two Bogoliubov branches cross and stick together, giving rise to flat regions near the crossing points. This is due to level attraction caused by the anti-Hermitian coupling of Eq. (3.7), and is accompanied by a splitting of the imaginary parts, as illustrated in Fig. 3.5. We further distinguish two separate cases, $0 < \Delta_p \leq 2$ and $\Delta_p > 2$. In the first case (panels [e,f]), there is only one flat region in momentum-space, and the intensity of the Rayleigh scattering is amplified on a segment situated at $\delta k_x = 0$ and oriented parallel to the y axis, as shown in the left column of Fig. 3.4. A consequence of this (parametric) amplification is the long shadow seen in the real-space image [156]. As the imaginary part only has one peak (corresponding to the pump), this is the precursor of the Kerr single-mode instability described in Sec. 2.8. The second case (panels [g,h]) has a different momentum-space topology, with two flat regions, producing two distinct peaks in the imaginary part. As soon as these become positive, one enters the regime of parametric oscillation (see Sec. 2.9), with the signal and idler momenta situated at the two maxima. The corresponding far-field image plotted in the middle column of Fig. 3.4 shows two pronounced peaks on the line passing through $\delta k_x = 0$, the interference of which results in a near-field "zebra-like" pattern [156]. For very small fluid velocities (see right column of Fig. 3.4), the two Bogoliubov branches cross on a ring of wavevectors, giving rise to cylindrical wavefronts [158]. We note that spectra [e]–[h] have no correspondence in equilibrium systems, because a finite polariton lifetime γ is needed in order to insure stability, $\Im[\omega_\pm(\boldsymbol{k})] < 0$. Following the literature [2], we refer to these spectra as *diffusive-like*. We also note that, for these spectra, even if considering only the real part of the collective excitation spectrum, as soon as the fluid is in motion, dissipation in the form of waves is possible. However, we will see that, similar to the case of non-resonantly pumped polaritons [28], when decreasing γ (and accordingly Δ_p in order to have stable solutions), this situation continuously connects to the case where a threshold-like behaviour with $v^c = c_s$ was found.

We will see in the next section how these different spectra imply only two qualitatively different types of crossover of the drag force as a function of the fluid velocity, for either $\Delta_p < 0$ or $\Delta_p \geq 0$ pump detunings.

3.2 Drag force

The steady state response of the system to a static and weak defect can be evaluated starting from Eq. (3.5):

$$\begin{pmatrix} \delta\psi_s(\boldsymbol{r}) \\ \delta\psi_s^*(\boldsymbol{r}) \end{pmatrix} = \hat{\mathcal{L}}^{-1} \begin{pmatrix} V_d(\boldsymbol{r}) e^{i\boldsymbol{k}_p\cdot\boldsymbol{r}} \psi_p \\ -V_d(\boldsymbol{r}) e^{-i\boldsymbol{k}_p\cdot\boldsymbol{r}} \psi_p^\star \end{pmatrix} .$$

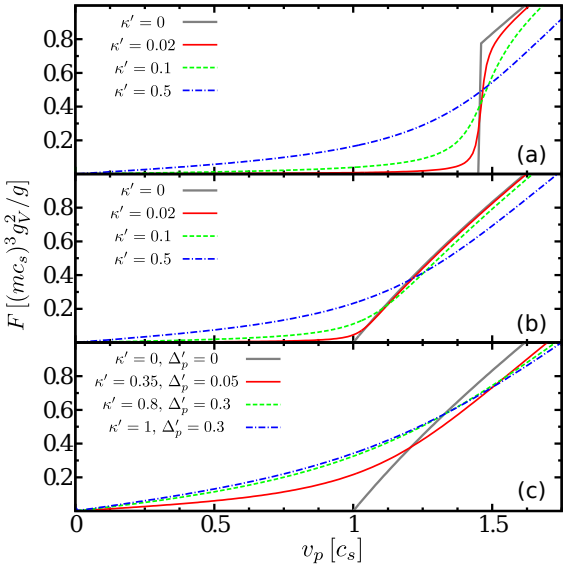

Figure 3.6: Drag force F_d as a function of the fluid velocity v_p for different values of the pump detuning Δ_p: $\Delta_p = -0.3 g_X |\psi_p|^2$ (a), $\Delta_p = 0$ (b), and $\Delta_p > 0$ (c), and for different values of the polariton lifetime — here, we use the notation $\gamma' = \gamma/g_X|\psi_p|^2$ and $\Delta'_p = \Delta/g_X|\psi_p|^2$.

For a point-like defect, this can be written in momentum space as:

$$\delta\psi_s(\boldsymbol{k}+\boldsymbol{k}_p) = \frac{-g_V\psi_p(\varepsilon(\boldsymbol{k}) - \boldsymbol{k}\cdot\boldsymbol{v}_p + i\gamma/2)}{\varepsilon(\boldsymbol{k})[\varepsilon(\boldsymbol{k}) + 2g_X|\psi_p|^2] - (\boldsymbol{k}\cdot\boldsymbol{v}_p - i\gamma/2)^2} ,$$

while the other component $\delta\psi_s^*(\boldsymbol{k}_p - \boldsymbol{k})$ can be obtained by complex conjugation and by substituting $\boldsymbol{k} \to -\boldsymbol{k}$. The drag force exerted by the defect on the fluid is given by the expectation value of the operator $-\boldsymbol{\nabla} V_d(\boldsymbol{r})$ over the condensate wavefunction [159]:

$$\boldsymbol{F}_d = -\int d\boldsymbol{r} |\psi_{LP}(\boldsymbol{r},t)|^2 \boldsymbol{\nabla} V_d(\boldsymbol{r}) , \tag{3.12}$$

This definition is justified for conservative systems in Appendix 1.A, using the momentum-flux tensor. In the steady state linear response regime, we obtain:

$$\begin{aligned}\boldsymbol{F}_d &= g_V \int \frac{d\boldsymbol{k}}{(2\pi)^2} i\boldsymbol{k} \left[\psi_p^* \delta\psi_s(\boldsymbol{k}+\boldsymbol{k}_p) + \psi_p \delta\psi_s^*(\boldsymbol{k}_p - \boldsymbol{k})\right] \\ &= 2g_V^2 |\psi_p|^2 \int \frac{d\boldsymbol{k}}{(2\pi)^2} \frac{i\boldsymbol{k}\varepsilon(\boldsymbol{k})}{\omega_+(\boldsymbol{k})\omega_-(\boldsymbol{k})} .\end{aligned} \tag{3.13}$$

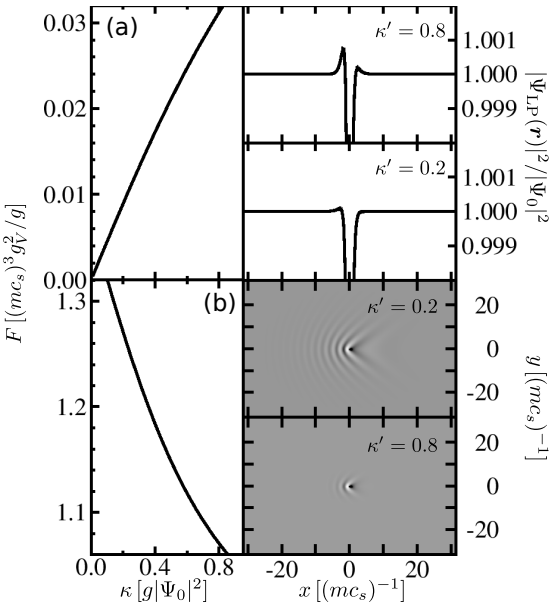

Figure 3.7: Drag force F_d as a function of the inverse polariton lifetime $\gamma' = \gamma/(g_X|\psi_p|^2)$ in the (a) subcritical regime ($v_p = 0.2c_s$) and (b) supercritical regime ($v_p = 1.9c_s$). In both cases we have fixed $\Delta_p = -0.3g_X|\psi_p|^2$ ($v^c \simeq 1.46c_s$) but these results are qualitatively similar for any other value of the pump detuning. We plot in the right panels the normalised real-space wavefunction $|\psi_{LP}(\boldsymbol{r})|^2/|\psi_p|^2$ for two specific values of $\gamma' = 0.4$ and $\gamma' = 1.6$.

The drag is clearly oriented along the fluid velocity $\boldsymbol{v}_p$, i.e., $\boldsymbol{F}_d = F_d\hat{\boldsymbol{v}}_p$. If $\gamma \to 0$, then the integral in Eq. (3.13) is finite only if poles exist when $\Re[\omega_\pm(\boldsymbol{k})] = 0$, i.e., when quasiparticles can be excited, in agreement with the Landau criterion. For finite polariton lifetimes, however, it is clear that the integral will always be different from zero for $v_p > 0$. We now analyse the behaviour of the drag force as a function of the fluid velocity for the three ($\Delta_p = 0$, $\Delta_p > 0$, and $\Delta_p < 0$) different spectra illustrated in the previous section.

For the *linear* spectrum, at $\Delta_p = 0$, in the equilibrium limit, $\gamma \to 0$, we recover for the drag the known result of weakly interacting Bose gases in two dimensions [59]:

$$\frac{F_d}{(m_{\rm LP}c_s)^3 g_V^2/g_X} = \frac{(v_p/c_s)^2 - 1}{v_p/c_s}\Theta(v_p - c_s)\ , \tag{3.14}$$

with a threshold-like behaviour at a critical fluid velocity equal to the speed of sound c_s. This limiting result is plotted as a bold gray line in the panels (b,c) of Fig. 3.6. For $\Delta_p = 0$ and finite lifetimes γ, we find a smooth crossover from the

subsonic to the supersonic regime, with the drag being closer to the equilibrium threshold behaviour for decreasing γ (see Fig. 3.6(b)). A finite lifetime tends to increase the value of the drag in the subsonic region $v_p \ll v^c$, giving place to a residual drag force, similar to what was found in the numerical simulations of Ref. [154] (see Fig. 3.8). Instead, in the supersonic region $v_p \gg v^c$, the finite lifetime tends to decrease the value of the drag.

In the case of *diffusive-like* spectra at $\Delta_p > 0$ the situation is qualitatively very similar to the resonant case (see Fig. 3.6(c)), with the difference that now, in order to have stable solutions, we can decrease the value of the lifetime only by decreasing accordingly also the value of the pump detuning Δ_p. The crossover for both $\Delta_p = 0$ and $\Delta_p > 0$ is also qualitatively very similar to the case of non-resonantly pumped polaritons [28], where the spectrum of excitation is diffusive-like. In Ref. [160], a similar approach was used to analytically derive the drag for nonresonantly pumped polaritons in 1D, finding a continuous crossover from a regime dominated by viscous drag (of Stokes type) to one dominated by wave resistance. Futhermore, the authors proved that it was not possible to separate the viscous and wave-resistance components of the drag. Shortly after the publication of Ref. [161] (on which this Chapter is based), Van Regemortel et al. [158] found that the parametric amplification mechanism described in Sec. 3.1.1 can increase the scattering of particles in the flow direction (for low condensate speeds), leading to a *negative drag force*, i.e. a force directed opposite to the flow direction. To see how this comes about, one can look at the right column of Fig. 3.4: the top panel shows that the average momentum of the scattered modes is in the positive δk_x direction. This, in turn, leads to a pileup of the fluid density behind the defect ($x > 0$), as can be seen in the bottom panel.

In the case of *gapped* spectra, the situation is, however, qualitatively different (see Fig. 3.6(a)). For infinitely living polaritons, $\gamma \to 0$, the drag force can also be evaluated analytically and its expression is similar to Eq. (3.14), but with a critical velocity larger than the speed of sound, the expression of which is given in Eq. (3.11):

$$\frac{F_d}{(m_{\rm LP} c_s)^3 g_V^2/g_X} = \frac{(v_p/c_s)^2 - 1}{v_p/c_s} \Theta(v_p - v^c) \, . \tag{3.15}$$

Therefore now the drag experiences a jump for $v_p = v^c$, rather than a continuous threshold as for the resonant case $\Delta_p = 0$. As already mentioned in the previous section, this discontinuous behaviour of the drag for the gapped spectra is connected to the fact that, as soon as quasiparticles can be excited by the defect at $v_p \geq v^c$, Cherenkov-like waves can be immediately emitted in all directions, rather than being restricted in a region outside the Mach cone as before. For $\Delta_p = 0$, the cone was gradually closing with increasing fluid velocity.

Both the increase of the value of the drag in the subcritical region as a function of the polariton lifetime and the decrease in the supercritical region, are behaviours common to all the types of spectra. We plot the drag force as a function of γ in Fig. 3.7, for two values of the fluid velocity v_p and a specific value

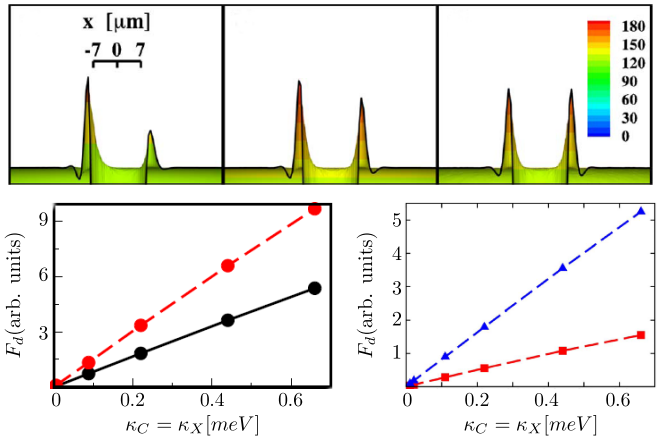

Figure 3.8: *Top row*: Photon density along $y = 0$, perturbed by a circular potential of radius 7 μm and height 110 meV (centered at the origin), in the subcritical regime. The pump momentum is $k_p = 1$ μm^{-1}, and the panels (from left to right) correspond to decreasing exciton (γ_X) and photon (γ_C) decay rates $\gamma_X = \gamma_C = 1.3$, 0.44 and 0.011 meV. *Bottom row*: Residual drag force as a function of decay rate. The left panel compares two different values of k_p, namely 0.7 (black solid line) and 1 μm^{-1} (red dashed line). The right panel shows two different potential heights, of -22 (blue dashed line) and -2.2 meV (red dashed line), with $k_p = 0.7$ μm^{-1}. In all plots, the pump is 0.44 meV blue-detuned above the bare LP branch $\omega_{LP}(\boldsymbol{k}_p)$. Adapted from Ref. [154].

of the pump detuning Δ_p, though we have checked that the following results are generic. For $v_p < v^c$, we find that the residual drag is a finite-lifetime effect only and, well below the critical velocity, the drag force goes linearly to zero for $\gamma \to 0$. This is in agreement with the results of Ref. [154], where the full GP equation for the coupled exciton and photon fields was solved numerically for a finite-size defect: see the bottom row of Fig. 3.8 for the numerical drag in the limit of asymptotically large densities.

In the resonant case $\Delta_p = 0$, the slope of the drag for $v_p \ll c_s$ can be evaluated analytically starting from the expression (3.13):

$$\frac{F_d}{(m_{\rm LP} c_s)^3 g_V^2 / g_X} \underset{\gamma \to 0}{\simeq} \frac{2c_s}{\pi v_p} \left(\frac{1}{\sqrt{1-(v_p/c_s)^2}} - 1 \right) \frac{\gamma}{2 g_X |\psi_p|^2} \, .$$

The residual drag in the subsonic regime is an effect of the broadening of the quasi-particles energies: Even when the spectrum real part does not allow any scattering against the defect (e.g., for $\Delta_p \leq 0$), the broadening produces some scattering close to the defect. This results in a perturbation of the fluid around the defect, asymmetric in the direction of the fluid velocity (see panel (a) of

Fig. 3.7), similar to what was obtained in Ref. [154] (see top row of Fig. 3.8). Instead, in the supersonic regime, the drag force is weaker in the non-equilibrium case with respect to the equilibrium one. This is caused by the finite lifetime tending to suppress the propagation of the Cherenkov waves away from the defect, as shown in panel (b) of Fig. 3.7.

3.3 Conclusions and discussion

To conclude, we have analysed the linear response to a weak defect of resonantly pumped polaritons in the pump-only state, and we have been able to determine two different kinds of threshold-like behaviours for the drag force as a function of the fluid velocity. In the case of either zero or positive pump detuning, one can continuously connect to the case of equilibrium weakly interacting gases of Chapter 1, where the drag displays a continuous threshold with a critical velocity equal to the speed of sound. However, for negative pump detuning, where the spectrum of excitations is gapped, the drag shows a discontinuity with a critical velocity larger than the speed of sound. In this sense, the case of coherently driven microcavity polaritons in the pump-only configuration displays a richer phenomenology than the case of nonresonantly pumped polariton superfluids. We have also seen that the absence of a long-range wake does not imply the absence of dissipation, as a residual drag force due to the finite polariton lifetime is always present in the system. In this sense, one can say that we are not dealing with superfluid behaviour in a strict sense.

3.A GP equation for the LP branch

If one starts from a description of polaritons in terms of separate exciton and cavity photon fields, a rotation into the LP and UP basis, followed by neglecting the occupancy of the upper polariton branch, as explained in detail in Chapter 2, results in the following Gross-Pitaevskii equation (compare to Eq. (2.27)) for the LP field in momentum space $\psi_{LP}(\boldsymbol{r},t)=\sum_{\boldsymbol{k}} e^{i\boldsymbol{k}\cdot\boldsymbol{r}}\psi_{LP,\boldsymbol{k}}(t)$ [12]:

$$i\partial_t\psi_{LP,\boldsymbol{k}} = f_p e^{-i\omega_p t}\delta_{\boldsymbol{k},\boldsymbol{k}_p} + \left[\omega_{LP}(\boldsymbol{k}) - i\gamma(\boldsymbol{k})/2\right]\psi_{LP,\boldsymbol{k}} + \sum_{\boldsymbol{k}_1,\boldsymbol{k}_2} g_{\boldsymbol{k},\boldsymbol{k}_1,\boldsymbol{k}_2}\psi^*_{LP,\boldsymbol{k}_1+\boldsymbol{k}_2-\boldsymbol{k}}\psi_{LP,\boldsymbol{k}_1}\psi_{LP,\boldsymbol{k}_2} + C_{\boldsymbol{k}}\sum_{\boldsymbol{k}_1} V_{d,\boldsymbol{k}-\boldsymbol{k}_1}\psi_{LP,\boldsymbol{k}_1}C_{\boldsymbol{k}_1}\ , \quad (3.16)$$

where $\gamma(\boldsymbol{k})=\gamma_X X_{\boldsymbol{k}}^2+\gamma_C C_{\boldsymbol{k}}^2$ is the effective LP decay rate,

$$g_{\boldsymbol{k},\boldsymbol{k}_1,\boldsymbol{k}_2} = g_X X_{\boldsymbol{k}} X_{|\boldsymbol{k}_1+\boldsymbol{k}_2-\boldsymbol{k}|} X_{\boldsymbol{k}_1} X_{\boldsymbol{k}_2} \quad (3.17)$$

is the interaction strength, and where $V_d(\boldsymbol{r})=\sum_{\boldsymbol{k}} e^{i\boldsymbol{k}\cdot\boldsymbol{r}}V_{d,\boldsymbol{k}}$.

In these expressions, the coefficients (see Eqs. (2.16) and (2.17))

$$X^2_{\boldsymbol{k}}, C^2_{\boldsymbol{k}} = \frac{1}{2}\left(1 \pm \frac{\omega_C(\boldsymbol{k}) - \omega_X(0)}{\sqrt{(\omega_C(\boldsymbol{k}) - \omega_X(0))^2 + 4\Omega_R^2}}\right) \tag{3.18}$$

are the Hopfield coefficients used to diagonalise the free polariton Hamiltonian. We want here to justify the simplified description done in Eq. (3.1). If we follow the linear response expansion as in (3.4), the operator $\hat{\mathcal{L}}$ in momentum space analogous to (3.7) reads as:

$$\mathcal{L}_{\boldsymbol{k},\boldsymbol{k}_p} = \begin{pmatrix} \widetilde{\omega_{LP}}(\delta\boldsymbol{k} + \boldsymbol{k}_p) - i\gamma(\delta\boldsymbol{k} + \boldsymbol{k}_p)/2 & g_X X^2_{\boldsymbol{k}_p} X_{\delta\boldsymbol{k}+\boldsymbol{k}_p} X_{\delta\boldsymbol{k}-\boldsymbol{k}_p} \psi_p^2 \\ -g_X X^2_{\boldsymbol{k}_p} X_{\delta\boldsymbol{k}+\boldsymbol{k}_p} X_{\delta\boldsymbol{k}-\boldsymbol{k}_p} \psi_p^{\star 2} & -\widetilde{\omega_{LP}}(\delta\boldsymbol{k} - \boldsymbol{k}_p) - i\gamma(\delta\boldsymbol{k} - \boldsymbol{k}_p)/2 \end{pmatrix}, \tag{3.19}$$

where now $\widetilde{\omega_{LP}}(\delta\boldsymbol{k} \pm \boldsymbol{k}_p) = \omega_{LP}(\delta\boldsymbol{k} \pm \boldsymbol{k}_p) - \omega_p + 2g_X X^2_{\boldsymbol{k}_p} X^2_{\delta\boldsymbol{k}\pm\boldsymbol{k}_p} |\psi_p|^2$. It is easy to show that the eigenvalues of this operator coincide with our approximated expressions (3.10) in the limit of $\delta k \ll k_p$, when $X^2_{\delta\boldsymbol{k}\pm\boldsymbol{k}_p} \simeq X^2_{\boldsymbol{k}_p}$, $C^2_{\delta\boldsymbol{k}\pm\boldsymbol{k}_p} \simeq C^2_{\boldsymbol{k}_p}$ and when we can simply rename $g_X \equiv g_X X^4_{\boldsymbol{k}_p}$ and $\gamma \equiv \gamma(\boldsymbol{k}_p)$. It is interesting to note that, even if we would retain the linear terms in $\boldsymbol{k}_p \cdot \delta\boldsymbol{k}$ in the expansion of $X^2_{\delta\boldsymbol{k}\pm\boldsymbol{k}_p}$, this would result in a renormalisation of the fluid velocity $\boldsymbol{v}_p$ in the expression (3.10) which takes into account the blue-shift of the LP dispersion due to the interaction.

Chapter 4

Polariton superfluidity in the OPO regime

This Chapter presents a joint theoretical and experimental study of an OPO configuration (see Fig. 4.1) where a wide and steady-state condensate hits a stationary localized defect in the microcavity. Contrary to the criterion for quantized flow metastability for which the signal and idler display simultaneous locked responses, we find that their scattering properties when the OPO hits a static defect are different. In particular we investigate the scattering properties of all three fluids, the pump, the signal and the idler, in both real and momentum space. We find that the modulations generated by the defect in each fluid are not only determined by its associated Rayleigh scattering ring, but each component displays additional rings because of the cross-talk with the other components imposed by nonlinear and parametric processes. We single out three factors determining which one of these rings has the biggest influence on each fluid response: the coupling strength between the three OPO states, the resonance of the ring with the blue-shifted LP dispersion, and the values of each fluid group velocity and lifetime together establishing how far each modulation can propagate from the defect. The concurrence of these effects implies that the idler strongly scatters, inheriting the same modulations as the pump, while the modulations due to its own ring can propagate only very close to the defect and cannot be appreciated. However, the modulations in the signal are strongly suppressed, and not at all visible in experiments, because the slope of the polariton dispersion in its low momentum component brings all Rayleigh rings coming from pump and idler out of resonance.

Note that the kinematic conditions for OPO are incompatible with the pump and idler being in the subsonic regime. Thus, the coupling between the three components always implies some degree of scattering in the signal. In practice, the small value of the signal momentum strongly suppresses its visible modulations, as confirmed by the experimental observations.

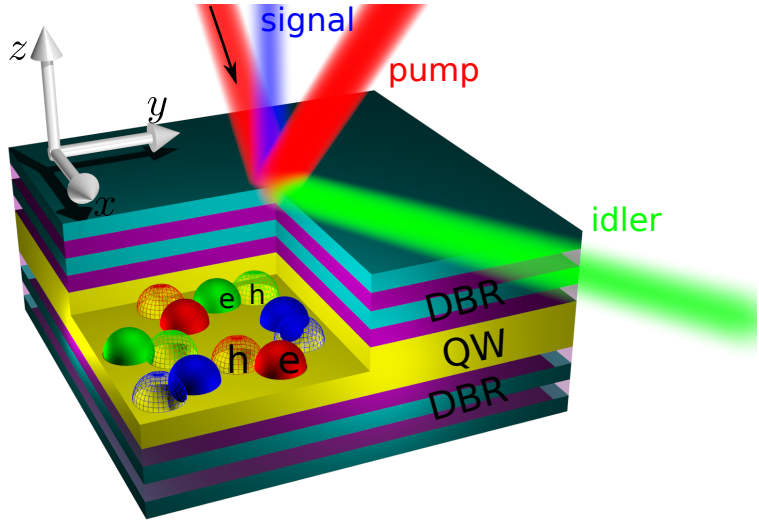

Figure 4.1: Pictorial representation of the optical parametric oscillator (OPO) state inside a planar microcavity. Cavity modes of the incoming external laser [black arrow] couple to the excitons formed by electron [e, solid spheres] – hole [h, hollow spheres] pairs inside the semiconductor quantum well (QW), creating the pump [red] polaritons, which coherently scatter into the signal [blue] and idler [green] states. All three types of polaritons decay into external radiation, emitted through the top distributed Bragg reflector (DBR) of the cavity.

4.1 Model

As explained in Chapter 2, the dynamics of polaritons in the OPO regime and their hydrodynamic properties when scattering against a defect can be described via a classical driven-dissipative non-linear Gross-Pitaevskii equation (GPE) for the coupled exciton and cavity fields $\psi_{X,C}(\mathbf{r},t)$ [2, 130]:

$$i\partial_t \begin{pmatrix} \psi_X \\ \psi_C \end{pmatrix} = \hat{H} \begin{pmatrix} \psi_X \\ \psi_C \end{pmatrix} + \begin{pmatrix} 0 \\ F_p(\mathbf{r},t) \end{pmatrix} . \tag{4.1}$$

The dispersive X- and C-fields decay at a rate $\gamma_{X,C}$ and are coupled by the Rabi splitting Ω_R, while the nonlinearity is regulated by the exciton coupling strength g_X:

$$\hat{H} = \begin{pmatrix} \omega_X(-i\nabla) - i\frac{\gamma_X}{2} + g_X|\psi_X|^2 & \Omega_R \\ \Omega_R & \omega_C(-i\nabla) - i\frac{\gamma_C}{2} + V_d \end{pmatrix} . \tag{4.2}$$

We describe the defect via a potential $V_d(\mathbf{r})$ acting on the photonic component; this can either be a defect in the cavity mirror or a localized laser field [26, 157, 162]. In the conservative, homogeneous, and linear regime [$\gamma_{X,C} = 0 = V_d(\mathbf{r}) =$

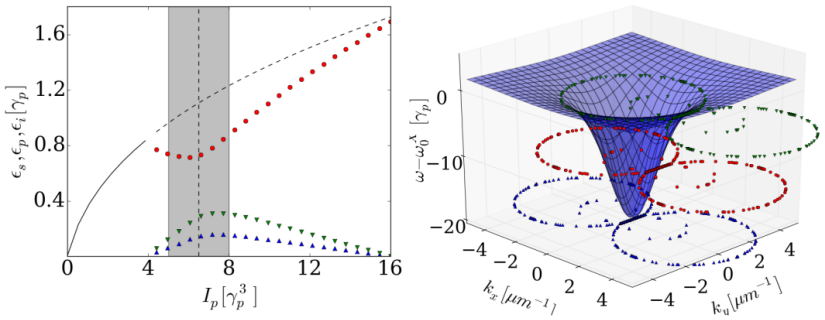

Figure 4.2: OPO mean-field blueshifts and fluctuation Rayleigh rings in the linear-response scheme for homogeneous pumping. Left panel: signal s ([blue] upper triangles), pump p ([red] circles), and idler i ([green] lower triangles) mean-field energy blueshifts $\epsilon_{n=s,p,i}$ (in units of $\gamma_p = \gamma_{\mathbf{k}_p}$) vs the rescaled pump intensity I_p (in units of γ_p^3) in the optical limiter regime. Parameters are $\Omega_R = 2.5$ meV, zero cavity-exciton detuning, $\gamma_X = \gamma_C = 0.12$ meV, $\omega_p - \omega_X(0) = -1.25$ meV, $k_p = 1.6\mu m^{-1}$, $k_s \simeq 0$, and $k_i = 3.2\mu m^{-1}$. The shaded area is stable OPO region, while the vertical dashed line corresponds to the pump power value chosen for plotting the right panel. Right panel: blueshifted LP dispersion (4.9) with superimposed Rayleigh curves $\Gamma_{p,i,(u,v),\tilde{\mathbf{k}}+\mathbf{k}_{p,i}}$ evaluated within the linear-response approximation (same symbols as left panel). The two rings corresponding to the signal state, $\Gamma_{s,(u,v),\tilde{\mathbf{k}}}$, are shrunk to zero because $k_s \simeq 0$.

g_X], the eigenvalues of $\hat{H}$ are given by the LP and UP energies Eq. (2.15). The cavity is driven by a continuous-wave laser field $F_p(\mathbf{r},t) = \mathcal{F}_p(\mathbf{r})e^{i(\mathbf{k}_p\cdot\mathbf{r}-\omega_p t)}$ into the OPO regime: Here, polaritons are continuously injected into the pump state with frequency ω_p and momentum $\mathbf{k}_p$, and, above a pump strength threshold, they undergo coherent stimulated scattering into the signal $(\omega_s, \mathbf{k}_s)$ and idler $(\omega_i, \mathbf{k}_i)$ states.

As a first step, it is useful to get insight into the system behaviour in the simple case of a homogeneous pump of strength $\mathcal{F}_p(\mathbf{r}) = f_p$. A numerical study of the coupled equations (4.1) for the more realistic case of a finite-size top-hat pump profile $\mathcal{F}_p(\mathbf{r})$ will be presented in Sec. 4.3. To further simplify our analysis, we assume here that the UP dispersion does not get populated by parametric scattering processes and thus, by means of the Hopfield coefficients Eqs. (2.16) and (2.17), we project the GPE (4.1) onto the LP component [11, 135] $\psi_{\mathbf{k}} = X_{\mathbf{k}}\psi_{X,\mathbf{k}} + C_{\mathbf{k}}\psi_{C,\mathbf{k}}$, where $\psi(\mathbf{r},t) = \sum_{\mathbf{k}} e^{i\mathbf{k}\cdot\mathbf{r}}\psi_{\mathbf{k}}(t)$. As explained in detail in

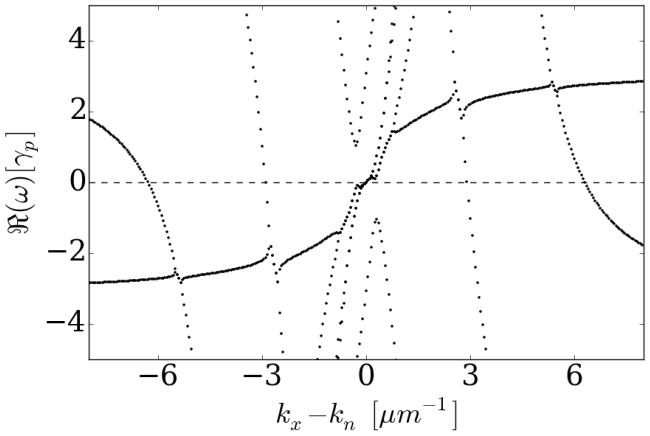

Figure 4.3: Spectrum of collective excitations. Cut at $k_y = 0$ of the real part of the quasiparticle energy dispersion $\Re[\omega_{n,(u,v),\mathbf{k}-\mathbf{k}_n}]$ plotted versus $k_x - k_n$. The spectrum is evaluated within the linear approximation scheme and the parameters are the same ones used for Fig. 4.2.

Sec. 2.7, we obtain Eq. (2.27):

$$i\partial_t\psi_{\mathbf{k}} = \left[\omega_{\mathrm{LP}}(\mathbf{k}) - i\frac{\gamma_{\mathbf{k}}}{2}\right]\psi_{\mathbf{k}} + C_{\mathbf{k}}\sum_{\mathbf{q}} C_{\mathbf{q}}V_d(\mathbf{k}-\mathbf{q})\psi_{\mathbf{q}} + \sum_{\mathbf{k}_1,\mathbf{k}_2} g_{\mathbf{k},\mathbf{k}_1,\mathbf{k}_2}\psi^*_{\mathbf{k}_1+\mathbf{k}_2-\mathbf{k}}\psi_{\mathbf{k}_1}\psi_{\mathbf{k}_2} + \tilde{f}_p(t)\delta_{\mathbf{k},\mathbf{k}_p}\ . \quad (4.3)$$

Here, $\gamma_{\mathbf{k}} = \gamma_X X_{\mathbf{k}}^2 + \gamma_C C_{\mathbf{k}}^2$ is the effective LP decay rate, the interaction strength is given by $g_{\mathbf{k},\mathbf{k}_1,\mathbf{k}_2} = g_X X_{\mathbf{k}} X_{\mathbf{k}_1+\mathbf{k}_2-\mathbf{k}} X_{\mathbf{k}_1} X_{\mathbf{k}_2}$, and the pumping term is given by $\tilde{f}_p(t) = C_{\mathbf{k}_p} f_p e^{-i\omega_p t}$. Note that the dependence on the exciton-exciton interaction strength g_X can be removed by rescaling both the LP field $\sqrt{g_X}\psi_{\boldsymbol{k}}(t) \to \psi_{\boldsymbol{k}}(t)$ and the pump strength $\sqrt{g_X} f_p \to f_p$, something we will do later on to all effects, working in terms of energy blueshifts and the rescaled pump intensity.

4.2 Linear-response theory

As already explained in Sec. 2.9, in the limit where the homogeneously pumped system is only weakly perturbed by the external potential $V_d(\mathbf{r})$, we apply a linear-response analysis [59]: The LP field is expanded around the mean-field terms for the three $n = 1, 2, 3 = s, p, i$ OPO states [130] (see Eqs. (2.38) and (2.41))

$$\psi_{\tilde{\mathbf{k}}} = \sum_{n=1}^{3} e^{-i\omega_n t}\left[\psi_n\delta_{\tilde{\mathbf{k}},0} + u_{n,\tilde{\mathbf{k}}}e^{-i\omega t} + v^*_{n,-\tilde{\mathbf{k}}}e^{i\omega t}\right]\ , \quad (4.4)$$

where $\tilde{\mathbf{k}} = \mathbf{k} - \mathbf{k}_n$. Eq. (4.3) is expanded linearly in both the fluctuation terms, $u_{n,\tilde{\mathbf{k}}}$ and $v_{n,\tilde{\mathbf{k}}}$, as well as the defect potential. At zeroth order, the three complex uniform mean-field equations can be solved to obtain the dependence of the signal, pump and idler energy blueshifts, $\epsilon_n = g_X X^2_{\mathbf{k}_n} |\psi_n|^2$ on the system parameters [135]. A typical behaviour of ϵ_n as a function of the rescaled pump intensity $I_p = g_X C^2_{\mathbf{k}_p} f_p^2 / X^2_{\mathbf{k}_p}$ in the optical limiter regime is plotted in the left panel of Fig. 4.2. At first order, one obtains six coupled equations diagonal in momentum space [29]

$$\omega \mathbf{w}_{\tilde{\mathbf{k}}} = \mathcal{L}_{\tilde{\mathbf{k}}} \mathbf{w}_{\tilde{\mathbf{k}}} + \frac{1}{2} \mathbf{\Psi}_d \, , \tag{4.5}$$

for the six-component vector $\mathbf{w}_{\tilde{\mathbf{k}}} = (u_{n,\tilde{\mathbf{k}}}, v_{n,\tilde{\mathbf{k}}})^T$ and for the potential part, $\mathbf{\Psi}_d = (\psi_n C_{\mathbf{k}_n} C_{\mathbf{k}+\mathbf{k}_n} V_d(\mathbf{k}), -\psi_n^* C_{\mathbf{k}_n} C_{\mathbf{k}_n - \mathbf{k}} V_d(-\mathbf{k}))^T$. To understand the origin of the factor $1/2$ in Eq. (4.5), it is sufficient to consider one component only, and start from Eq. (3.4) used in Sec. 3.1. The connection becomes clear once we write the fluctuation part as $\delta\psi(\boldsymbol{r}, t) = \frac{1}{2} \left\{ \delta\psi(\boldsymbol{r}, t) + [\delta\psi^\star(\boldsymbol{r}, t)]^\star \right\}$ and compare it to Eq. (2.38) of Sec. 2.8.

In (4.5) we have only kept the terms oscillating at the frequencies $\omega_n \pm \omega$ and neglected the other terms in the expansion (i.e., $2\omega_n - \omega_m \pm \omega$), which are oscillating at frequencies far from the LP band, and thus with negligible amplitudes. In the particlelike and the holelike channels, the Bogoliubov matrix determining the spectrum of excitations can be written as [29]

$$\mathcal{L}_{\mathbf{k}} = \begin{pmatrix} M_{\mathbf{k}} & Q_{\mathbf{k}} \\ -Q^*_{-\mathbf{k}} & -M^*_{-\mathbf{k}} \end{pmatrix} \, , \tag{4.6}$$

where the three OPO states components are

$$\begin{aligned} (M_{\mathbf{k}})_{mn} &= \left[\omega_{LP}(\mathbf{k}_m + \mathbf{k}) - \omega_m - i \frac{\gamma_{\mathbf{k}_m + \mathbf{k}}}{2} \right] \delta_{m,n} + 2 \sum_{q,t=1}^{3} g_{\mathbf{k}_m+\mathbf{k}, \mathbf{k}_n+\mathbf{k}, \mathbf{k}_t} \psi_q^* \psi_t \delta_{m+q, n+t} \\ (Q_{\mathbf{k}})_{mn} &= \sum_{q,t=1}^{3} g_{\mathbf{k}_m+\mathbf{k}, \mathbf{k}_q, \mathbf{k}_t} \psi_q \psi_t \delta_{m+n, q+t} \, . \end{aligned} \tag{4.7}$$

In absence of a defect potential ($\mathbf{\Psi}_d = 0$), Eq. (4.5) is the eigenvalue equation for the spectrum of excitations of a homogeneous OPO, i.e., $\det(\mathcal{L}_{\tilde{\mathbf{k}}} - \omega) = 0$. We plot in Fig. 4.3 a typical collective dispersion (here we consider the same system parameters as the ones used in Fig. 4.2), by plotting the real part of the Bogoliubov matrix eigenvalues $\Re[\omega_{n,(u,v),\mathbf{k}-\mathbf{k}_n}]$ as a function of $k_x - k_n$ (cut at $k_y = 0$). The spectrum has six branches, $\omega_{n,(u,v),\tilde{\mathbf{k}}}$, labeled by $n = s, p, i$ and (u, v). Even though these degrees of freedom are mixed together, at large momenta, one recovers the LP dispersions shifted by the three states' energies and momenta, i.e.,

$$\lim_{\tilde{k} \gg \sqrt{4 m_C \Omega_R}} \omega_{n,(u,v),\tilde{\mathbf{k}}} = \pm (\omega_{LP}(\mathbf{k} - \mathbf{k}_n) - \omega_n) \, , \tag{4.8}$$

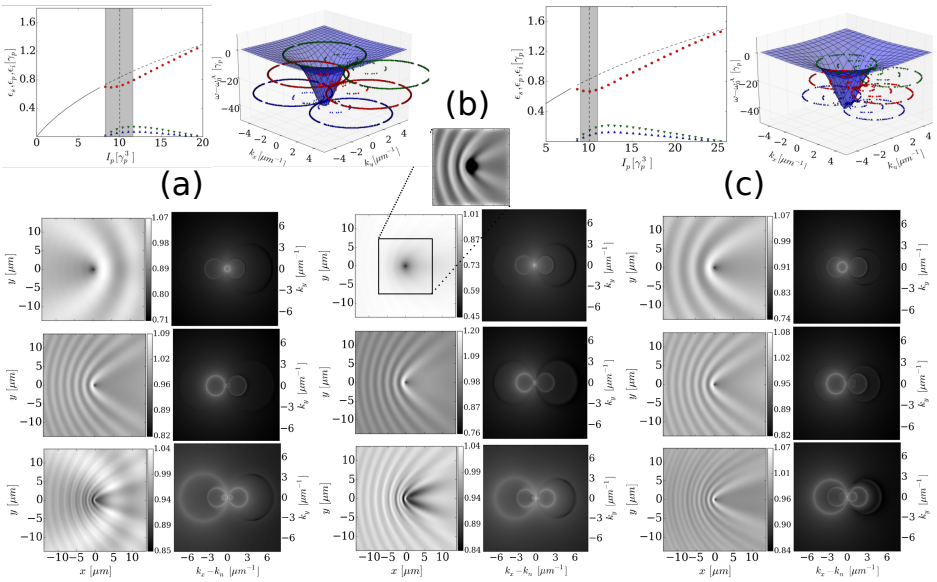

Figure 4.4: Linear response of the three OPO states to a static δ-defect for $k_s = -0.4$ [column (a)], 0.0 [column (b)] and 0.7 μm^{-1} [column (c)]. The parameters are given in Fig. 4.2, and $g_V = 0.5\gamma_p$ μm^2. *Column (a):* Top row is the analogue of Fig. 4.2, for negative signal momentum. The three bottom rows show the rescaled emission in real $|\psi(\mathbf{r},\omega_n)|^2/|\psi_n|^2$ (left panels in linear scale) and momentum space $|\psi_{\tilde{\mathbf{k}}}(\omega_n)|^2$ (right panels in logarithmic scale) filtered at the energies of the signal (top), pump (middle) and idler (bottom). *Column (c):* Same as column (a), for a positive signal momentum. *Column (b):* Vanishing signal momentum; the corresponding mean-field blueshifts and Rayleigh rings are plotted in Fig. 4.2. The inset shows the Gaussian-filtered (see main text) signal emission.

where + (−) corresponds to the u (v) particlelike (holelike) branch. The OPO solution is stable (shaded area in Fig. 4.2) as far as $\Im[\omega_{n,(u,v),\tilde{\mathbf{k}}}] < 0$. Note also that, owing to the $U(1)$ symmetry of the OPO equations of motion (see Sec. 2.9), no restoring force would oppose a rotation of the signal-idler phases, meaning that the generator of such global rotations, $(i\psi_s, 0, -i\psi_i, -i\psi_s^\star, 0, i\psi_i^\star)$, is an eigenvector of $\mathcal{L}_{\tilde{\mathbf{k}}=0}$ with eigenvalue 0 [29].

The shape of the patterns, or Cherenkov-like waves, resulting from the elastic scattering of the OPO 3-fluids against the static ($\omega = 0$) defect can be determined starting from the spectrum, and in particular evaluating the closed curves $\Gamma_{n,(u,v),\tilde{\mathbf{k}}}$ in $\mathbf{k}$-space, or "Rayleigh rings" [57] defined by the condition $\Re[\omega_{n,(u,v),\tilde{\mathbf{k}}}] = 0$. Even if they do not appear to be relevant here, note that the presence of a non-vanishing imaginary part of the excitation spectrum $\Im[\omega_{n,(u,v),\tilde{\mathbf{k}}}] \neq$

0 introduces some complications: Even in the absence of any Rayleigh ring, the drag force can be non-vanishing (as we saw in Chapter 3 for the pump-only case) and the standard Landau criterion may fail to identify a critical velocity [28]. The modulations propagate with a direction $\hat{\eta}_{n,(u,v),\tilde{\mathbf{k}}}$ orthogonal to each curve $\Gamma_{n,(u,v),\tilde{\mathbf{k}}}$, a pattern wavelength given by the corresponding $|\tilde{\mathbf{k}}|$, and a group velocity $\mathbf{v}^{(g)}_{n,(u,v),\tilde{\mathbf{k}}} = \nabla_{\tilde{\mathbf{k}}}\Re[\omega_{n,(u,v),\tilde{\mathbf{k}}}]$, where $\xi_{n,(u,v),\tilde{\mathbf{k}}} = |\mathbf{v}^{(g)}_{n,(u,v),\tilde{\mathbf{k}}}/\Im[\omega_{n,(u,v),\tilde{\mathbf{k}}}]|$ determines the distance, at any given direction $\hat{\eta}_{n,(u,v),\tilde{\mathbf{k}}}$, over which the perturbation extends away from the defect. For a single fluid under a coherent pump, the qualitative shape of the modulation pattern generated in the fluid by the defect is mostly determined by the excitation spectrum [56, 155].

For OPO, the spectrum of excitation on top of each of the three, $n = 1, 2, 3$, states (see Fig. 4.3) generates six identical Rayleigh rings $\Gamma_{n,(u,v),\tilde{\mathbf{k}}}$ for the three states. Note that the Rayleigh rings can be found by finding the intersections $\Re[\omega_{n,(u,v),\mathbf{k}-\mathbf{k}_n}] = 0$. The Rayleigh rings for the OPO conditions specified in Fig. 4.2 are clearly visible in the right panels of Fig. 4.4 (b), where we plot the $\mathbf{k}$-space photoluminescence filtered at the energy of each state, i.e., $|\psi_{\tilde{\mathbf{k}}}(\omega_n)|^2 = |\psi_n\delta_{\tilde{\mathbf{k}},0}+u_{n,\tilde{\mathbf{k}}}+v^*_{n,-\tilde{\mathbf{k}}}|^2$. We have chosen here a δ-like defect potential, $V_d(\mathbf{k}) = g_V$, but we have checked that our results do not depend on the specific shape of the defect potential: In particular, we have also considered the response to defects with smooth Gaussian-like profiles, whose effect is only to partially weaken the upstream modulations in real space.

As detailed in Sec. 2.9, the mean-field OPO ansatz assumes the signal momentum $\boldsymbol{k}_s$ to be an input parameter, rather than solving the full "selection problem" [135]. This is in contrast to both the full numerical solution of the GP Eq. (4.1) (Sec. 4.3) as well as experiments (Sec. 4.4), where the signal momentum is automatically selected (typically close to the bottom of the LP band) by parametric scattering processes. The reason why parametric scattering processes select a signal with a momentum close to zero, already very close to the lower pump thresold for OPO, is still awaiting an explaination. In particular, this cannot be addressed within a spatially homogeneous approximation where the three mean-field solutions for pump, signal, and idler states are described by plane waves. However, one can show [130] that, within the same mean-field approximation scheme, when increasing the pump power towards the upper threshold for OPO, the blue-shift of the LP polariton dispersion due to the increasing mean-field polariton density, causes the signal momentum to converge towards zero $\mathbf{k}_s \to 0$.

In the following, we take advantage of the broad range of possible choices for $\boldsymbol{k}_s$ (and thus $\boldsymbol{k}_i$) at mean-field level [135], and analyze three distinct cases: negative ($k_s = -0.4\ \mu\mathrm{m}^{-1}$), vanishing ($k_s = 0\ \mu\mathrm{m}^{-1}$) and positive ($k_s = 0.7\ \mu\mathrm{m}^{-1}$) signal momenta.

4.2.1 Vanishing signal momentum

For the OPO conditions considered here, the signal momentum is at $k_s \simeq 0$, and thus only four of the six Rayleigh rings are present. The same rings are also plotted in the right panel of Fig. 4.2, shifted at each of the three OPO states' momentum $\mathbf{k}_n$, $\Gamma_{n,(u,v),\tilde{\mathbf{k}}+\mathbf{k}_n}$ and energies ω_n. It is important to note that, even though the three OPO states have locked responses because they display the same spectrum of excitations, only one of the rings $\Gamma_{n,(u,v),\tilde{\mathbf{k}}+\mathbf{k}_n}$ is the most resonant at ω_n with the interaction blueshifted LP dispersion,

$$\bar{\omega}_{LP}(\mathbf{k}) = \omega_{LP}(\mathbf{k}) + 2X^2_{\mathbf{k}} \sum_{n=1}^{3} \epsilon_n \ , \tag{4.9}$$

where $\epsilon_n = g_X X^2_{\mathbf{k}_n} |\psi_n|^2$ are the mean-field energy blueshifts (measured in Fig. 4.2 in units of $\gamma_p = \gamma_{\mathbf{k}_p}$). This implies that the most visible modulation for each fluid should be the most resonant one, with superimposed weaker modulations coming from the other two state rings.

In the specific case of Fig. 4.2, the signal is at $k_s \simeq 0$ and thus produces no rings in momentum space. The other four rings are very far from being resonant with the blueshifted LP dispersion (4.9) at ω_s, and thus the signal displays only an extremely weak modulation coming from the next closer ring, which is the one associated with the pump state, $\Gamma_{p,u,\tilde{\mathbf{k}}+\mathbf{k}_s}$. We estimate that the signal modulation amplitudes are roughly 1% of the average signal intensity and about a factor of 10 times weaker than the modulation amplitudes in the pump fluid. To show that the signal has weak modulations coming from the pump, we apply a Gaussian filter to the real space images (see the inset of Fig. 4.4 (b)). This consists of the following procedure. The original data for the real space profile $\psi(\mathbf{r})$ are convoluted with a Gaussian kernel $K(\mathbf{r}-\mathbf{r}')$, obtaining a new profile, $\tilde{\psi}(\mathbf{r}') = \int d\mathbf{r}\psi(\mathbf{r})K(\mathbf{r}-\mathbf{r}')$, where short wavelengths features are smoothened out. The convoluted image $\tilde{\psi}(\mathbf{r}')$ is then subtracted from the original data, giving $\psi(\mathbf{r}) - \tilde{\psi}(\mathbf{r})$, and effectively filtering out all long wavelength details. This procedure reveals that indeed the pump imprints its modulations also into the signal, even though these are extremely weak, thus leaving the signal basically insensitive to the presence of the defect.

Pump and idler states are each mostly resonant with their own rings, i.e., $\Gamma_{p,u,\tilde{\mathbf{k}}+\mathbf{k}_p}$ at ω_p and $\Gamma_{i,u,\tilde{\mathbf{k}}+\mathbf{k}_i}$ at ω_i, respectively. Thus one should then observe two superimposed modulations in both pump and idler filtered emissions, the stronger one for each being the most resonant one. However, the modulations associated with the idler only propagate very close to the defect, at an average distance $\overline{\xi_{i,u,\tilde{\mathbf{k}}}} \sim 1.7\ \mu$m before getting damped, and thus are not clearly visible. For the OPO conditions considered, this is due to the small idler group velocity $\mathbf{v}^{(g)}_{i,u,\tilde{\mathbf{k}}}$, as the dispersion is almost excitonic at the idler energy.

We can conclude that, for the typical OPO condition with a signal at $k_s \simeq 0$, considered in Figs. 4.2 and 4.4 (b), the signal fluid does not show modulations and

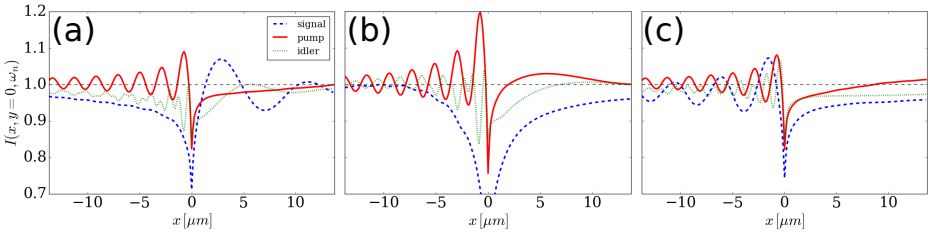

Figure 4.5: Real space signal, pump and idler OPO one-dimensional filtered profiles in the linear-response approximation. OPO filtered emissions along the $y = 0$ direction, $I(x, y = 0, \omega_n) = |\psi(x, y = 0, \omega_n)|^2/|\psi_n|^2$. A signal at $k_s = -0.4\ \mu\text{m}^{-1}$ [panel (a)] corresponds to Fig. 4.4 (a), a signal at $k_s = 0.0\ \mu\text{m}^{-1}$ [panel (b)] corresponds to Fig. 4.4 (b) and a signal at $k_s = 0.7\ \mu\text{m}^{-1}$ [panel (c)] corresponds to Fig. 4.4 (c). In each panel we plot the filtered profiles of signal, pump, and idler, while the horizontal gray dashed lines represent the values of the mean-field emission without a defect.

the extremely weak scattering inherited from the pump state can be appreciated only after a Gaussian filtering procedure of the image. In contrast, the idler has a locked response to the one of the pump state.

4.2.2 Finite signal momentum

Given the freedom of choice for the signal momentum $\mathbf{k}_s$ close to the lower OPO threshold, we consider here two additional cases, that could not be studied neither experimentally, nor within a full numerical approach, but that instead we can easily analize within the linear-response theory. In particular, we have left fixed the pumping conditions $k_p = 1.6\ \mu\text{m}^{-1}$ and $\omega_p - \omega_X(0) = -1.25$ meV and considered two opposite situations.

In the first case, the signal has a finite and positive momentum $k_s = 0.7\ \mu\text{m}^{-1}$ and thus the idler is at low momentum, $k_i = 2.5\ \mu\text{m}^{-1}$. The results are shown in Fig. 4.4 (c). Here we see that all six Rayleigh rings are clearly visible and, in addition, as the idler is at lower momentum compared to the case considered in Sec. 4.2.1, and thus its dispersion steeper, the idler group velocity is large enough to appreciate the modulation of the Rayleigh ring associated to this state. As a result, each of the three filtered OPO emissions exhibits as the strongest modulation the one coming from its own Rayleigh ring, including the signal which is now at finite and large momentum. In this case, the OPO response of each filtered state profile looks completely independent from the other, as if we were pumping each state independently.

In the second case, shown in Fig. 4.4 (a), the signal is finite and negative, $k_s = -0.4\ \mu\text{m}^{-1}$, and the idler is now at very large momentum, $k_i = 3.6\ \mu\text{m}^{-1}$, where its dispersion is very exciton-like and flat, and thus the idler has a very

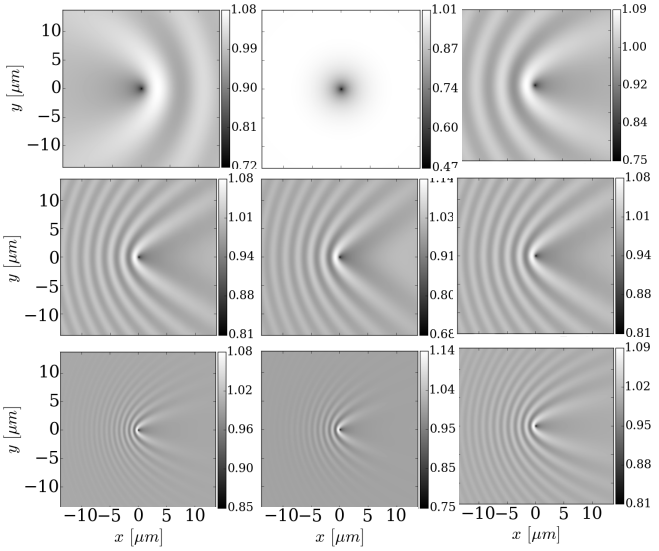

Figure 4.6: Real space profiles of three uncoupled signal, pump and idler fluids. The rescaled profiles $|\psi(\mathbf{r},\omega_n)|^2/|\psi_n|^2$ are obtained by setting all off-diagonal couplings in Eq. (4.6) to zero, resulting in three uncoupled signal (top row), pump (middle row), and idler (bottom row) fluids. The three columns correspond to the three different cases analysed within the linear-response approximation: the case of a signal at $k_s = -0.4$ μm^{-1} (left column) corresponds to the same conditions as Fig. 4.4 (a), a signal at $k_s = 0.0$ μm^{-1} (middle column) corresponds to Fig. 4.4 (b), and a signal at $k_s = 0.7$ μm^{-1} (right column) corresponds to Fig. 4.4 (c).

small group velocity and its own modulations are visible only very close to the defect. For this case, we can appreciate in the idler filtered profile overlapped modulations from all the three state Rayleigh rings (note that because the signal is at negative momentum, its modulations have an opposite direction compared to the ones of pump and idler), while in the signal we can mostly see the signal long wavelength modulations and only very weakly the pump one.

4.2.3 Discussion

We can compare the different modulation strengths of the three OPO profiles by looking at the color bars plotted next to the profiles. In order to better compare them on the same plot, we show in Fig. 4.5 the one-dimensional OPO filtered emissions along the $y = 0$ direction, rescaled by the mean-field solution ψ_n in absence of the defect, for the three cases analysed above. While for the OPO conditions with a signal at $k_s = 0.0$ μm^{-1} (middle panel, corresponding to Fig. 4.4 (b)), the imprinted modulations from the pump are hardly visible,

and can only be appreciated after a Gaussian filter manipulation, both OPO cases with a finite momentum signal result in modulations in the signal with an amplitude of the same order of magnitude of both pump and idler fluids.

In Fig. 4.6 we instead show the real space profiles obtained by setting all off-diagonal couplings in the Bogoliubov matrix $\mathcal{L}_{\mathbf{k}}$ of Eq. (4.6) to zero, resulting in three uncoupled signal (top row), pump (middle row), and idler (bottom row) fluids. This underlines the importance of the coupling between the three fluids in the three different OPO regimes we analysed within the linear-response approximation. In particular, for the OPO conditions such that the signal has a finite and positive momentum $\mathbf{k}_s$ (right column of Fig. 4.6, which corresponds to the conditions shown in Fig. 4.4 (c)), the coupling has little effect and the three fluids respond to the defect in practice in a independent way (each Rayleigh ring influences its own fluid). The OPO condition with a finite and negative momentum $\mathbf{k}_s$, which corresponds to the conditions shown in Fig. 4.4 (a), are shown in the left column of Fig. 4.6: Here, we can see that the coupling between the three fluids plays a role. The modulations of the pump can be appreciated both in the signal profile (though weakly), as well as in the idler profile. In the idler fluid its own modulations can only propagate very close to the defect and thus the only really appreciable modulations are the ones inherited from the pump. Finally, for the experimentally relevant case of an OPO with a signal at zero momentum (middle column of Fig. 4.6, which corresponds to the conditions shown in Fig. 4.4 (b)), there is also a role played by the coupling, though, as already thoroughly analysed, the modulations in the signal inherited from the pump can only be appreciated after a Gaussian filtering manipulation.

Finally note that, for the OPO conditions of Sec. 4.2.1, as well as for the finite momenta cases considered in Sec. 4.2.2, the subsonic to supersonic crossover of the pump-only state [26] happens at pump intensities well above the region of stability of OPO — the shaded gray regions of Fig. 4.2 and Fig. 4.4 (a) and (c). Thus, it is not possible to study a case where the pump is already subsonic and at the same time promotes stimulated scattering.

4.3 Numerical analysis

The results obtained within the linear-response approximation are additionally confirmed by an exact full numerical analysis of the classical driven-dissipative non-linear GPE (4.1) for the coupled exciton and cavity fields $\psi_{X,C}(\mathbf{r}, t)$ in the case of a finite size pump. Eq. (4.1) is solved numerically on a 2D grid of $N \times N = 2^8 \times 2^8$ points and a separation of 0.47 μm (i.e., in a box $L \times L = 121\ \mu\text{m} \times 121\ \mu\text{m}$) by using a 5^{th}-order adaptive-step Runge-Kutta algorithm. Convergence has been checked both with respect the resolution in space L/N as well as in momentum π/L, without [128, 151] as well as in presence of the defect. The same approach has been already used in the literature, for a review, see Refs. [128, 151]).

As for the system parameters, we have considered a LP dispersion at zero

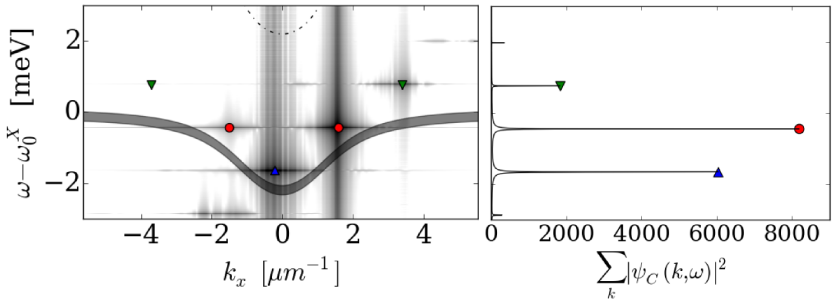

Figure 4.7: OPO spectrum obtained by full numerics. Left panel: Photonic component of the OPO spectrum in presence of a point-like defect, $|\psi_C(k_x, 0, \omega)|^2$ (logarithmic scale), as a function of the rescaled energy $\omega - \omega_X(0)$ versus the x-component of momentum k_x (cut at $k_y = 0$) for a top-hat pump (see text for the space profile and parameter values), with intensity $f_p = 1.23 f_p^{\rm th}$ above the OPO threshold, pump wave-vector $k_p = 1.6\ \mu{\rm m}^{-1}$ in the x-direction and $\omega_p - \omega_X(0) = -0.44$ meV. The symbols indicate the signal ([blue] upper triangle), pump ([red] circle), and idler ([green] lower triangle) energies, as well as the two momenta k_x on each state Rayleigh ring at $k_y = 0$. Note that the logarithmic scale results in a fictitious broadening in energy of the spectrum, which is in reality δ-like (see right panel). The bare LP dispersion, including its broadening due to finite lifetime, is plotted as a shaded grey region, while the bare UP dispersion as a (black) dot-dashed line. Right panel: Momentum integrated spectrum, $\sum_{\mathbf{k}} |\psi_C(\mathbf{k}, \omega)|^2$ (linear scale) as a function of the rescaled energy $\omega - \omega_X(0)$, where it can be clearly appreciated that the emission is δ-like in energy.

photon-exciton detuning, $\omega_C(0) = \omega_X(0)$, a dispersionless excitonic spectrum, $\omega_X(\mathbf{k}) = \omega_X(0)$ and a quadratic dispersion for photons $\omega_C(\mathbf{k}) = \omega_C(0) + k^2/2m_C$, with the photon mass $m_C = 2.3 \times 10^{-5} m_e$, where m_e is the bare electron mass. The LP dispersion Eq. (2.15) is characterised by a Rabi splitting $\Omega_R = 2.2$ meV. Furthermore, the exciton and cavity decay rates are fixed to $\gamma_X = \gamma_C = 0.53$ meV. For the defect we choose a δ-like potential

$$V_d(\mathbf{r}) = g_V \delta(\mathbf{r} - \mathbf{r}_0)\ , \tag{4.10}$$

where its location $\mathbf{r}_0$ is fixed at one of the $N \times N$ points of the grid. Note that in a finite-size OPO, local currents lead to inhomogeneous OPO profiles inside the pump spot, despite the external pump having a top-hat profile with a completely flat inner region [128, 151] — as shown later, this can be observed in the filtered OPO profiles evaluated in absence of a defect, shown as dashed lines in Fig. 4.9. We have thus chosen the defect location so that it lies in the smoothest and most homogeneous part of the OPO profiles.

Also we have checked that our results do not qualitatively depend on the

strength g_V (nor on the sign) of the defect potential, as far as this does not exceed a critical value above which it destabilises the OPO steady-state regime. The pump, $F_p(\mathbf{r},t) = \mathcal{F}_p(\mathbf{r})e^{i(\mathbf{k}_p\cdot\mathbf{r}-\omega_p t)}$, has a smoothen and rotationally symmetric top-hat profile, $\mathcal{F}_p(\mathbf{r}) = \mathcal{F}_p(r) = \frac{f_p}{2}[\tanh(\frac{r+\sigma_p}{r_0}) - \tanh(\frac{r-\sigma_p}{r_0})]$ with strength $f_p = 1.23 f_p^{\rm th} = 0.053$ meV/μm and parameters $r_0 = 8.68$ μm, $\sigma_p = 34.72$ μm. We pump at $k_p = 1.6$ μm^{-1} in the x-direction, $\mathbf{k}_p = (k_p, 0)$, and at $\omega_p - \omega_X(0) = -0.44$ meV, i.e., roughly 0.5 meV above the bare LP dispersion. By increasing the pump strength f_p, we find the threshold $f_p^{\rm th}$ above which OPO switches on, leading to two conjugate signal and idler states. We then fix the pump strength just above this threshold ($f_p = 1.23 f_p^{\rm th}$), where we find a steady state OPO solution which is stable (see Ref. [128] for further details). In absence of the defect, this condition corresponds to a signal state at $k_s = -0.2$ μm^{-1} and $\omega_s - \omega_X(0) = -1.64$ meV and an idler at $k_i = 3.4$ μm^{-1} and $\omega_i - \omega_X(0) = 0.76$ meV. It is interesting to note that already very close to the lower pump power threshold for OPO, the selected signal momentum is very close to zero. This contrasts with what one obtains in the linear approximation scheme, where instead just above the lower OPO threshold there exists a broad interval of permitted values for k_s (and thus k_i) — we have already mentioned this "selection problem" for parametric scattering in Sec. 4.2.

We evaluate the time dependent full numerical solution of (4.1) $\psi_{X,C}(\mathbf{r},t)$, until a steady state regime is reached. Here, both its Fourier transform to momentum $\mathbf{k}$ and energies ω can be evaluated numerically. We plot on the left panel of Fig. 4.7 a cut at $k_y = 0$ of the photonic component of the OPO spectrum in presence of a point-like defect, $|\psi_C(k_x, 0, \omega)|^2$, as a function of the rescaled energy $\omega - \omega_X(0)$ versus the x-component of momentum k_x (cut at $k_y = 0$). In the right panel we plot instead the corresponding momentum integrated spectrum, $\sum_{\mathbf{k}} |\psi_C(\mathbf{k},\omega)|^2$. Here, we can clearly see that the presence of the defect does not modify the fact that the OPO emission for the OPO signal ([blue] upper triangle), pump ([red] circle), and idler ([green] lower triangle) states has a completely flat dispersion in energy, thus indicating that a stable steady state OPO solution has been reached. Note that in the spectrum map of the left panel of Fig. 4.7, the logarithmic scale results in a fictitious broadening in energy. However, from the integrated spectrum plotted in linear scale in the right panel of Fig. 4.7 one can clearly appreciate that this emission is δ-like, exactly as it happens for the homogeneous OPO case [128]. Thus the effect of the defect is to induce only elastic (i.e., at the same energy) scattering; now the three OPO states emit each on its own Rayleigh ring (given each by the symbols on the left panel of Fig. 4.7 which represent the rings at a cut for $k_y = 0$). This makes it rather difficult to extract the separated signal, pump and idler profiles by filtering in momentum, as done previously for the homogeneous case, but it still allows to filter those profiles very efficiently in energy. In fact, because the emission is δ-like, it is enough to fix a single value of the energy ω to the one of the three states $\omega_{n=s,p,i}$, thus extracting the filtered profiles either in real space $|\psi_C(\mathbf{r},\omega_n)|^2$ or

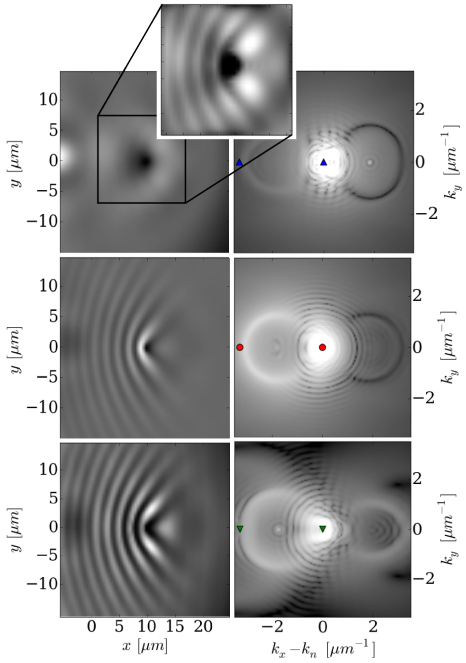

Figure 4.8: Full numerical responses to a static defect of the three OPO states in real and momentum space. Filtered OPO emissions (signal [top panels], pump [middle], and idler [bottom]) in real space $|\psi_C(\mathbf{r},\omega_n)|^2$ (left panels in linear scale) and momentum space $|\psi_C(\tilde{\mathbf{k}},\omega_n)|^2$ (right panel in logarithmic scale) obtained by a full numerical evaluation of (4.1). For the top left panel of the signal space emission, Gaussian filtering is applied to enhance the short wavelength modulations of this state, revealing that the modulations corresponding to the pump state are also imprinted (though weakly) into the signal. The symbols indicate the pump ring diameter extracted from fitting the upstream modulations and resulting in a density-wave wavevector coinciding with that of the pump, $k_p = 1.6\ \mu\mathrm{m}^{-1}$.

in momentum space $|\psi_C(\mathbf{k},\omega_n)|^2$ — we have however checked that integrating in a narrow energy window around ω_n does not quantitatively change the results.

The results of the above described filtering are shown in Fig. 4.8, where real-space emissions $|\psi_C(\mathbf{r},\omega_n)|^2$ are plotted in the left panels, while the ones in momentum space $|\psi_C(\tilde{\mathbf{k}},\omega_n)|^2$ are plotted in the right panels. We observe a very similar phenomenology to that one obtained in the linear approximation shown in Fig. 4.4 (b). The signal now is at slightly negative values of momenta $k_s = -0.2\ \mu\mathrm{m}^{-1}$, thus implying a very small Rayleigh ring associated with this state. Thus we observe that only the modulations associated with the pump are

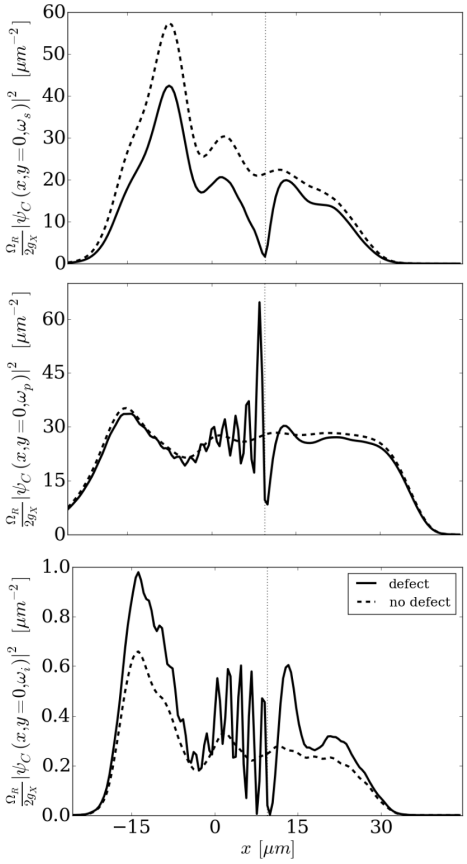

Figure 4.9: Real space signal, pump and idler OPO one-dimensional filtered profiles derived from finite size numerics with and without a defect. Rescaled OPO filtered emissions along the $y = 0$ direction, $|\psi_C(x, y = 0, \omega_n)|^2 \frac{\Omega_R}{g_X}$, obtained by numerically solving the GPE Eq. (4.1) of Sec. 4.1. While the dashed lines represent the filtered emissions of signal (top panel), pump (middle) and idler (bottom) for a top-hat pump without a defect, the solid lines are the same OPO conditions but now for a defect positioned at $(x_d, y_d) = (9.5, -0.5)$ μm corresponding to the vertical dotted lines. The system parameters are the same ones as those of Fig. 4.8.

the ones that are weakly imprinted in the signal state and that can be observed by means of a Gaussian filtering (inset of the top-left panel). We have fitted the upstream wave crests and obtained the same modulation wavevector as the pump one ([blue] upper triangles). Similar to the linear-response case, we also find here that the most visible perturbation in the emission filtered at the idler

energy is the one due to the pump Rayleigh ring. As before, the modulations due to the idler Rayleigh ring cannot propagate far from the defect because of the small group velocity associated with this state.

In Fig. 4.9 we instead plot the corresponding one-dimensional profiles in the $y = 0$ direction both in presence (solid line) and without (dashed line) a defect. Here, we can observe that, even if the pump has a top-hat flat profile, as also commented previously, in absence of a defect, the finite-size OPO is characterised by inhomogeneous profiles of signal, pump and idler because of localised currents. Furthermore, we observe that the presence of a defect induces strong modulations in pump and idler. Notice that the modulation imprinted by the pump into the signal is hardly visible in the top panel of Fig. 4.9 without the Gaussian filtering.

4.4 Experiments

We now turn to the experimental analysis, where a continuous-wave laser is used to drive a high quality ($Q = 14000$) GaAs microcavity sample into the OPO regime — details on the sample can be found in Refs. [163, 164]. The polariton dispersion is characterised by a Rabi splitting $\Omega_R = 2.7$ meV and the exciton energy is $\omega_X(0) = 1485.26$ meV, while the cavity-exciton detuning is slightly negative, -1 meV. The pump is at $k_p = 0.89\ \mu\text{m}^{-1}$ and $\omega_p - \omega_X(0) = -2.43$ meV, and, at pump powers 1.5-times above threshold, an OPO appears, with signal at small wavevector $k_s = 0.21\ \mu\text{m}^{-1}$ and $\omega_s - \omega_X(0) = -2.95$ meV, and idler at $k_i = 1.57\ \mu\text{m}^{-1}$ and $\omega_i - \omega_X(0) = -1.91$ meV. The defect used in the sample is a localized inhomogeneity naturally present in the cavity mirror. Note that the exact location of the defect can be extracted from the emission spectrum and is indicated with a dot (orange) symbol in the profiles of Fig. 4.10.

To filter the emission at the three states' energies, $I_{s,p,i}(\mathbf{r} = x, y)$, and to obtain 2D spatial maps for the three OPO states, one uses a spectrometer and, at a fixed position x_0, one obtains the intensity emission as a function of energy and position, $I(\epsilon, x_0, y)$. By changing x_0 one can build the full emission spectrum as a function of energy and 2D position, $I(\epsilon, \mathbf{r})$. The filtered emission for each OPO state is obtained from the integrals $I_{n=s,p,i}(\mathbf{r}) = \int_{\omega_n-\sigma}^{\omega_n+\sigma} d\epsilon I(\epsilon, \mathbf{r})$, with $\sigma = 0.08$ meV. The results are shown in Fig. 4.10 for, respectively, the signal (top panel), pump (middle) and the idler (bottom) profiles. Energy and momentum of the three OPO states are labeled with a [blue] upper triangle (signal), a [red] circle (pump), and a [green] lower triangle (idler), while the localised state, clearly visible just below the bottom of the LP dispersion, is indicated with the symbol d. The bare LP dispersion is extracted from an off-resonant low pump power measurement, as well as the emission of the exciton reservoir (X) and that of the UP dispersion (each in a different scale). The signal profile shows no appreciable modulations around the defect locations, nor could any be observed after applying a Gaussian filtering procedure to the image. In contrast, in agreement with the theoretical results, both filtered profiles of the pump and idler show

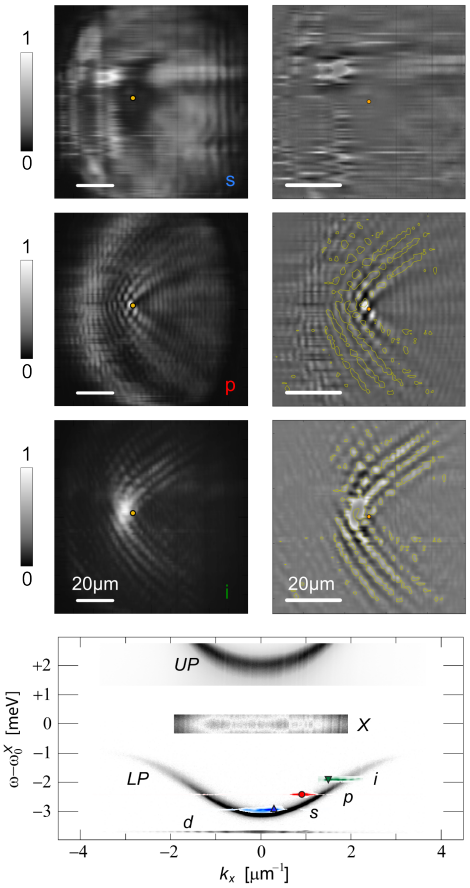

Figure 4.10: Experimental OPO spectrum (lower panel) and filtered emissions of signal (top), pump (middle), and idler (bottom) in presence of a structural defect. The six panels show the filtered emission profiles in real space $I_{s,p,i}(\mathbf{r})$. A Gaussian filtering to enhance the short wavelength modulations is applied in the right column. The extracted wave crests from the idler (yellow contours in the bottom panel) are also superimposed on the pump profile (middle) by applying a π phase-shift.

the same Cherenkov-like pattern. We extracted the wave crests from the idler profile ([yellow] contours in the bottom panel) and superimposed them on the pump profile (middle panel) with an added π phase-shift, revealing that the only modulations visible in the idler state are the ones coming from the pump state.

4.5 Conclusions

To conclude, we have presented a joint theoretical and experimental study of the superfluid properties of a nonequilibrium condensate of polaritons in the so-called optical parametric oscillator configuration by studying the scattering against a static defect. We have found that, while the signal is basically free from modulations, the pump and idler lock to the same response. We have highlighted the role of the coupling between the OPO components due to nonlinear and parametric processes. These are responsible for the transfer of the spatial modulations from one component to the other. This process is most visible in the clear spatial modulation pattern that is induced by the nonsuperfluid pump onto the idler, while the same modulations are only extremely weakly transferred into the signal, because of its low characteristic wavevector, so much that experimentally cannot be resolved. The main features of the real- and momentum-space emission patterns are understood in terms of Rayleigh scattering rings for each component and a characteristic propagation length from the defect; the rings are then transferred to the other components by nonlinear and parametric processes.

Much interest has been recently devoted to aspects related to algebraic order [165, 166] and superfluid response [153] in drive-dissipative polariton condensates. Our theoretical and experimental results further stress the complexities and richness involved when looking for superfluid behavior in nonequilibrium multicomponent condensates such as the ones obtained in the OPO regime.

Chapter 5

Landau levels in driven-dissipative cavity arrays

In 1984, Michael Berry showed that the adiabatic evolution of energy eigenfunctions with respect to a time-dependent Hamiltonian contains a phase of geometrical origin, commonly known today by the name of "Berry's phase" [167]. Although Berry's seminal paper gave the example of a spinor's evolution under slowly changing magnetic field, geometric phases [168] with similar origin have been encountered in a plethora of physical contexts, ranging from hydrodynamics to quantum field theory, the quantum Hall effect and topological insulators.

In a condensed matter context, the eigenstates of electrons in a periodic lattice can be labeled by a band index n and the crystal momentum $\boldsymbol{k}$. The Berry-phase physics arising when adiabatically transitioning between neighbouring wavevectors was appreciated only recently. This phenomenon can explain properties such as electric polarization, anomalous Hall conductivity or the quantization of conductance in the integer quantum Hall effect.

In the presence of a (synthetic) gauge field, the eigenstates making up an energy band can have nontrivial geometrical properties, as encoded in the Berry connection and Berry curvature [169, 170]. Understanding the geometry of eigenstates in a band is of great importance, not least because the integral of the Berry curvature over the 2D Brillouin zone (BZ) gives the first Chern number: the topological invariant responsible for the integer quantum Hall effect [109]. Consequently, there has been much work in recent years to develop new techniques with which to probe the properties of energy bands in photonics and ultracold gases. For example, the Berry curvature can be measured in the semiclassical dynamics of a wavepacket in an optical lattice [171–177] or in photon transport in a cavity array [178]. In all these cases, the physics can be most naturally understood by recognising that the Berry curvature acts like a magnetic field in momentum space [169, 179–181].

The analogy between Berry curvature and magnetism is most powerful when a geometrical energy band is subjected to an additional weak harmonic poten-

tial [182]. Then, in the effective momentum-space Hamiltonian, a harmonic potential acts like the kinetic energy of a particle in real space. Just as the physical momentum $\mathbf{p} - \mathbf{A}(\boldsymbol{r})$ is the sum of the canonical momentum $\mathbf{p}$ and the magnetic vector potential $\mathbf{A}(\boldsymbol{r})$ in the magnetic Hamiltonian, so the physical position $\mathbf{r} + \mathcal{A}_{n,n}(\boldsymbol{p})$, is given by the canonical position $\mathbf{r}$ and the Berry connection $\mathcal{A}_{n,n}(\boldsymbol{p})$ of band n in the effective Hamiltonian [179, 183–188]. The Berry curvature, $\Omega_n(\boldsymbol{p}) = \nabla \times \mathcal{A}_{n,n}(\boldsymbol{p})$, is then like a momentum-space magnetic field. For certain models, this analogy leads to a clear analytical understanding of single-particle dynamics [182, 189–191]. In particular, we will focus on the small-flux limit of the Harper-Hofstadter Hamiltonian [88, 89], which is a model that has recently been realized in a multitude of experimental configurations, ranging from ultracold gases [94, 95, 192, 193], solid state superlattices [90, 91] and silicon photonics [3] to classical systems such as coupled pendula [194] and oscillating circuits [195]. As first shown in Ref. [182], the eigenstates of this model in the presence of a harmonic trap are toroidal Landau levels in momentum space. Not only would an observation of these states constitute the first exploration of analogue magnetic states in momentum space, but also the first experimental study of magnetism on a torus.

Most theoretical works on momentum-space Landau levels have focused on conservative dynamics [182, 191], while photonic systems naturally include driving and dissipation [196]. In this Chapter, we present a realistic experimental proposal for the observation of these states in a driven-dissipative 2D lattice of cavities, such as the array of coupled silicon ring resonators of Ref. [3], where link resonators were used to simulate a synthetic gauge field for photons. We combine this set-up with a harmonic potential, introduced, for example, by a spatial modulation of the resonator size. We demonstrate numerically that the main features of momentum-space Landau levels will be observable spectroscopically in this system for realistic parameters.

In this Chapter, we also emphasize how the inherent driving and dissipation in photonics can be a key advantage in probing properties that are otherwise inaccessible. Firstly, the spectroscopic measurements discussed here are sensitive to the absolute energy of a state. From this, we show how to extract the energy shift due to the off-diagonal matrix elements of the Berry connection $\mathcal{A}_{n,n'}(\boldsymbol{p})$ relating eigenstates in different bands n and n'. Only very recently has the first measurement of such effects been reported in ultracold atomic gases [197, 198], and the approach used in this experiment would be difficult to apply to a photonics set-up. The scheme we present may therefore be useful for the characterisation of energy bands in topologically-nontrivial photonic systems.

Secondly, since the photon steady-state depends on the overlap between the (observable) spatial amplitude profile of the drive and of the eigenstates [196], the observables will depend on the phase of the eigenfunctions and thus on the specific synthetic magnetic gauge that is implemented in a given experimental realization of the Harper-Hofstadter Hamiltonian using a synthetic gauge field. We note that a related gauge-sensitivity has also recently been of much interest in ultracold

gases in suitably designed time-of-flight experiments [199–202]. Experiments on synthetic magnetic fields therefore present the opportunity of straightforwardly probing gauge-dependent physics.

This Chapter is organized as follows: in Section 5.1 we add a harmonic trap to the HH model introduced in Sec. 1.7. We explain how the eigenstates can be understood as momentum-space Landau levels in Section 5.1.1, before we discuss the breakdown of approximations in Section 5.1.2, focusing on the energy shift from the off-diagonal matrix elements of the Berry connection. Then in Section 5.1.3, we add driving and dissipation to the model. In Section 5.2.1, we show numerical results highlighting gauge-dependent effects, before presenting a viable proposal for a photonics-based experiment in Section 5.2.2. Finally, we draw conclusions in Section 5.3.

5.1 The trapped Harper-Hofstadter Model

In this Chapter, we study the Harper-Hofstadter Hamiltonian $\mathcal{H}_0$ in the presence of an external harmonic trap. The full tight-binding Hamiltonian $\mathcal{H}$ of this system is

$$\mathcal{H} = \mathcal{H}_0 + \frac{1}{2}\kappa \sum_{m,n} \left[(m-m_0)^2 + (n-n_0)^2\right] \hat{a}^\dagger_{m,n}\hat{a}_{m,n} \tag{5.1}$$

$$\mathcal{H}_0 = -J \sum_{m,n} (e^{i\phi^x_{m,n}} \hat{a}^\dagger_{m+1,n}\hat{a}_{m,n} + e^{i\phi^y_{m,n}} \hat{a}^\dagger_{m,n+1}\hat{a}_{m,n}) + \text{H.c.} \tag{5.2}$$

where J is the real hopping amplitude and $\hat{a}^\dagger_{m,n}$ ($\hat{a}_{m,n}$) are the creation (annihilation) operators for a particle on a square lattice at site (m,n). The harmonic trap is of strength κ and is centered at a position (m_0, n_0) which, in general, need not coincide with a lattice site. Throughout, the lattice spacing is set equal to one.

As explained in Sec. 1.7, the hopping phases $\phi = (\phi^x_{m,n}, \phi^y_{m,n})$ are the Peierls phases gained by a charged particle hopping in the presence of a perpendicular magnetic field [88, 89]. The sum of the phases around a square plaquette of the lattice is therefore equal to $2\pi\alpha$, where α is the number of magnetic flux quanta through the plaquette (with $\hbar = e = 1$). For neutral particles, such as photons, these phases can be imposed artificially to simulate the effects of magnetism, for example, by inserting link resonators into an array of silicon ring resonators as mentioned above [3].

Although the sum of phases around a plaquette is set by the external (synthetic) flux, the exact form of the hopping phases themselves depends on the choice of magnetic gauge. In the Landau gauge, for example, $\phi = (0, 2\pi\alpha m)$ such that only the hopping amplitude along one direction is modified. Conversely, in the symmetric gauge, $\phi = (-\pi\alpha n, \pi\alpha m)$ and so hopping terms along both x and y are affected, preserving the C_4 rotational invariance of the lattice.

This gauge-dependence of the hopping phases is reflected in the spatial profile of the phase of an eigenstate of $\mathcal{H}$. In a photonics experiment, this phase is an observable quantity as the intensity response of a system to a given external driving is determined by the overlap of the spatial amplitude distribution of the pump with the eigenstates. Such experiments will therefore be sensitive to the synthetic magnetic gauge as we discuss in Section 5.2.2.

5.1.1 Toroidal Landau Levels in Momentum Space

Having introduced the full Hamiltonian in Eq. (5.1), we now review how the eigenstates of this model in an appropriate limit can be understood as toroidal Landau levels in momentum space [182]. Throughout the following discussion, we assume that the trap is centered at the origin $(m_0, n_0) = (0, 0)$.

We begin from the eigenstates of the Harper-Hofstadter model $\mathcal{H}_0|\chi_{n,\mathbf{p}}\rangle = E_n(\boldsymbol{p})|\chi_{n,\mathbf{p}}\rangle$, where $E_n(\boldsymbol{p})$ is the energy dispersion of band n at crystal momentum $\mathbf{p}$. As the spatially-dependent hopping phases in $\mathcal{H}_0$ break translational invariance, new magnetic translation operators must be introduced to define a larger magnetic unit cell, containing an integer number of magnetic flux quanta [102, 103, 172]. Then translational symmetry is restored and Bloch's theorem can be applied to write the eigenstates as $|\chi_{n,\mathbf{p}}\rangle = \frac{1}{\sqrt{N}} e^{i\mathbf{p}\cdot\mathbf{r}}|u_{n,\mathbf{p}}\rangle$, where $|u_{n,\mathbf{p}}\rangle$ is the periodic Bloch function and N is the number of lattice sites. Thanks to the new larger unit cell, the crystal momentum and the periodic Bloch functions here are defined in the smaller magnetic Brillouin zone (MBZ). For example, hereafter, we take the number of flux quanta per plaquette to be of the form $\alpha = 1/q$, where q is an integer. Then the magnetic unit cell can be chosen to be q times larger than the original unit cell, while the MBZ is q times smaller than the original BZ.

Adding the harmonic trap breaks all translational symmetry of the lattice, but we can use the eigenstates of $\mathcal{H}_0$ as a basis in which to expand the new wave function $|\psi\rangle = \sum_n \sum_{\mathbf{p}} \psi_n(\mathbf{p})|\chi_{n,\mathbf{p}}\rangle$. Substituting this expansion into the full Schrödinger equation $i\partial_t|\psi\rangle = \mathcal{H}|\psi\rangle$, it can be shown that the expansion coefficients $\psi_n(\mathbf{p})$ satisfy [182]:

$$i\partial_t\psi_n(\mathbf{p}) = E_n(\mathbf{p}) + \frac{\kappa}{2}\sum_{n',n''}\Big(\delta_{n,n'}i\nabla_{\mathbf{p}} + \mathcal{A}_{n,n'}(\mathbf{p})\Big)\times \\ \times\Big(\delta_{n',n''}i\nabla_{\mathbf{p}} + \mathcal{A}_{n',n''}(\mathbf{p})\Big)\psi_{n''}(\mathbf{p}), \quad (5.3)$$

where $\mathcal{A}_{n,n'}(\mathbf{p}) = i\langle u_{n,\mathbf{p}}|\nabla_{\mathbf{p}}|u_{n',\mathbf{p}}\rangle$ is the matrix-valued Berry connection.

To proceed, we consider the harmonic trap to be sufficiently weak compared to the bandgap that we can make a single-band approximation [182]. This assumes that only one coefficient ψ_n is non-negligible and that the external trap does not significantly mix different energy bands. Then Eq. (5.3) reduces to

$$i\partial_t\psi_n(\mathbf{p}) = \widetilde{\mathcal{H}}\psi_n(\mathbf{p}), \quad (5.4)$$

where we have introduced the effective momentum-space Hamiltonian

$$\widetilde{\mathcal{H}} = \frac{\kappa}{2}[i\nabla_{\mathbf{p}} + \mathcal{A}_{n,n}(\mathbf{p})]^2 + E_n(\mathbf{p}) + \frac{\kappa}{2}\sum_{n'\neq n} |\mathcal{A}_{n,n'}(\mathbf{p})|^2. \tag{5.5}$$

For the moment we focus on the first two terms; we discuss the role of the last term, which comes from the off-diagonal matrix elements of the Berry connection, in detail in the next subsection. As can be seen, there is a close analogy between the first two terms in the momentum-space Hamiltonian and that of a charged particle in an electromagnetic field *in real space*:

$$\mathcal{H}' = \frac{\left[-i\nabla_{\mathbf{r}} - \mathbf{A}(\mathbf{r})\right]^2}{2M} + \Phi(\boldsymbol{r}). \tag{5.6}$$

In this analogy, the role of the particle mass M is played by κ^{-1}, while the scalar potential $\Phi(\boldsymbol{r})$ is replaced by the energy band dispersion $E_n(\mathbf{p})$ and the magnetic vector potential $\mathbf{A}(\mathbf{r})$ by the intra-band Berry connection $\mathcal{A}_{n,n}(\mathbf{p})$. We note that both the magnetic vector potential and the Berry connection are gauge-dependent quantities. We hereafter refer to the gauge choice for the Berry connection as the Berry gauge, and the gauge choice for a real-space magnetic vector potential as the magnetic gauge. From the Berry connection, we can also define the geometrical Berry curvature $\Omega_n(\mathbf{p}) = \nabla \times \mathcal{A}_{n,n}(\mathbf{p})$, which acts like a momentum-space magnetic field $B(\mathbf{r})$.

The topology of momentum space also plays a crucial role here, as the MBZ is topologically equivalent to a torus. One important consequence of this is of course that the integral of Berry curvature over the whole MBZ is quantised in units of the first Chern number $\mathcal{C}_n$. In the above analogy with magnetism, this means that the particle is confined to move on the surface of a torus, while the Chern number counts the number of magnetic monopoles contained inside [203].

The above analogy with magnetism is particularly powerful because there are natural limits for our model Eq. (5.1) in which the eigenstates of Eq. (5.6) and hence of Eq. (5.5) are known analytically [182, 189, 191]. We will focus on the flat-band limit in which the bandwidth is much smaller than the trapping energy; for the energy bands of $\mathcal{H}_0$ with $\alpha = 1/q$, this assumption improves as κ decreases or as q increases. In this limit, we can firstly approximate $\Omega_n(\mathbf{p}) \approx \Omega_n$, so that the first term is analogous to the kinetic energy of a particle in a uniform magnetic field. Secondly, we can approximate $E_n(\mathbf{p}) \approx E_n$ so that the second term of $\widetilde{\mathcal{H}}$ is just a constant energy shift. Hence, the corresponding eigenstates can be understood as toroidal Landau levels in momentum space. We note that the opposite limit, in which the trapping energy is small compared to the bandwidth, also yields very interesting physics including the realisation of a Harper-Hofstatder model in momentum space [189, 204].

As shown in Ref. [182], the momentum-space toroidal Landau levels form semi-infinite ladders of states:

$$\epsilon_{n,\beta} = E_n + \left(\beta + \frac{1}{2}\right)\kappa|\Omega_n|, \tag{5.7}$$

where we have introduced the Landau level quantum number [85] $\beta = 0, 1, 2, \ldots$, and where $\kappa|\Omega_n|$ can be recognised as the analogue of the cyclotron frequency $\omega_c = e|B|/M$. Again, we note that here we have neglected the contribution from the last term in Eq. (5.5), as this will be discussed in the next subsection. As can be shown from the Diophantine equation for the Hall conductivity, for odd values of q, the Chern number of all bands except the middle band is $\mathcal{C}_n = -1$ [104]. Then as the Chern number is related to the uniform Berry curvature as $\mathcal{C}_n = (1/2\pi)\Omega_n A_{\mathrm{MBZ}}$, where $A_{\mathrm{MBZ}} = (2\pi)^2/q$ is the MBZ area, the Berry curvature is given by $|\Omega_n| = \frac{1}{2\pi\alpha}$ [182].

While the above spectrum does not directly depend on the toroidal topology of momentum space, the topology does enter into the eigenstate degeneracy, which is equal to $|\mathcal{C}_n|$, as well as into the analytical form of the eigenstates in the MBZ. For example, for the bands with $\mathcal{C}_n = -1$, the eigenstates can be written as [182]

$$\begin{aligned}\chi_\beta(\mathbf{p}) = \mathcal{N}_\beta^{l_{\Omega_n}} \sum_{j=-\infty}^{\infty} e^{-ip_y j} e^{-(p_x + j l_{\Omega_n}^2)^2/2l_{\Omega_n}^2} \\ \times H_\beta(p_x/l_{\Omega_n} + j l_{\Omega_n}),\end{aligned} \tag{5.8}$$

$$\mathcal{N}_\beta^{l_{\Omega_n}} = \left(\frac{\sqrt{2/q}}{2^\beta \beta! \times 2\pi l_{\Omega_n}^2} \right)^{1/2}, \tag{5.9}$$

where H_β are the Hermite polynomials and $l_{\Omega_n} = \sqrt{1/|\Omega_n|}$ is the analogue of the magnetic length. Here we have taken the Berry gauge to have a Landau form $\mathcal{A}_n(\mathbf{p}) = \Omega_n p_x \hat{\mathbf{p}}_y$ parallel to the $\hat{\mathbf{p}}_y$ unit vector in momentum space. We have also assumed that the MBZ is of length 2π in one momentum direction, and $2\pi/q$ in the other direction, corresponding to a magnetic unit cell of q plaquettes containing one flux quantum. While this choice of MBZ is valid in any magnetic gauge of the underlying Harper-Hofstadter model, it is particularly natural when the hopping phases in $\mathcal{H}_0$ are in the Landau magnetic gauge $\phi = (0, 2\pi\alpha m)$, as we shall discuss further below.

5.1.2 The Berry connection

We now study the effects of the last term in the momentum-space Hamiltonian Eq. (5.5) which comes from the off-diagonal matrix elements of the Berry connection [169]:

$$\begin{aligned}\delta E_n(\mathbf{p}) &\equiv \frac{\kappa}{2} \sum_{n' \neq n} |\mathcal{A}_{n,n'}(\mathbf{p})|^2 \\ &= \frac{\kappa}{2} \sum_{n' \neq n} \frac{|\langle u_{n,\mathbf{p}} | \nabla_{\mathbf{p}} \mathcal{H}_0(\mathbf{p}) | u_{n',\mathbf{p}} \rangle|^2}{\left[E_{n'}(\mathbf{p}) - E_n(\mathbf{p})\right]^2}.\end{aligned} \tag{5.10}$$

This can be recognised as a momentum-space counterpart of the real-space geometrical scalar potential previously studied in atomic systems [39, 205, 206].

In these systems, the scalar potential arises from real-space Berry connections, which can be created, for example, by using spatially-dependent optical fields to dress the atoms.

In the flat-band limit, we have checked numerically that we can approximate the momentum-space geometrical scalar potential as $\delta E_n(\mathbf{p}) \approx \delta E_n$ and so this contributes only a uniform constant energy shift. This term was not considered in previous works [182, 189], as these works focused on systems such as ultracold atomic gases, where the absolute energy is not easily experimentally observable. As we will discuss in the next section, spectroscopic measurements in photonics are sensitive to the energy of a state, therefore such corrections may be extracted experimentally. We note that an analogous effect has also been derived for the effective momentum-space magnetic Hamiltonian for a trapped particle in an ideal flat band [191], and predicted for the frequency spectrum associated with excitonic states in transition metal dichalcogenides [207].

To see under what conditions the off-diagonal elements of the Berry connection are relevant, we compare the energy E_{ex} obtained from an exact numerical diagonalization of Eq. (5.1) with the analytical eigenenergy E_{an} predicted by Eq. (5.7). We focus on the lowest ladder of states, associated with band $n = 0$ in Eq. (5.7), at energies which are below the onset of the second ladder around energy E_1. This allow us to easily identify which numerical eigenvalue should correspond to which Landau level quantum number [182].

We introduce two dimensionless parameters η_{zpe} and η_{lev} to quantify deviations between the numerics and analytics. The former represents the error in the "zero-point energy", and is defined as the energy of the lowest numerical state relative to the analytical $n = 0, \beta = 0$ Landau level. The latter is the level spacing error, which we define as the difference between the numerical energy spacing between two neighbouring states and the analytical spacing between states with β and $\beta - 1$ quantum numbers.

Considering first the "zero-point energy" error η_{zpe}, the analytical energy of the $n = 0, \beta = 0$ Landau level is given from Eq. (5.7) by:

$$E_{\text{an}} = \langle E_0(\mathbf{p}) \rangle_{\mathbf{p}} + \frac{1}{2}\frac{\kappa}{2\pi\alpha}, \tag{5.11}$$

where we have used that $|\Omega_n| = \frac{1}{2\pi\alpha}$ and where we calculate the uniform energy shift $E_0 = \langle E_0(\mathbf{p}) \rangle_{\mathbf{p}}$ as the average band-energy over the MBZ. This definition generalises our flat-band approximation to account for the non-zero bandwidth of the lowest band.

We then define the dimensionless parameter η_{zpe} as

$$\eta_{\text{zpe}} = \frac{4\pi\alpha}{\kappa}(E_{\text{ex}} - E_{\text{an}}). \tag{5.12}$$

This dimensionless error is plotted with a dashed line as a function of q for $\kappa = 0.02J$ in the top panel of Fig. 5.1. At small q, there is a large bandgap between

the lowest two Harper-Hofstadter energy bands, but the lowest band also has a large bandwidth. In this regime, the single-band approximation is reasonable, while the flat-band approximation breaks down leading to large errors. This limit requires a different analytical approach as previously presented in Ref. [189]. To account for the error at large q, we include the shift from the off-diagonal matrix elements of the Berry connection Eq. (5.10). We calculate this shift numerically from the eigenstates of the Harper-Hofstadter model, and we incorporate it into a second parameter

$$\eta_{\mathrm{zpe}}^{\mathrm{nab}} = \frac{4\pi\alpha}{\kappa}(E_{\mathrm{ex}} - E_{\mathrm{an}} - \langle \delta E_0(\mathbf{p}) \rangle_{\mathbf{p}}). \tag{5.13}$$

This is plotted as a solid line in the top panel of Fig. 5.1. As can be seen, this shift dramatically reduces the error in the zero point energy at large q. We also calculate this shift considering only the effects of band mixing with the second lowest band $n = 1$; this is indistinguishable on this scale from the full shift. This can be understood from the dependence on the bandgaps in Eq. (5.10), which shows that the contributions of high-energy bands are suppressed. As discussed further in Section 5.2.2, it would be possible experimentally to extract the energy of the lowest state; this could constitute the first direct measurement of the effects of the off-diagonal matrix elements of the Berry connection in a photonics system.

We turn now to the level-spacing error η_{lev}. This can be expressed as

$$\eta_{\mathrm{lev}} = \frac{2\pi\alpha}{\kappa}[E_{\mathrm{ex}}(\beta) - E_{\mathrm{ex}}(\beta - 1)] - 1, \tag{5.14}$$

where we have used that the analytical level spacing from Eq. (5.7) is simply $\kappa/2\pi\alpha$. We plot the level-spacing error in the bottom panel of Fig. 5.1 for $\beta = 1, 2, 3$ and 4. As can be seen here, there is a large variation in the errors at small q due to the large bandwidth [189]. On the other hand, we see that $\eta_{\mathrm{lev}} \ll 1$, for $q \gtrsim 6$, where the flat-band approximation improves. In this regime, the level-spacing error is much smaller than the zero-point error. This is because when the shift from the off-diagonal matrix elements of the Berry connection Eq. (5.10) is approximately uniform over the MBZ at large q, it just acts as a uniform energy shift on all the states in a ladder with band index n. Consequently, this shift drops out of the level spacing error between states, leaving only higher-order band-mixing terms. From perturbation theory, it is expected that mixing with other bands leads to a negative energy shift on states in the lowest band, and indeed this can be seen in both $\eta_{\mathrm{zpe}}^{\mathrm{nab}}$ and η_{lev} in the small negative errors found at large q.

5.1.3 Driving and dissipation

We now include in our model the driving and dissipation that are an integral part of the proposed photonics experiment. We assume there are uniform and local losses characterized by a loss rate γ, and that the pump is monochromatic, with

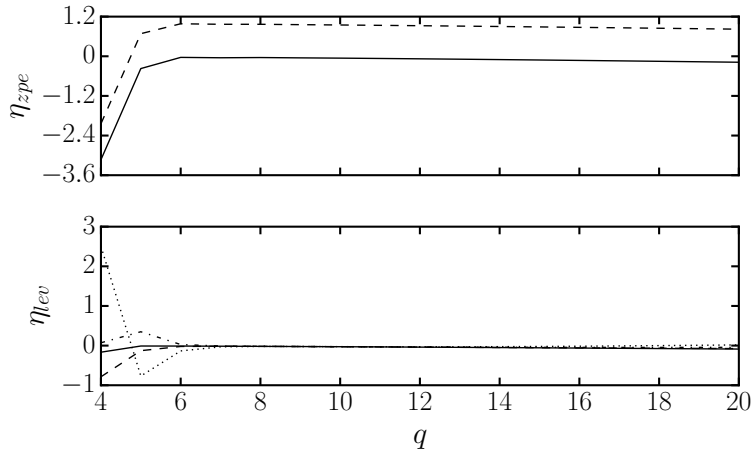

Figure 5.1: *Top panel*: "Zero-point energy" error, with (solid curve, $\eta_{\rm zpe}^{\rm nab}$) and without (dashed line, $\eta_{\rm zpe}$) the shift from the off-diagonal matrix elements of the Berry connection. Including just the first term in the sum Eq. (5.10) gives an identical curve to the one of $\eta_{\rm zpe}^{\rm nab}$. The chosen trap strength is $\kappa = 0.02J$. *Bottom panel*: Level-spacing error, for the same trap strength, considering $\beta = 0, 1$ (solid curve), $\beta = 1, 2$ (dashed curve), $\beta = 2, 3$ (dashed-dotted curve) and $\beta = 3, 4$ (dotted curve).

frequency ω_0 and a spatial profile $f_{m,n}$. Following the treatment of Ref. [178], we replace the bosonic creation and annihilation operators with their expectation values, as can be justified for a noninteracting system. The steady state evolution of the photon-field amplitude in a cavity then follows that of the pump as $a_{m,n}(t) = a_{m,n}e^{-i\omega_0 t}$. Combining Hamiltonian evolution with pumping and losses, one arrives at a set of linear coupled equations that can be solved numerically for the steady-state[208]:

$$\begin{aligned} f_{m,n} = J\Big[& e^{-i\phi^x_{m,n}} a_{m+1,n} + e^{i\phi^x_{m-1,n}} a_{m-1,n} \\ & + e^{-i\phi^y_{m,n}} a_{m,n+1} + e^{i\phi^y_{m,n-1}} a_{m,n-1} \Big] \\ & + \left[\omega_0 + i\gamma - \frac{1}{2}\kappa \left((m-m_0)^2 + (n-n_0)^2 \right) \right] a_{m,n} \end{aligned} \quad (5.15)$$

where we have reintroduced the position of the harmonic trap centre (m_0, n_0), although unless otherwise specified we set $(m_0, n_0) = (0, 0)$ in our simulations.

The expectation values $|a_{m,n}|^2$ correspond to the number of photons at site (m, n), whereas the intensity spectrum is given by their total sum $\sum_{m,n} |a_{m,n}|^2$ as a function of pump frequency ω_0. These observables can be directly related to the eigenstates of the Hamiltonian in Eq. (5.1). Firstly, the different eigenmodes

of a driven-dissipative system will appear as peaks in the transmission and/or absorption spectra under a coherent pump [196]. The resonance peaks will be broadened by the decay rate γ, while the area of the peaks will depend on the overlap between the spatial amplitude profile of the pump and the underlying eigenstate of $\mathcal{H}$ at that energy.

Secondly, when the pump frequency is set on resonance with a given mode, the intensity profiles in both real- and momentum-space reproduce the wave function of that mode [196]. This corresponds respectively to measuring the near-field and far-field spatial emission of photons from the cavity array. We note that the far-field emission is simply the Fourier-transform of the real-space wave function and so will be a function of crystal momentum defined in the full BZ. To reach the MBZ, a further processing step is required; for example, if the Harper-Hofstadter Hamiltonian is in the Landau gauge and if we choose a magnetic unit cell of q plaquettes along $\hat{x}$, the appropriate transformation takes a particularly simple form [182]:

$$\sum_n |\psi_n(\mathbf{p}_{\mathrm{MBZ}})|^2 = \sum_j |\psi(\mathbf{p}_{\mathrm{BZ}} = \mathbf{p}_{\mathrm{MBZ}} - j\mathbf{G})|^2, \tag{5.16}$$

where $\psi_n(\mathbf{p}_{\mathrm{MBZ}})$ is the wave function coefficient in the MBZ, while $\psi(\mathbf{p}_{\mathrm{BZ}})$ is that in the original BZ. In this expression, j is an integer, while $\mathbf{G} = (2\pi/q)\hat{\mathbf{p}}_x$ is the magnetic reciprocal lattice vector, where the factor of q is due to the enlarged magnetic unit cell. We note that for other magnetic gauges or for other choices of the magnetic unit cell, this transformation will in general be more complicated. In this sense, we call this choice of magnetic unit cell, a "natural" choice when the Harper-Hofstadter Hamiltonian is in the Landau gauge. In the rest of the Chapter, we denote the momentum in the original BZ as $\mathbf{p}$, and that in the MBZ as $\mathbf{p}^0$.

5.2 Results and discussion

5.2.1 Pumping and gauge-dependent effects

As introduced above, spectroscopic measurements can be used in a driven-dissipative photonics experiment to study the trapped Harper-Hofstadter model and hence toroidal Landau levels in momentum space. In this section, we focus on the effects of the pumping, exploring how different pumping schemes excite the eigenstates with different weights. We find that such spectroscopic measurements are sensitive to the underlying synthetic magnetic gauge chosen in a given implementation of the Harper-Hofstadter Hamiltonian.

To best illustrate these gauge-dependent effects, we present the results of numerically solving Eq. (5.15) for the steady-state in a large lattice of $N \times N = 45 \times 45$ sites, with $\kappa = 0.02J$, $\gamma = 0.001J$ and $\alpha = 1/11$. These parameters are chosen to highlight the key features of different pumping schemes; we will present numerical results for a more realistic experimental system in Section 5.2.2. The

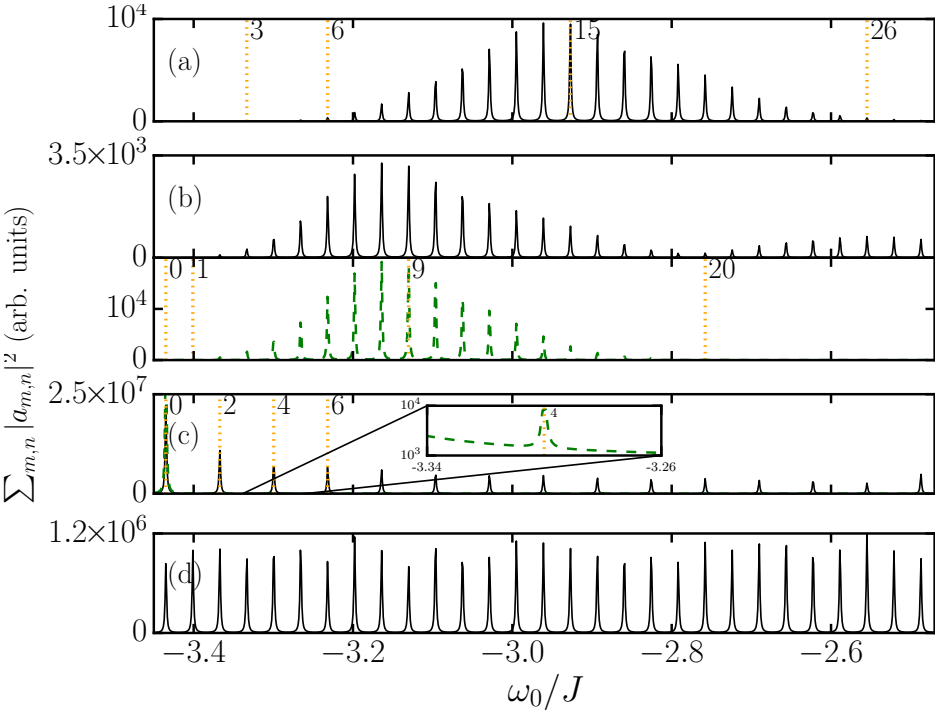

Figure 5.2: Intensity spectra for different pumping conditions: (a) pumping the single site (5,5), (b) pumping with a Gaussian profile centered at site (5,5) with width $\sigma = 1$, (c) homogeneous pumping across all lattice sites and (d) pumping with a random phase across all lattice sites. These results were obtained by numerical solving Eq. (5.15) for the steady-state in a lattice of $N \times N = 45 \times 45$ sites, with $\kappa = 0.02J$, $\gamma = 0.001J$ and $\alpha = 1/11$. Black (solid) curves correspond to using the Landau gauge while green (dashed) ones to the symmetric gauge. The dotted vertical lines (with labels indicating the value of β) mark the states which were selected for later analysis. The spectra in panels (a) and (d) are identical for both gauges.

numerical code was written in Julia [209] and is available online, as supplemental material to Ref. [210].

The intensity spectrum of the steady-state as a function of pump frequency is shown in Fig. 5.2, where we compare results for both the Landau and symmetric gauge for four pumping schemes, discussed in turn below. For simplicity we limit ourselves to pump frequencies located between the two lowest-lying Harper-Hofstadter bands of the untrapped system. This allows us to focus only on states within the first ladder of the trapped system (Eq. (5.7) with $n = 0$). At higher energies, the clear identification of states is more difficult as more than one ladder

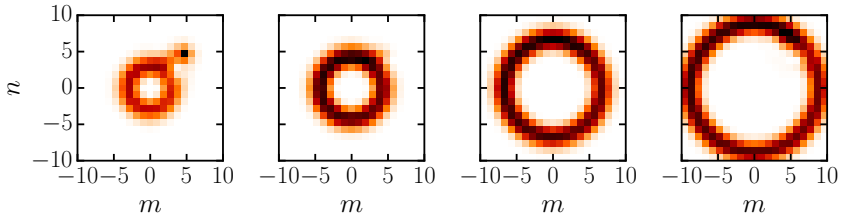

Figure 5.3: Real space reconstruction of the states $\beta = 3$, 6, 15 and 26 of Fig. 5.2(a).

of toroidal Landau levels can overlap, as shown, for example, in Section 5.2.2.

Single-site pumping–The first and simplest case that we consider is that of pumping a single site $f_{m,n} = \delta_{m,m_0}\delta_{n,n_0}$ at an off-center lattice site. These results are shown in Fig. 5.2 panel (a), where the uniform energy spacing of the toroidal Landau levels can be clearly observed. For this pumping scheme, we find no significant differences between the spectra for the Landau or symmetric gauge. This is to be expected as changing the gauge is equivalent to changing the relative phase between different sites, but as we are only pumping one site, this phase difference is unimportant.

Instead, for both magnetic gauges, we see that the peak height is very small for low energy states, rising to a maximum as energy increases, before decreasing once more. This behaviour can be understand by considering the form of the real space wavefunctions of $\mathcal{H}$. In real space, the eigenstates are rings of finite width which increase in radius as the energy increases (as can be seen in Fig. 5.3). Analytically, we can predict how the ring radius scales with energy by remembering that the term $(\beta+1/2)\kappa|\Omega_n|$ in Eq. (5.7) is the momentum-space kinetic energy $\frac{\kappa}{2}r^2$ where $r = i\nabla_{\mathbf{p}} + \mathcal{A}_{0,0}(\mathbf{p})$ is the physical position operator in the lowest band. From this, we deduce that $r^2 \approx \frac{1}{\pi}q\beta$, as can be confirmed numerically. Therefore, if one pumps an off-center site, there will only be a limited range of rings that will have radii that will overlap with the pump spot and so be excited. Here, we have set the pump spot to be at position $(5, 5)$, and from the above scaling, the toroidal Landau level that best overlaps with this pump will have a quantum number $\beta \approx 14$, which is in good agreement with the numerical results shown in Fig. 5.2 (a).

Gaussian pumping– We now consider a Gaussian pump as the next logical step up in complexity from a single-site pump. This has the form $f_{m,n} = \exp -\frac{1}{2\sigma^2}\left[(m-m')^2 + (n-n')^2\right]$, and we choose $\sigma = 1$ and for the pump centre to be at $(m', n') = (5, 5)$, as for single-site pumping. The results are shown in Fig. 5.2 (b). The main effect is, as expected, that more states become visible in both the low- (smaller β) and high-energy (larger β) sections of the spectrum. This is because the pump has a greater spatial width and so overlaps with a larger range of real-space eigenstates.

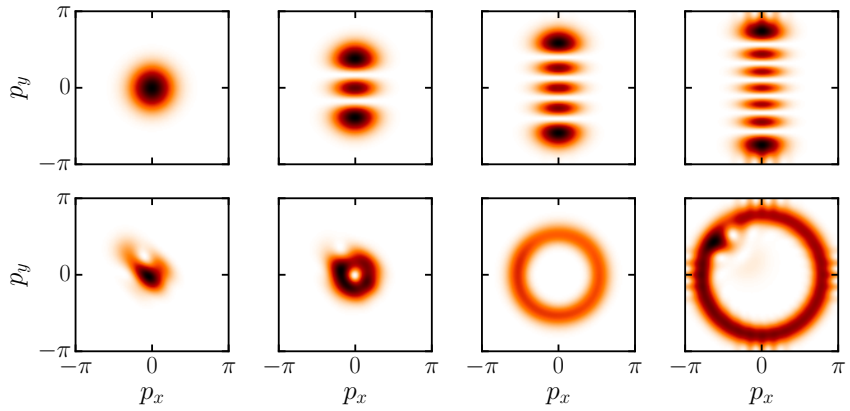

Figure 5.4: Momentum space reconstruction of the eigenstates. *Top row*: states corresponding to $\beta = 0$, 2, 4 and 6 in Fig. 5.2(c), using the Landau gauge. *Bottom row*: states corresponding to $\beta = 0$, 1, 9 and 20 in Fig. 5.2(b), using the symmetric gauge.

However, we can also see that the intensity spectrum now depends on the underlying magnetic gauge, as the phase of the eigenstates is important. In particular, more high-energy peaks can be seen for the Landau gauge than for the symmetric gauge. This can be most easily understood by noting that in momentum space, the symmetric-gauge states also have a ring-like structure (see bottom panel of Fig. 5.4), where the ring radius increases with β. To see this, we note that, in the symmetric gauge, the real-space wavefunctions have a phase which winds around the ring as $e^{i\beta\phi}$ where ϕ is the polar angle around the ring. This phase-winding sets the radius of the rings in momentum space as $p^2 \approx \pi\frac{\beta}{q}$; a scaling that can be confirmed numerically and seen in Fig. 5.4, bottom panel. (The white spot close to the edges of the rings in these figures is due to destructive interference with the pump.) As the Fourier transform of the Gaussian pump is again a Gaussian, it follows that only a limited range of low-energy symmetric-gauge momentum-space states will have a good overlap with the pump. The high energy portion of the spectrum is therefore washed out compared to its Landau gauge counterpart, where states have higher amplitude close to the centre of the BZ and so better overlap with the pump.

Before continuing, we also note that for sufficiently large values of β the symmetric-gauge rings in momentum space will increase to the point where they touch the BZ boundaries. When this occurs, self-interference patterns appear in the wave function as shown for example in Fig. 5.5. The extra ring-like structures appearing for $\beta \geq 30$ in Fig. 5.5 are due to the close proximity of states pertaining to other ladders with $n > 0$. Note that in order to excite such high-energy states, we have used a pump with a homogeneous amplitude and a random onsite phase,

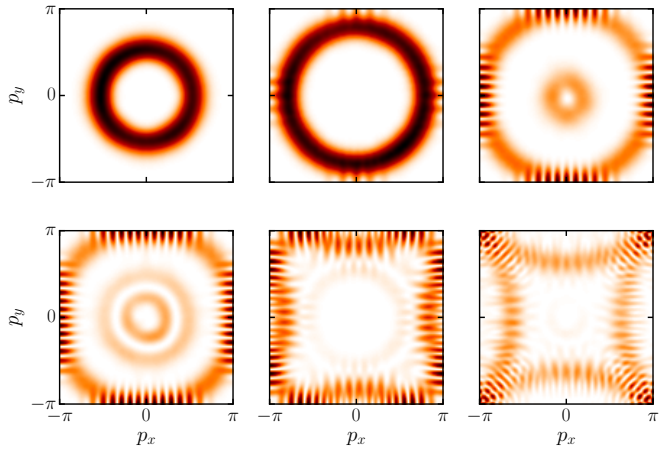

Figure 5.5: Momentum space reconstruction of the eigenstates in the full BZ, using the symmetric gauge and homogeneous pumping with a random on-site phase. *Top row*: states corresponding to $\beta = 9, 20, 30$. *Bottom row*: states corresponding to $\beta = 38, 59, 99$. Parameters are the same as in Fig. 5.2.

as will be presented in the fourth pumping case below.

Homogeneous pumping with uniform phase– If we now take the limit of a very wide Gaussian, we reach a homogeneous pump profile extended over all lattice sites. The results for this pumping scheme are shown in panel (c) of Fig. 5.2. Now $f_{m,n} = f$, and we see that the intensity spectrum is strongly magnetic-gauge dependent. In the Landau gauge, firstly, there are visible peaks for only half of the states. This can be understood by noting that a homogeneous pump in real space is a δ function in momentum space centered in the middle of the BZ. If we consider the Landau-gauge eigenstates in the full BZ, as shown in the top row of Fig. 5.4, we see that the states with an even value of β have an even number of nodes, with a lobe at the BZ center. Conversely, the states with odd values of β have an odd number of nodes, including one at the BZ center. (These feature can be related back to the properties of the Hermite polynomials in the analytical eigenstates in the MBZ Eq. (5.8).) Consequently, only states with even values of β have a good overlap with the pump, and the intensity spectrum contains half the expected peaks, now separated by twice the toroidal Landau level energy spacing.

In the symmetric gauge, secondly, we find only one out of every four states for homogeneous pumping, as can be seen in the inset of Fig. 5.2 (c). This is due to the fact that, on a square lattice, the angular momentum is conserved modulo 4, respecting the 4-fold rotational symmetry. The peak intensity gets smaller for larger β because of the diminishing overlap of the localized central pump with the increasing momentum-space ring discussed above.

Homogeneous pumping with a random on-site phase – As the fourth scheme, we consider a pump with a uniform amplitude over the lattice but a random site-dependent phase $\phi_{m,n}$: $f_{m,n} = fe^{i\phi_{m,n}}$. The phases are chosen from a random uniform distribution, and have values in the interval $[0, 2\pi)$. The bottom panel of Fig. 5.2 was obtained by averaging over 100 distinct realizations of these random phases. This results in a relatively even intensity distribution, for both gauges, where we can associate a peak to each toroidal Landau level in this energy window. While such a pumping scheme would therefore be the best way to excite all the eigenstates and to fully probe the momentum-space physics, we note that this would also be difficult to achieve in an experiment.

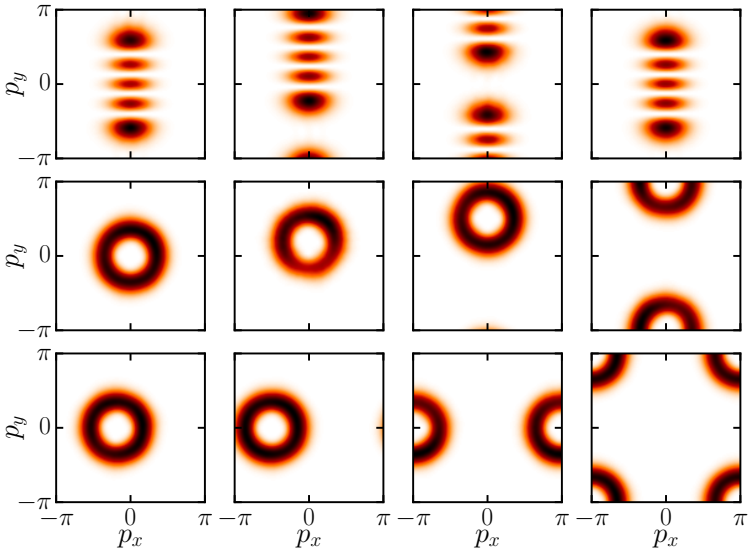

Figure 5.6: Momentum space reconstruction of the eigenstates in the full BZ, using the Landau (top row) and symmetric gauge (middle and bottom row) and a spatially homogeneous pump with a random on-site phase. We have considered the state $\beta = 4$ for different trap positions (m_0, n_0). For the top and middle rows, we have (from left to right): (0,0) (trap in the center), (2,0), (5.5,0) and (11,0), whereas for the bottom row we chose the positions (0,2), (0,5.5), (0,11) and (11,11). Parameters are the same as in Fig. 5.2.

Before continuing, we give a final example of an interesting gauge-dependent effect that could be studied experimentally in this system. Unlike the physics discussed above, this is not directly related to the pumping but instead to the behaviour of the wave function under a change in the centre of the harmonic trap (m_0, n_0). As derived in Ref. [189], moving the harmonic trap in space changes the boundary conditions on the wave function in the MBZ. We note that although

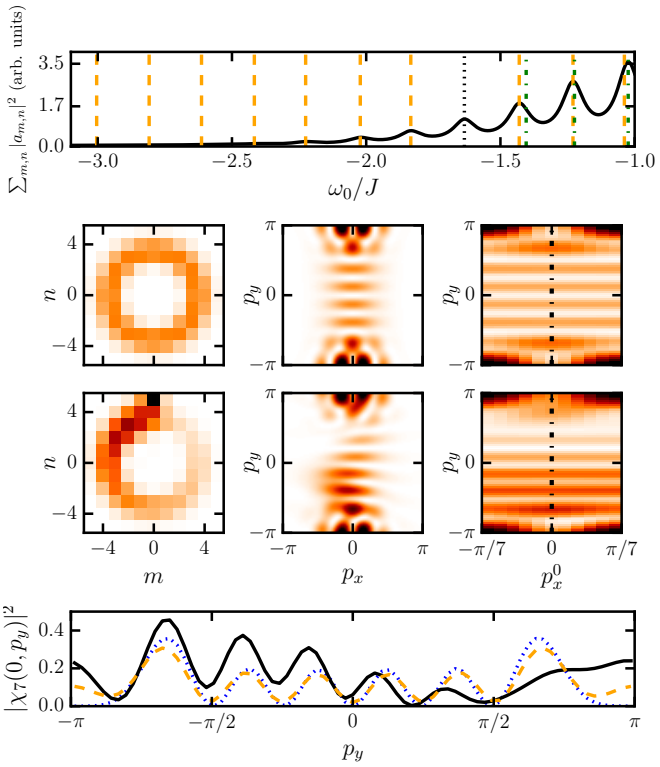

Figure 5.7: *Top row*: Intensity spectrum for a small lattice of 11×11 sites, with $\gamma = 0.05J$, $\kappa = 0.2J$ and $\alpha = 1/7$. *Second row*: Profile of the $\beta = 7$ state in real space (left), momentum space (center) and the population over bands in the MBZ (right) for the conservative system. *Third row*: Reconstruction of the $\beta = 7$ mode wavefunction in real space (left), momentum space (center) and the population over bands in the MBZ (right) obtained in the driven-dissipative system by pumping at $\omega_0 = -1.63J$, on resonance with the desired mode (black dotted line in the top panel). The δ-like pump at (0,5) is visible as a dark square in the left panel. *Bottom row*: Slice along the $p_x^0 = 0$ line in the MBZ (solid black line), compared to the analytical prediction of Eq. (5.8), $|\chi_7(0, p_y)|^2$ (blue dotted line) and to the population over bands for the nondissipative system (dashed orange line).

this derivation was made explicitly for the magnetic Landau gauge in the MBZ, numerically we observe here that this physics is also seen in the full BZ in both gauges. As shown in Fig. 5.6, a shift in the harmonic trap centre in one direction shifts the observed momentum-space pattern in the perpendicular direction. This behaviour can be understood as a realisation of Laughlin's *Gedankenexperiment*

for the quantum Hall effect but now in momentum space [189]. As we observe, the momentum-space wave function returns to itself after the harmonic trap has been moved q lattice sites for the magnetic Landau gauge but $2q$ lattice sites for the magnetic symmetric gauge, reflecting the underlying translational symmetry of $\mathcal{H}_0$ in the two different gauges.

5.2.2 Results for realistic experimental parameters

We now present numerical results for system parameters within current experimental reach, to demonstrate that the essential characteristics of toroidal Landau levels could be probed experimentally for the first time in photonics. We choose a small lattice of only 11×11 sites, with losses of $\gamma = 0.05J$; this loss rate is in the same range as those present in the experiment of Ref. [3]. Such a large loss rate broadens the peaks in the intensity spectrum, making closely-spaced eigenenergies harder to resolve. From Eq. (5.7), we see that the level spacing is given by $\frac{\kappa}{2\pi\alpha}$, and so we can increase the energy spacing by applying a stronger harmonic potential, chosen here as $\kappa = 0.2J$. Increasing the strength of the harmonic trap improves our flat-band approximation, but weakens the single-band approximation. To compensate for this, we consider a larger value of $\alpha = 1/7$, for which the larger band-gap $(E_1 - E_0)$ reduces band-mixing effects.

As in the experiment of Ref. [3], we work in the Landau gauge for the Harper-Hofstadter Hamiltonian, with hopping phases given by $\phi = (0, 2\pi\alpha m)$. In order to model the experimental pumping scheme where light was injected into a single resonator at the edge of the system via an external integrated waveguide [3], we consider a localized pump on a single site situated on the upper border of the system at $(m_0, n_0) = (0, 5)$. The corresponding intensity spectrum is shown in the 1st row of Fig. 5.7. Apart from the expected broadening due to larger losses, the peaks observed correspond well to the expected eigenenergies. As discussed above, single-site pumping limits the number of visible peaks, as the heights of the peaks at low-energies are suppressed due to the poor overlap of the real-space eigenstate with the pump position. However, as this pumping scheme is closest to that used in experiments, we emphasise that even in this case, enough peaks can be observed to extract quantitative measurements of the toroidal Landau level spacing. The orange vertical (dashed) lines show the first ladder of eigenstates of $\mathcal{H}$ from Eq. (5.1). We also note that here for frequencies larger than $-1.5J$, we also start to see states from the second ladder $\epsilon_{1,\beta}$ (see Eq. (5.7)), which are depicted as green vertical dash-dotted lines. Their proximity to the first ladder states means they cannot be easily resolved as separate peaks in the dissipative spectrum.

Setting the pump frequency at the energy indicated by the black dotted line, we plot the numerical near- and far-field emission in the left and center panels of the 3rd row of Fig. 5.7. This corresponds to the wave function in real space and in the full BZ, respectively. By applying the transformation in Eq. (5.16), we can also map the wave function in the full BZ to the population over bands in the

MBZ, as shown in the right panel of the 3rd row of Fig. 5.7. For comparison, we plot these quantities for the corresponding numerical eigenstate of $\mathcal{H}$ Eq. (5.1) in the second row of Fig. 5.7, for which there is no pumping and dissipation.

We find very good qualitative agreement between the numerical results in the MBZ and the analytical toroidal Landau level Eq. (5.8) with $\beta = 7$, as expected. We can make a quantitative comparison with this analytical eigenstate by taking a slice along the dash-dotted vertical lines ($p_x^0 = 0$) in the right column of rows 2 and 3; these cuts are shown in the bottom panel of Fig. 5.7 along with a dotted blue curve indicating the analytical eigenstate. As can be seen, there is excellent agreement between the numerics without driving and dissipation and the analytical result. We have checked that reducing κ makes this fit even better, pointing towards band-mixing effects. Introducing pumping and dissipation distorts the eigenstate, but many characteristic features are still clearly observable.

It is particularly interesting to note that in the driven-dissipative steady-state in real space, shown in the left panel of the 3rd row of Fig. 5.7, the photon distribution breaks the rotational symmetry of the ring eigenstate. While this can be physically understood as a decaying cyclotron orbit with an inverse lifetime set by γ, in terms of eigenmodes the exponential decay (and more generally the breaking of the rotational symmetry) results from the interference of several modes which overlap in frequency due to the relatively large value of γ. In the same way that real-space Landau levels give rise to real-space cyclotron orbits under the effect of the magnetic field, the observation of momentum-space Landau levels can provide clear evidence of a cyclotron orbit in momentum space under the effect of the Berry curvature, whose effect is indeed that of a momentum-space magnetic field.

Finally, we briefly summarize how one can practically measure the contribution δE_0 from the off-diagonal matrix elements of the Berry connection (see Eq. (5.10)) from the intensity spectrum. Starting from an experimental spectrum, one first needs to select a particular peak and determine its β label by comparing the MBZ reconstruction with the analytical result. The distance between two neighbouring peaks gives the level spacing $\kappa|\Omega_0|$. Finally, to separate the shift δE_0 from the Harper-Hofstadter ground state energy E_0 in Eq. (5.7), one can make use of the fact that the former depends on the trap strength κ, while the latter does not. Preparing two otherwise identical samples with different trap strengths and subtracting the ground state energy will then allow for a direct measurement of the contribution from the off-diagonal matrix elements of the Berry connection.

5.3 Conclusion

In conclusion, we have shown that the observation of toroidal Landau levels in momentum space is within experimental reach for state-of-the-art driven-dissipative photonic systems. Our proposal combines the recent realisation of the Harper-

Hofstatder model in an array of silicon-based coupled ring resonators in Ref. [3], with a harmonic potential, which could be introduced through a spatial modulation of the resonator size. We have presented numerical results to show that even for very small lattices, in the presence of driving and strong dissipation, key characteristics of the toroidal Landau levels can still be extracted. This would be a first direct investigation of analogue magnetic eigenstates in momentum space.

We have also emphasised that the proposed photonics experiment would be able to highlight a momentum-space analog of the cyclotron motion as well as to measure the energy shift due to the off-diagonal matrix elements of the Berry connection, which, as these are inter-band geometrical properties, are hard to access by other means. We have also discussed how the spectroscopic measurements presented here are sensitive to the specific synthetic magnetic gauge implemented in an experiment.

Finally, an interesting outlook would be to include the effect of photon-photon interactions in the model, as the degenerate ground states predicted in [189] for a weakly-interacting trapped Harper-Hofstadter model may lead to interesting nonlinear dynamical features. In the longer run, when the synthetic gauge field is combined with strong interactions, one can hope to observe the hallmarks of fractional quantum Hall physics [211, 212].

Conclusions

The main theme of this thesis was the study of well-established phenomena, namely superfluidity and magnetism, in a novel context of driven-dissipative photonic systems, which are subject to losses that need to be compensated by continuous pumping. After introducing the basic concepts in the setting of ultracold atomic gases in thermal equilibrium, we looked at how the effects of driving and dissipation changed this picture. In particular, we investigated the response of microcavity exciton-polaritons scattering against a stationary defect, with an eye on superfluid-like effects, and then turned to the momentum-space magnetism of resonator arrays.

In the case of polaritons, we looked at the single-fluid pump-only regime, as well as the three coupled fluids of the optical parametric oscillator regime created by the parametric scattering of the pump to the signal and idler states. We found that none of the two regimes displayed frictionless flow in the strict sense of the word. The pump-only fluid showed a density modulation localized close to the defect even in the "superfluid regime", resulting in a residual drag force that is entirely due to the finite polariton lifetime. On the other hand, we showed that the optical parametric oscillator regime, in the optical limiter configuration, always displays propagating density modulations in the pump, signal and idler, and therefore violates the definition of frictionless flow in a stronger, conceptual way. Futhermore, we determined two distinct types of threshold-like behaviour of the drag force as a function of fluid velocity in the pump-only case, one of which has no direct analog in equilibrium weakly-interacting atomic gases. In the optical parametric oscillator case, we singled out three factors which together determine the amplitude of the density modulations, and explained why, for typical experimental conditions, the signal state may appear superfluid.

In the last part of the manuscript, we have discussed how momentum-space Landau levels could be observed experimentally in driven-dissipative photonic systems, by breaking time-reversal invariance by means of a synthetic gauge field and creating topologically nontrivial energy bands. We have presented a realistic proposal for engineering these states by combining a harmonic trap with an artificial magnetic field for photons in a two-dimensional ring resonator array. An observation of momentum-space Landau levels would be the first realisation of magnetism on a toroidal surface. We have also demonstrated that the main

properties of momentum-space Landau levels may be observed spectroscopically for systems with realistic experimental parameters. Furthermore, spectroscopic measurements will be able to access the absolute energy of eigenstates, measuring novel geometrical features of energy bands, such as a contribution from the interband Berry connection. The pumping and losses present in these experiments also open the way towards studying analogue cyclotron orbits in momentum space.

In the future, more in-depth studies of polariton superfluidity, especially regarding the optical parametric oscillator regime, are needed. In experiments, one could look at multiply-connected geometries, and on the theoretical side, use nonequilibrium Keldysh field theory, which was already successfully employed in the case of incoherently pumped systems, in order to rigorously compute the superfluid and normal fractions. As far as the resonator arrays are concerned, it would be interesting to include photon-photon interaction in future studies, paving the way to fractional quantum Hall physics in a driven-dissipative setting.

Conclusiones

These closing conclusions are written in Spanish as required by the Spanish Government for thesis manuscripts in a foreign language.

El tema principal de esta tesis es el estudio de la superfluidez y magnetismo en un nuevo contexto de los sitemas fotónicos en presencia de bombeo y decadimiento. Estos sistemas están sujetos a pérdidas que necesitan ser compensadas con un bombeo continuo. Después de introducir los conceptos básicos para un sistema de gases atómicos ultrafríos en equilibrio térmico vemos cómo los efectos del bombeo y las pérdidas cambian el panorama. En particular, investigamos la respuesta de la difusión de los polaritones excitónicos en microcavidades bajo la presencia de un defecto estacionario, mirando los efectos de superfluidez. Posteriormente miramos el magnetismo en el espacio de momentos de matrices de resonadores.

En el caso de los polaritones consideramos el régimen de un solo fluido (estado de pump) y también el caso de tres fluidos acoplados en la configuración de oscilación óptica paramétrica creada por la difusión paramétrica del pump en los estados signal y idler. Encontramos que ninguno de los dos regímenes manifiestan un comportamiento de fluido sin fricción en el sentido estricto de la palabra. En el caso del fluido único existe una modulación de la densidad localizada cerca del defecto incluso en el régimen superfluido produciendo una fuerza de arrastre residual completamente debida al tiempo de vida finito de los polaritones. Por otra parte, vemos que el régimen de oscilación óptica paramétrica en la configuración del limitador óptico siempre muestra modulaciones de la densidad que se propaga en los estados de pump, signal y idler, y por tanto viola la definición de fluido sin fricción de una forma conceptual. Además determinamos dos tipos distintos de umbrales de la fuerza de arrastre como función de la velocidad del fluido y del pump, uno de ellos no tiene análogo directo con gases atómicos en equilibro débilmente interactuantes. En el caso del oscilador óptico paramétrico señalamos tres factores que juntos determinan la amplitud de la modulación de la densidad, que explican la aparente superfluidez del signal en condiciones experimentales típicas.

En la última parte de esta tesis discutimos como los niveles de Landau en el espacio de momentos pueden ser observados experimentalmente en sistemas fotónicos en presencia de bombeo externo y perditas, rompiendo la inversión tem-

poral por medio de un campo magnético artificial y creando bandas de energía topológicamente no triviales. Presentamos una propuesta realista para observar estos estados combinando una trampa armónica con un campo magnético artificial para fotones en una matriz de anillos resonantes bidimensional. Una observación de los niveles de Landau en el espacio de momentos sería la primera observación del magnetismo en una superficie toroidal. Además demostramos que las propiedades principales de los niveles de Landau en el espacio de momentos pueden ser observadas espectroscópicamente en sistemas con parámetros experimentales realistas. En el futuro, experimentos espectroscópicos podrán medir la energía absoluta de los autoestados describiendo nuevas propiedades geométricas de las bandas de energía, como ocurre en el caso de la conexión Berry entre bandas. El bombeo y las pérdidas que hay en estos experimentos abren una nueva vía para estudiar órbitas análogas a las del ciclotrón en el espacio de momentos.

En el futuro se requerirán estudios más a fondo de la superfluidez de los polaritones, sobre todo en el régimen de oscilación óptica paramétrica. En los experimentos uno puede mirar geometrías múltiplemente conexas. Desde el punto de vista de la teoría de Keldysh, basada en funciones de Green fuera del equilibro, que ha sido utilizada de manera satisfactoria en el caso de sistemas bombeados incoherentemente, para poder calcular de forma rigurosa las fracciones tanto superfluida como normal. En el caso de las matrices de resonadores podría ser interesante incluir la interacción fotón-fotón en futuros estudios, abriendo el camino en la física del efecto Hall cuántico fraccionario en sistemas con bombeo y dissipación.

References

[1] J. Toner and Y. Tu, Phys. Rev. Lett. **75**, 4326 (1995).

[2] I. Carusotto and C. Ciuti, Reviews of Modern Physics **85**, 299 (2013).

[3] M. Hafezi, S. Mittal, J. Fan, A. Migdall, and J. M. Taylor, Nature Photon. **7**, 1001 (2013).

[4] G. Bastard, *Wave mechanics applied to semiconductor heterostructures* (Wiley-Interscience, 1991).

[5] B. Deveaud and P. Schwendimann, *Electron and photon confinement in semiconductor nanostructures*, vol. 150 (IOS Press, 2003).

[6] A. Kavokin, J. J. Baumberg, G. Malpuech, and F. P. Laussy, *Microcavities* (Oxford University Press, 2007).

[7] J. Kasprzak, M. Richard, S. Kundermann, A. Baas, P. Jeambrun, J. M. J. Keeling, F. M. Marchetti, M. H. Szymańska, R. André, J. L. Staehli, V. Savona, P. B. Littlewood, B. Deveaud, and L. S. Dang, Nature **443**, 409 (2006).

[8] H. Deng, H. Haug, and Y. Yamamoto, Rev. Mod. Phys. **82**, 1489 (2010).

[9] J. Keeling, F. M. Marchetti, M. H. Szymańska, and P. B. Littlewood, Semiconductor Science and Technology **22**, R1 (2007).

[10] C. Ciuti, P. Schwendimann, B. Deveaud, and A. Quattropani, Phys. Rev. B **62**, R4825 (2000).

[11] C. Ciuti, P. Schwendimann, and A. Quattropani, Phys. Rev. B **63** (2001).

[12] C. Ciuti, P. Schwendimann, and A. Quattropani, Semiconductor Science and Technology **18**, S279 (2003).

[13] R. M. Stevenson, V. N. Astratov, M. S. Skolnick, D. M. Whittaker, M. Emam-Ismail, A. I. Tartakovskii, P. G. Savvidis, J. J. Baumberg, and J. S. Roberts, Phys. Rev. Lett. **85**, 3680 (2000).

[14] P. G. Savvidis, J. J. Baumberg, R. M. Stevenson, M. S. Skolnick, D. M. Whittaker, and J. S. Roberts, Phys. Rev. Lett. **84**, 1547 (2000).

[15] P. G. Savvidis, J. J. Baumberg, R. M. Stevenson, M. S. Skolnick, D. M. Whittaker, and J. S. Roberts, Phys. Rev. B **62**, R13278 (2000).

[16] J. J. Baumberg, P. G. Savvidis, R. M. Stevenson, A. I. Tartakovskii, M. S. Skolnick, D. M. Whittaker, and J. S. Roberts, Phys. Rev. B **62**, R16247 (2000).

[17] M. Saba, C. Ciuti, J. Bloch, V. Thierry-Mieg, R. André, L. S. Dang, S. Kundermann, A. Mura, G. Bongiovanni, J. L. Staehli, and B. Deveaud, Nature **414**, 731 (2001).

[18] K. Edamatsu, G. Oohata, R. Shimizu, and T. Itoh, Nature **431**, 167 (2004).

[19] S. Savasta, O. D. Stefano, V. Savona, and W. Langbein, Phys. Rev. Lett. **94** (2005).

[20] L. Lanco, S. Ducci, J.-P. Likforman, X. Marcadet, J. A. W. van Houwelingen, H. Zbinden, G. Leo, and V. Berger, Phys. Rev. Lett. **97** (2006).

[21] M. Abbarchi, V. Ardizzone, T. Lecomte, A. Lemaître, I. Sagnes, P. Senellart, J. Bloch, P. Roussignol, and J. Tignon, Phys. Rev. B **83** (2011).

[22] V. Ardizzone, M. Abbarchi, A. Lemaitre, I. Sagnes, P. Senellart, J. Bloch, C. Delalande, J. Tignon, and P. Roussignol, Phys. Rev. B **86** (2012).

[23] W. Xie, H. Dong, S. Zhang, L. Sun, W. Zhou, Y. Ling, J. Lu, X. Shen, and Z. Chen, Phys. Rev. Lett. **108** (2012).

[24] T. Lecomte, V. Ardizzone, M. Abbarchi, C. Diederichs, A. Miard, A. Lemaitre, I. Sagnes, P. Senellart, J. Bloch, C. Delalande, J. Tignon, and P. Roussignol, Phys. Rev. B **87** (2013).

[25] T. Karzig, C.-E. Bardyn, N. H. Lindner, and G. Refael, Phys. Rev. X **5**, 031001 (2015).

[26] A. Amo, J. Lefrère, S. Pigeon, C. Adrados, C. Ciuti, I. Carusotto, R. Houdré, E. Giacobino, and A. Bramati, Nat Phys **5**, 805 (2009).

[27] A. J. Leggett, Reviews of Modern Physics **71**, S318 (1999).

[28] M. Wouters and I. Carusotto, Phys. Rev. Lett. **105** (2010).

[29] M. Wouters and I. Carusotto, Phys. Rev. A **76** (2007).

[30] A. Amo, D. Sanvitto, F. P. Laussy, D. Ballarini, E. del Valle, M. D. Martin, A. Lemaître, J. Bloch, D. N. Krizhanovskii, M. S. Skolnick, C. Tejedor, and L. Viña, Nature **457**, 291 (2009).

[31] D. Sanvitto, F. M. Marchetti, M. H. Szymańska, G. Tosi, M. Baudisch, F. P. Laussy, D. N. Krizhanovskii, M. S. Skolnick, L. Marrucci, A. Lemaître, J. Bloch, C. Tejedor, and L. Viña, Nat Phys **6**, 527 (2010).

[32] C.-E. Bardyn, T. Karzig, G. Refael, and T. C. H. Liew, Phys. Rev. B **93**, 020502 (2016).

[33] C.-E. Bardyn, T. Karzig, G. Refael, and T. C. H. Liew, Phys. Rev. B **91**, 161413 (2015).

[34] A. V. Nalitov, D. D. Solnyshkov, and G. Malpuech, Phys. Rev. Lett. **114**, 116401 (2015).

[35] O. Bleu, D. D. Solnyshkov, and G. Malpuech, Phys. Rev. B **93**, 085438 (2016).

[36] T. Jacqmin, I. Carusotto, I. Sagnes, M. Abbarchi, D. D. Solnyshkov, G. Malpuech, E. Galopin, A. Lemaître, J. Bloch, and A. Amo, Phys. Rev. Lett. **112** (2014).

[37] M. Milićević, T. Ozawa, P. Andreakou, I. Carusotto, T. Jacqmin, E. Galopin, A. Lemaître, L. L. Gratiet, I. Sagnes, J. Bloch, and A. Amo, 2D Materials **2**, 034012 (2015).

[38] M. Hafezi, Int. J. Mod. Phys. B **28**, 1441002 (2014).

[39] J. Dalibard, F. Gerbier, G. Juzeliūnas, and P. Öhberg, Rev. Mod. Phys. **83**, 1523 (2011).

[40] N. Goldman, G. Juzeliūnas, P. Öhberg, and I. B. Spielman, Rep. Prog. Phys. **77**, 126401 (2014).

[41] N. Goldman, N. Cooper, and J. Dalibard, ArXiv e-prints (2015).

[42] Http://www.uam.es/personal_pdi/ciencias/fmarchet/students.html.

[43] S. Chu, Rev. Mod. Phys. **70**, 685 (1998).

[44] C. N. Cohen-Tannoudji, Rev. Mod. Phys. **70**, 707 (1998).

[45] G. Grynberg and C. Robilliard, Physics Reports **355**, 335 (2001).

[46] E. A. Cornell and C. E. Wieman, Rev. Mod. Phys. **74**, 875 (2002).

[47] W. Ketterle, Rev. Mod. Phys. **74**, 1131 (2002).

[48] I. Bloch, J. Dalibard, and W. Zwerger, Rev. Mod. Phys. **80**, 885 (2008).

[49] O. Morsch and M. Oberthaler, Rev. Mod. Phys. **78**, 179 (2006).

[50] L. P. Pitaevskii and S. Stringari, *Bose-Einstein Condensation* (Clarendon Press, 2004).

[51] P. C. Hohenberg, Phys. Rev. **158**, 383 (1967).

[52] M. H. Anderson, J. R. Ensher, M. R. Matthews, C. E. Wieman, and E. A. Cornell, Science **269**, 198 (1995).

[53] K. B. Davis, M. O. Mewes, M. R. Andrews, N. J. van Druten, D. S. Durfee, D. M. Kurn, and W. Ketterle, Phys. Rev. Lett. **75**, 3969 (1995).

[54] Y. Castin, in R. Kaiser, C. Westbrook, and F. David (editors), *Coherent atomic matter waves*, vol. 72 of *Les Houches - Ecole d'Ete de Physique Theorique*, 1–136 (Springer Berlin Heidelberg, 2001).

[55] A. Mostafazadeh, International Journal of Geometric Methods in Modern Physics **07**, 1191 (2010).

[56] I. Carusotto, S. X. Hu, L. A. Collins, and A. Smerzi, Phys. Rev. Lett. **97** (2006).

[57] I. Carusotto and G. Rousseaux, in D. Faccio, F. Belgiorno, S. Cacciatori, V. Gorini, S. Liberati, and U. Moschella (editors), *Analogue Gravity Phenomenology*, vol. 870 of *Lecture Notes in Physics*, 109–144 (Springer International Publishing, 2013).

[58] L. D. Landau and E. M. Lifshitz, *Statistical physics; 3rd ed.*, Course of theoretical physics (Butterworth, Oxford, 1980).

[59] G. E. Astrakharchik and L. P. Pitaevskii, Phys. Rev. A **70** (2004).

[60] S. Ianeselli, C. Menotti, and A. Smerzi, J. Phys. B: At. Mol. Opt. Phys. **39**, S135 (2006).

[61] L. D. Landau, E. M. Lifshitz, and L. P. Pitaevskii, *Electrodynamics of continuous media; 2nd ed.*, Course of theoretical physics (Butterworth, Oxford, 1984).

[62] J. V. Jelley, *Čerenkov radiation, and its applications* (Pergamon, 1958).

[63] L. D. Landau and E. M. Lifshitz, *Fluid mechanics; 2nd ed.*, Course of theoretical physics (Butterworth, Oxford, 1987).

[64] A. J. Leggett, *Quantum liquids: Bose condensation and Cooper pairing in condensed-matter systems* (OUP Oxford, 2006).

[65] L. Meyer and F. Reif, Phys. Rev. **123**, 727 (1961).

[66] D. R. Allum, P. V. E. McClintock, and A. Phillips, Philosophical Transactions of the Royal Society A: Mathematical, Physical and Engineering Sciences **284**, 179 (1977).

[67] N. R. Cooper and Z. Hadzibabic, Phys. Rev. Lett. **104** (2010).

[68] I. Carusotto and Y. Castin, Phys. Rev. A **84** (2011).

[69] S. T. John, Z. Hadzibabic, and N. R. Cooper, Phys. Rev. A **83** (2011).

[70] C. Raman, M. Köhl, R. Onofrio, D. S. Durfee, C. E. Kuklewicz, Z. Hadzibabic, and W. Ketterle, Phys. Rev. Lett. **83**, 2502 (1999).

[71] F. Chevy, K. W. Madison, and J. Dalibard, Phys. Rev. Lett. **85**, 2223 (2000).

[72] C. Ryu, M. Andersen, P. Cladé, V. Natarajan, K. Helmerson, and W. Phillips, Phys. Rev. Lett. **99** (2007).

[73] A. Ramanathan, K. C. Wright, S. R. Muniz, M. Zelan, W. T. Hill, C. J. Lobb, K. Helmerson, W. D. Phillips, and G. K. Campbell, Phys. Rev. Lett. **106** (2011).

[74] A. P. Chikkatur, A. Görlitz, D. M. Stamper-Kurn, S. Inouye, S. Gupta, and W. Ketterle, Phys. Rev. Lett. **85**, 483 (2000).

[75] R. Onofrio, C. Raman, J. M. Vogels, J. R. Abo-Shaeer, A. P. Chikkatur, and W. Ketterle, Phys. Rev. Lett. **85**, 2228 (2000).

[76] R. P. Feynman, R. B. Leighton, and M. Sands, *The Feynman lectures on physics, vol. 2: Mainly electromagnetism and matter* (Addison-Wesley, 1979).

[77] J. M. Ziman, *Principles of the Theory of Solids* (Cambridge university press, 1972).

[78] C. Cohen-Tannoudji, B. Diu, and F. Laloë, *Quantum mechanics, vol. 2* (Wiley, New York, NY, 1977).

[79] D. M. Stamper-Kurn, M. R. Andrews, A. P. Chikkatur, S. Inouye, H.-J. Miesner, J. Stenger, and W. Ketterle, Phys. Rev. Lett. **80**, 2027 (1998).

[80] B. P. Anderson and M. A. Kasevich, Science **282**, 1686 (1998).

[81] M. P. A. Fisher, P. B. Weichman, G. Grinstein, and D. S. Fisher, Phys. Rev. B **40**, 546 (1989).

[82] D. Jaksch, C. Bruder, J. I. Cirac, C. W. Gardiner, and P. Zoller, Phys. Rev. Lett. **81**, 3108 (1998).

[83] W. Zwerger, Journal of Optics B: Quantum and Semiclassical Optics **5**, S9 (2003).

[84] M. Greiner, O. Mandel, T. Esslinger, T. W. Hänsch, and I. Bloch, nature **415**, 39 (2002).

[85] L. D. Landau and E. M. Lifshitz, *Quantum mechanics: non-relativistic theory; 3rd ed.*, Course of theoretical physics (Butterworth, Oxford, 1977).

[86] D. Langbein, Phys. Rev. **180**, 633 (1969).

[87] D. Pfannkuche and R. R. Gerhardts, Phys. Rev. B **46**, 12606 (1992).

[88] P. G. Harper, Proc. Phys. Soc. A **68**, 874 (1955).

[89] D. R. Hofstadter, Phys. Rev. B **14**, 2239 (1976).

[90] C. R. Dean, L. Wang, P. Maher, C. Forsythe, F. Ghahari, Y. Gao, J. Katoch, M. Ishigami, P. Moon, M. Koshino, T. Taniguchi, K. Watanabe, K. L. Shepard, J. Hone, and P. Kim, Nature **497**, 598 (2013).

[91] G. L. Y. et. al., Nature Phys. **10**, 525 (2014).

[92] V. Schweikhard, I. Coddington, P. Engels, V. P. Mogendorff, and E. A. Cornell, Phys. Rev. Lett. **92**, 040404 (2004).

[93] R. A. Williams, S. Al-Assam, and C. J. Foot, Phys. Rev. Lett. **104**, 050404 (2010).

[94] M. Aidelsburger, M. Atala, M. Lohse, J. T. Barreiro, B. Paredes, and I. Bloch, Phys. Rev. Lett. **111**, 185301 (2013).

[95] H. Miyake, G. A. Siviloglou, C. J. Kennedy, W. C. Burton, and W. Ketterle, Phys. Rev. Lett. **111**, 185302 (2013).

[96] D. Jaksch and P. Zoller, New Journal of Physics **5**, 56 (2003).

[97] F. Gerbier and J. Dalibard, New Journal of Physics **12**, 033007 (2010).

[98] S. Powell, R. Barnett, R. Sensarma, and S. Das Sarma, Phys. Rev. A **83**, 013612 (2011).

[99] R. Peierls, Zeitschrift für Physik **80**, 763 (1933).

[100] R. Moessner, Canadian Journal of Physics **79**, 1283 (2001).

[101] J. K. Jain, *Composite fermions* (Cambridge University Press, 2007).

[102] J. Zak, Phys. Rev. **134**, A1602 (1964).

[103] J. Zak, Phys. Rev. **134**, A1607 (1964).

[104] B. A. Bernevig and T. L. Hughes, *Topological insulators and topological superconductors* (Princeton University Press, 2013).

[105] P. G. Harper, Proc. Phys. Soc. A **68**, 874 (1955).

[106] M. Kohmoto, Phys. Rev. B **39**, 11943 (1989).

[107] A. H. Castro Neto, F. Guinea, N. M. R. Peres, K. S. Novoselov, and A. K. Geim, Rev. Mod. Phys. **81**, 109 (2009).

[108] X.-G. Wen, Phys. Rev. B **65**, 165113 (2002).

[109] D. J. Thouless, M. Kohmoto, M. P. Nightingale, and M. den Nijs, Phys. Rev. Lett. **49**, 405 (1982).

[110] L. D. Landau and E. M. Lifshitz, *The classical theory of fields; 4th ed.*, Course of theoretical physics (Pergamon, Oxford, 1975).

[111] G. Wentzel and C. Houtermans, *Quantum theory of fields* (Courier Corporation, 2003).

[112] L. D. Landau and E. M. Lifshitz, *Mechanics; 3rd ed.*, Course of theoretical physics (Pergamon, Oxford, 1976).

[113] K. F. Riley, M. P. Hobson, and S. J. Bence, *Mathematical Methods for Physics and Engineering; 3rd ed.* (Cambridge University Press, New York, 2006).

[114] T. Winiecki, J. F. McCann, and C. S. Adams, Phys. Rev. Lett. **82**, 5186 (1999).

[115] R. W. Boyd, *Nonlinear Optics* (Academic Press, 2008).

[116] J. J. Hopfield, Phys. Rev. **112**, 1555 (1958).

[117] A. Baas, J.-P. Karr, M. Romanelli, A. Bramati, and E. Giacobino, Phys. Rev. Lett. **96** (2006).

[118] Y. Yamamoto and A. Imamoglu, Mesoscopic Quantum Optics, published by John Wiley & Sons, Inc., New York, 1999. **1** (1999).

[119] G. Rochat, C. Ciuti, V. Savona, C. Piermarocchi, A. Quattropani, and P. Schwendimann, Phys. Rev. B **61**, 13856 (2000).

[120] C. Weisbuch, M. Nishioka, A. Ishikawa, and Y. Arakawa, Phys. Rev. Lett. **69**, 3314 (1992).

[121] C. Ciuti, V. Savona, C. Piermarocchi, A. Quattropani, and P. Schwendimann, Phys. Rev. B **58**, 7926 (1998).

[122] F. Tassone and Y. Yamamoto, Phys. Rev. B **59**, 10830 (1999).

[123] M. M. Glazov, H. Ouerdane, L. Pilozzi, G. Malpuech, A. V. Kavokin, and A. D'Andrea, Phys. Rev. B **80** (2009).

[124] M. Combescot, O. Betbedermatibet, and F. Dubin, Physics Reports **463**, 215 (2008).

[125] C. Ciuti and I. Carusotto, Phys. Rev. A **74** (2006).

[126] E. Burstein and C. Weisbuch, *Confined electrons and photons: new physics and applications*, vol. 340 (Springer Science & Business Media, 2012).

[127] T. C. H. Liew and V. Savona, Phys. Rev. A **84** (2011).

[128] F. Marchetti and M. Szymańska, in V. Timofeev and D. Sanvitto (editors), *Exciton Polaritons in Microcavities*, vol. 172 of *Springer Series in Solid-State Sciences*, 173–213 (Springer Berlin Heidelberg, 2012).

[129] R. W. Boyd, *Nonlinear optics* (Academic press, 2003).

[130] D. M. Whittaker, Phys. Rev. B **71** (2005).

[131] S. Pigeon, I. Carusotto, and C. Ciuti, Phys. Rev. B **83** (2011).

[132] A. Amo, S. Pigeon, D. Sanvitto, V. G. Sala, R. Hivet, I. Carusotto, F. Pisanello, G. Lemenager, R. Houdre, E. Giacobino, C. Ciuti, and A. Bramati, Science **332**, 1167 (2011).

[133] G. Nardin, G. Grosso, Y. Léger, B. Piętka, F. Morier-Genoud, and B. Deveaud-Plédran, Nat Phys **7**, 635 (2011).

[134] D. Sanvitto, S. Pigeon, A. Amo, D. Ballarini, M. D. Giorgi, I. Carusotto, R. Hivet, F. Pisanello, V. G. Sala, P. S. S. Guimaraes, R. Houdré, E. Giacobino, C. Ciuti, A. Bramati, and G. Gigli, Nature Photonics **5**, 610 (2011).

[135] M. Wouters and I. Carusotto, Phys. Rev. B **75** (2007).

[136] Y. Yamamoto, *Fundamentals of Noise Processes* (Lecture Notes, 2004).

[137] G. K. Campbell, J. Mun, M. Boyd, E. W. Streed, W. Ketterle, and D. E. Pritchard, Phys. Rev. Lett. **96** (2006).

[138] W. B. Case, American Journal of Physics **64**, 215 (1996).

[139] R. M. Stevenson, V. N. Astratov, M. S. Skolnick, D. M. Whittaker, M. Emam-Ismail, A. I. Tartakovskii, P. G. Savvidis, J. J. Baumberg, and J. S. Roberts, Phys. Rev. Lett. **85**, 3680 (2000).

[140] J. J. Baumberg, P. G. Savvidis, R. M. Stevenson, A. I. Tartakovskii, M. S. Skolnick, D. M. Whittaker, and J. S. Roberts, Phys. Rev. B **62**, R16247 (2000).

[141] N. A. Gippius, S. G. Tikhodeev, V. D. Kulakovskii, D. N. Krizhanovskii, and A. I. Tartakovskii, Europhysics Letters (EPL) **67**, 997 (2004).

[142] D. M. Whittaker, Phys. Rev. B **63** (2001).

[143] G. Panzarini, L. C. Andreani, A. Armitage, D. Baxter, M. S. Skolnick, V. N. Astratov, J. S. Roberts, A. V. Kavokin, M. R. Vladimirova, and M. A. Kaliteevski, Phys. Rev. B **59**, 5082 (1999).

[144] K. V. Kavokin, I. A. Shelykh, A. V. Kavokin, G. Malpuech, and P. Bigenwald, Phys. Rev. Lett. **92** (2004).

[145] I. Carusotto and C. Ciuti, Phys. Rev. B **72** (2005).

[146] G. Dasbach, C. Diederichs, J. Tignon, C. Ciuti, P. Roussignol, C. Delalande, M. Bayer, and A. Forchel, Phys. Rev. B **71** (2005).

[147] A. Baas, J.-P. Karr, M. Romanelli, A. Bramati, and E. Giacobino, Phys. Rev. B **70** (2004).

[148] M. H. Szymańska, J. Keeling, and P. B. Littlewood, Phys. Rev. Lett. **96** (2006).

[149] G. Roumpos, M. Lohse, W. H. Nitsche, J. Keeling, M. H. Szymanska, P. B. Littlewood, A. Loffler, S. Hofling, L. Worschech, A. Forchel, and Y. Yamamoto, Proceedings of the National Academy of Sciences **109**, 6467 (2012).

[150] D. M. Whittaker, phys. stat. sol. (c) **2**, 733 (2005).

[151] F. M. Marchetti, M. H. Szymańska, C. Tejedor, and D. M. Whittaker, Phys. Rev. Lett. **105** (2010).

[152] G. Tosi, F. M. Marchetti, D. Sanvitto, C. Antón, M. H. Szymańska, A. Berceanu, C. Tejedor, L. Marrucci, A. Lemaître, J. Bloch, and L. Viña, Phys. Rev. Lett. **107** (2011).

[153] J. Keeling, Phys. Rev. Lett. **107** (2011).

[154] E. Cancellieri, F. M. Marchetti, M. H. Szymańska, and C. Tejedor, Phys. Rev. B **82** (2010).

[155] I. Carusotto and C. Ciuti, Phys. Rev. Lett. **93** (2004).

[156] C. Ciuti and I. Carusotto, physica status solidi (b) **242**, 2224 (2005).

[157] A. Amo, S. Pigeon, C. Adrados, R. Houdré, E. Giacobino, C. Ciuti, and A. Bramati, Phys. Rev. B **82** (2010).

[158] M. V. Regemortel and M. Wouters, Phys. Rev. B **89** (2014).

[159] N. Pavloff, Phys. Rev. A **66** (2002).

[160] P.-É. Larré, N. Pavloff, and A. M. Kamchatnov, Phys. Rev. B **86** (2012).

[161] A. C. Berceanu, E. Cancellieri, and F. M. Marchetti, Journal of Physics: Condensed Matter **24**, 235802 (2012).

[162] J. M. Zajac and W. Langbein, Phys. Rev. B **86** (2012).

[163] D. Ballarini, M. D. Giorgi, E. Cancellieri, R. Houdré, E. Giacobino, R. Cingolani, A. Bramati, G. Gigli, and D. Sanvitto, Nature Communications **4**, 1778 (2013).

[164] L. Dominici, D. Colas, S. Donati, J. P. R. Cuartas, M. D. Giorgi, D. Ballarini, G. Guirales, J. C. L. Carreño, A. Bramati, G. Gigli, E. del Valle, F. P. Laussy, and D. Sanvitto, Phys. Rev. Lett. **113** (2014).

[165] E. Altman, L. M. Sieberer, L. Chen, S. Diehl, and J. Toner, Phys. Rev. X **5** (2015).

[166] G. Dagvadorj, J. M. Fellows, S. Matyjaśkiewicz, F. M. Marchetti, I. Carusotto, and M. H. Szymańska, Phys. Rev. X **5**, 041028 (2015).

[167] M. V. Berry, Proceedings of the Royal Society A: Mathematical, Physical and Engineering Sciences **392**, 45 (1984).

[168] A. Shapere and F. Wilczek, *Geometric phases in physics*, vol. 14 (World Scientific Singapore, 1989).

[169] M. V. Berry, Proc. R. Soc. London, Ser. A **392**, 45 (1984).

[170] D. Xiao, M.-C. Chang, and Q. Niu, Rev. Mod. Phys. **82**, 1959 (2010).

[171] A. M. Dudarev, R. B. Diener, I. Carusotto, and Q. Niu, Phys. Rev. Lett. **92**, 153005 (2004).

[172] M.-C. Chang and Q. Niu, Phys. Rev. Lett. **75**, 1348 (1995).

[173] H. M. Price and N. R. Cooper, Phys. Rev. A **85**, 033620 (2012).

[174] M. Cominotti and I. Carusotto, Europhys. Lett. **103**, 10001 (2013).

[175] A. Dauphin and N. Goldman, Phys. Rev. Lett. **111**, 135302 (2013).

[176] M. Aidelsburger, M. Lohse, C. Schweizer, M. Atala, J. T. Barreiro, S. Nascimbene, N. Cooper, I. Bloch, and N. Goldman, Nature Phys. **11**, 162 (2015).

[177] G. Jotzu, M. Messer, R. Desbuquois, M. Lebrat, T. Uehlinger, D. Greif, and T. Esslinger, Nature **515**, 237 (2014).

[178] T. Ozawa and I. Carusotto, Phys. Rev. Lett. **112**, 133902 (2014).

[179] K. Bliokh and Y. Bliokh, Ann. Phys. **319**, 13 (2005).

[180] T. T. Wu and C. N. Yang, Phys. Rev. D **12**, 3845 (1975).

[181] N. R. Cooper and R. Moessner, Phys. Rev. Lett. **109**, 215302 (2012).

[182] H. M. Price, T. Ozawa, and I. Carusotto, Phys. Rev. Lett. **113**, 190403 (2014).

[183] E. N. Adams and E. I. Blount, J. Phys. Chem. Solids **10**, 286 (1959).

[184] N. Nagaosa, J. Sinova, S. Onoda, A. H. MacDonald, and N. P. Ong, Rev. Mod. Phys. **82**, 1539 (2010).

[185] S. Murakami, N. Nagaosa, and S.-C. Zhang, Science **301**, 1348 (2003).

[186] T. Fujita, M. B. A. Jalil, S. G. Tan, and S. Murakami, J. Appl. Phys. **110**, 121301 (2011).

[187] K. Y. Bliokh, Europhys. Lett. **72**, 7 (2005).

[188] P. Gosselin, F. Ménas, A. Bérard, and H. Mohrbach, Europhys. Lett. **76**, 651 (2006).

[189] T. Ozawa, H. M. Price, and I. Carusotto, Phys. Rev. A **92**, 023609 (2015).

[190] H. M. Price, T. Ozawa, N. R. Cooper, and I. Carusotto, Phys. Rev. A **91**, 033606 (2015).

[191] M. Claassen, C. H. Lee, R. Thomale, X.-L. Qi, and T. P. Devereaux, Phys. Rev. Lett. **114**, 236802 (2015).

[192] M. Mancini, G. Pagano, G. Cappellini, L. Livi, M. Rider, J. Catani, C. Sias, P. Zoller, M. Inguscio, M. Dalmonte, and L. Fallani, Science **349**, 1510 (2015).

[193] B. K. Stuhl, H.-I. Lu, L. M. Aycock, D. Genkina, and I. B. Spielman, Science **349**, 1514 (2015).

[194] R. Süsstrunk and S. D. Huber, Science **349**, 47 (2015).

[195] J. Ningyuan, C. Owens, A. Sommer, D. Schuster, and J. Simon, Phys. Rev. X **5**, 021031 (2015).

[196] I. Carusotto and C. Ciuti, Rev. Mod. Phys. **85**, 299 (2013).

[197] F. Grusdt, D. Abanin, and E. Demler, Phys. Rev. A **89**, 043621 (2014).

[198] T. Li, L. Duca, M. Reitter, F. Grusdt, E. Demler, M. Endres, M. Schleier-Smith, I. Bloch, and U. Schneider, ArXiv e-prints (2015).

[199] C. J. Kennedy, W. Cody Burton, W. C. Chung, and W. Ketterle, Nature Phys. **11**, 859 (2015).

[200] Y.-J. Lin, R. L. Compton, K. Jiménez-García, W. D. Phillips, J. V. Porto, and I. B. Spielman, Nature Phys. **7**, 531 (2011).

[201] L. J. LeBlanc, K. Jiménez-García, R. A. Williams, M. C. Beeler, W. D. Phillips, and I. B. Spielman, New J. Phys. **17**, 065016 (2015).

[202] T. Ozawa, Nature Phys. **11**, 801 (2015).

[203] Z. Fang *et al.*, Science **302**, 92 (2003).

[204] T. Scaffidi and S. H. Simon, Phys. Rev. B **90**, 115132 (2014).

[205] R. Dum and M. Olshanii, Phys. Rev. Lett. **76**, 1788 (1996).

[206] S. K. Dutta, B. K. Teo, and G. Raithel, Phys. Rev. Lett. **83**, 1934 (1999).

[207] A. Srivastava and A. Imamoglu, ArXiv e-prints (2015).

[208] C. Cohen-Tannoudji, J. Dupont-Roc, G. Grynberg, and P. Thickstun, *Atom-photon interactions: basic processes and applications* (Wiley, 1992).

[209] J. Bezanson, A. Edelman, S. Karpinski, and V. B. Shah, arXiv:1411.1607 [cs.MS] (2014).

[210] A. C. Berceanu, H. M. Price, T. Ozawa, and I. Carusotto, Phys. Rev. A **93** (2016).

[211] R. Umucalılar and I. Carusotto, Phys. Rev. Lett. **108**, 206809 (2012).

[212] M. Hafezi, M. D. Lukin, and J. M. Taylor, New J. Phys. **15**, 063001 (2013).